

# Neutron Star Observations: Prognosis for Equation of State Constraints

James M. Lattimer<sup>1</sup> and Madappa Prakash<sup>2</sup>

<sup>1</sup>*Department of Physics and Astronomy, SUNY at Stony Brook, Stony Brook, New York 11794-3800*

<sup>2</sup>*Department of Physics and Astronomy, Ohio University, Athens, OH 45701-2979*

We investigate how current and proposed observations of neutron stars can lead to an understanding of the state of their interiors and the key unknowns: the typical neutron star radius and the neutron star maximum mass. We consider observations made not only with photons, ranging from radio waves to X-rays, but also those involving neutrinos and gravity waves. We detail how precision determinations of structural properties would lead to significant restrictions on the poorly understood equation of state near and beyond the equilibrium density of nuclear matter.

To begin, a theoretical analysis of neutron star structure, including general relativistic limits to mass, compactness, and spin rates is made. A review is made of recent observations such as pulsar timing (which leads to mass, spin period, glitch and moment of inertia estimates), optical and X-ray observations of cooling neutron stars (which lead to estimates of core temperatures and ages and inferences about the internal composition), and X-ray observations of accreting and bursting sources (which shed light on both the crustal properties and internal composition). Next, we discuss neutrino emission from proto-neutron stars and how neutrino observations of a supernova, from both current and planned detectors, might impact our knowledge of the interiors, mass and radii of neutron stars. We also explore the question of how superstrong magnetic fields could affect the equation of state and neutron star structure. This is followed by a look at binary mergers involving neutron stars and how the detection of gravity waves could unambiguously distinguish normal neutron stars from self-bound strange quark matter stars.

PACS numbers: 26.60.+c, 21.10.-k, 97.60.Jd, 21.10.Gv, 21.65.+f

Keywords: Neutron Stars; Observations, Structure, Equation of State of Dense Matter

## Contents

<b>I. Introduction</b>	4
A. Personal note (James Lattimer)	6
B. Personal note (Madappa Prakash)	6
<b>II. Some maximal attributes of neutron stars</b>	7
A. The maximum mass	7
B. Maximum compactness	8
C. Maximum central density	9
D. Maximum spin rate	10
<b>III. Recent mass measurements and their implications</b>	12
<b>IV. The radius constraint</b>	14
<b>V. Neutron star crusts and their constraints</b>	17
A. Theoretical considerations	17
B. Observational application 1: Pulsar glitches	21
C. Observational application 2: Neutron star oscillations	22
D. Observational application 3: Thermal relaxation of the crust	23
<b>VI. Cooling neutron stars</b>	25
A. Observations of thermal emission	25
B. Implications for neutron star cooling	27
<b>VII. Other radius observables</b>	28
A. Pulse profiles	28
B. Redshift	28
C. Eddington limit	29
D. Quasi-periodic oscillations from accreting stars	31
E. Moments of inertia	31
<b>VIII. Neutrino emission from a proto-neutron star</b>	35
A. The birth of proto-neutron stars	35
B. Theoretical expectations	36
C. Model calculations	41
D. Metastable proto-neutron stars	43
<b>IX. Magnetic matters</b>	44
A. Magnetic effects on the EOS	45
B. Magnetic effects on neutron star structure	47
<b>X. Gravity wave emission from binary mergers</b>	50
A. Tidal disruption and mass transfer	51
B. Merger evolution	51
C. The EOSs of normal versus self-bound stars	53
D. Model evolutions	54
E. Observational parameters	56

<b>XI. Constraints from laboratory data</b>	57
A. Nuclear masses	57
B. Nuclear matter compression modulus	58
C. Symmetry energy and giant dipole resonances	58
D. Neutron skin thickness in nuclei	60
E. Heavy-Ion Collisions	60
1. Collective Flow	60
2. Multi-fragmentation	61
3. Isospin diffusion	62
<b>XII. Outlook</b>	63
<b>Acknowledgements</b>	65
<b>References</b>	65

## I. INTRODUCTION

Neutron stars are the most compact known objects without event horizons and therefore serve as extraordinary laboratories for dense matter physics. The internal composition of the cores of neutron stars is currently poorly understood. Most models of dense matter predict that above twice the equilibrium density of nuclear matter,  $\rho_s \simeq 2.7 \times 10^{14} \text{ g cm}^{-3}$  or  $n_s \simeq 0.16 \text{ baryons fm}^{-3}$ , exotica in the form of hyperons, a Bose condensate of pions or kaons, or deconfined quark matter, will eventually appear. However, whether the threshold density for such exotica is around twice  $\rho_s$ , or much larger, is unclear.

It has been suggested that if strange quark matter is the ultimate ground state of matter (i.e., has a lower energy at zero pressure than iron) [1], compression of matter to sufficiently high density would trigger a phase transition converting virtually the entire star into strange quark matter. Such a star is self-bound as opposed to being gravitationally bound as is the case of a normal neutron star.

It has so far proved very difficult to find venues from astrophysical observations that could unambiguously distinguish strange quark stars from normal neutron stars. This is because self-bound stars have similar radii, moments of inertia, and neutrino emissivities and opacities to that of moderate mass normal neutron stars. Therefore, it may be unlikely that photon or neutrino observations, or radio binary pulsar timing measurements, will be able to differentiate these cases, especially if strange quark stars have a small hadronic crust, supported perhaps by electrostatic forces or a mixed phase [2]. In that case, the effective temperatures and radii of solar-mass-sized strange quark stars and normal neutron stars would tend to be similar. Even during the proto-neutron star stage, which is observable through neutrino emissions [3], these two types of stellar configurations likely yield similar neutrino signals until such late times that the low luminosities prevent an unambiguous discrimination [4]. However, major differences in the evolutions of normal neutron stars and strange quark matter stars emerge during the final stages of binary mergers if stable mass transfer occurs. These differences would be prominent in both the amplitudes and frequencies of gravitational wave emissions. Except for discussing this latter topic, we will not discuss self-bound strange quark matter stars in detail further in this paper.

Possibly the two most important properties of neutron stars - their maximum masses and typical radii - are not yet well known. These properties reflect rather different aspects of the dense matter equation of state (EOS). The neutron star maximum mass, which is a consequence of general relativity and does not exist in Newtonian gravity, has a limit of, at most,  $3 M_\odot$ , assuming causality [5]. The maximum mass is controlled by the stiffness of the dense matter EOS at densities in excess of a few times  $n_s$ . The introduction of non-nucleonic degrees of freedom at supra-nuclear densities generally implies a softening of the EOS. The largest precisely known neutron star mass is only  $1.44 M_\odot$ , which is too small to provide an effective constraint on the composition of dense matter and the structural properties neutron stars. However, some recent mass measurements, detailed below, from timing of pulsars in binaries with white dwarf companions suggest that the maximum mass might be about  $2 M_\odot$  or even larger. In addition, large masses are also suggested from observations of QPO's, or quasi-periodic oscillations, observed in X-ray emission from neutron stars accreting from binary companions. If verified, a maximum mass in the vicinity of  $2 M_\odot$  would fundamentally alter our perception of the properties of matter in neutron star cores. As we demonstrate below, sufficiently large observed neutron star masses set interesting upper limits to the densities possible in neutron stars. It could be the case that the maximum density allowed is not large enough for exotic forms of matter to play significant roles.

On the other hand, the neutron star radius is controlled by properties of the nuclear force in the immediate vicinity of  $n_s$ , in particular by the density dependence of the nuclear symmetry energy [6] (the symmetry energy is the difference, at a given density, between the baryon energies of pure neutron matter and symmetric nucleonic matter). Measurements of the neutron star radius are far less precise than mass measurements. Among the observations recently utilized include radius upper limits from rapidly rotating

neutron stars, estimates from the thermal emission of cooling neutron stars, including redshifts, estimates obtained from the properties of sources with bursts or thermonuclear explosions on their surfaces, and estimates of crustal properties from (a) glitches of pulsars, (b) “star-quakes” occurring in the aftermath of giant flares from soft-gamma ray repeaters (SGR’s), and (c) cooling timescales during periods of quiescence in-between X-ray bursts from accreting neutron stars in low-mass X-ray binaries (LMXRB’s).

Aside from direct mass and radius determinations, one of our best windows into the interior is through observations of their thermal properties. Neutron star cooling curves (*i.e.*, their luminosities or temperatures as a function of age) are sensitive to the internal composition and the superfluid characteristics of its components. The interior of the star cools through the emission of neutrinos, which is very sensitive to composition and possible superfluidity. The crucial question is whether or not the neutrino emission processes are *rapid* or *slow*, terms having historical significance. The surface temperature of the neutron star, apart from an initial period of several to one hundred years, the thermal timescale of the crust, is intimately coupled to that of the core. After the crust reaches thermal equilibrium with the core, a rapidly cooling core would be revealed through relatively low surface temperatures for a given age. It is now realized that the behavior of the symmetry energy of dense matter is crucial in determining the relative rate of neutrino cooling. This is because the symmetry energy not only controls the rate of cooling for a mixture of nucleons, but also determines at what densities exotic material, such as hyperons, Bose condensates, or deconfined quark matter appear, all of which could allow relatively rapid cooling even if neutrino processes involving nucleons were slow.

There are other, less traditional, ways in which information about neutron stars can be gleaned. These involve neutrinos and gravity waves. Indeed, the fewer than two dozen neutrinos observed from SN 1987A are only the harbinger of the thousands expected in current detectors, or millions from planned detectors, from a galactic supernova. These neutrinos are emitted in two phases. The first is a tremendous burst accompanying core bounce, with peak luminosities of nearly 1000 bethes  $\text{s}^{-1}$  (1 bethe  $\equiv 10^{51}$  erg), exceeding the photon luminosity of all the stars in the visible universe during the same instant. The second is a continuous flux, quickly ramping down from the peak of the initial burst, from the deleptonizing proto-neutron star that will remain visible for perhaps fifty seconds. Nearly all ( $\sim 99\%$ ) of the neutron star’s binding energy of about 300 bethes is eventually radiated away in neutrinos of all flavors. The neutrino luminosities and the emission timescale are controlled by several factors including the total mass of the proto-neutron star and the opacity of neutrinos at supranuclear density, which depend on the star’s composition and the EOS of strongly interacting dense matter. The details of the neutrino light curve and neutrino energy distributions could reveal details of their internal compositions.

Last, but perhaps not least, prodigious amounts of gravity waves are expected to be emitted in the death throes of binary mergers involving neutron stars. Compact binaries, containing neutron stars and/or black holes, continuously radiate gravitational waves which cause their orbits to decay. Observed neutron star binaries have times-to-merger ranging from about 85 million years to tens of billions of years. Current estimates imply that there are about 1 merger per 10,000 years in our galaxy, and detectors such as the advanced LIGO might observe 40–400 events per year [7]. The observed patterns of gravitational waves could yield information about the masses of the components as well as estimates of the radii of inspiralling neutron stars. Furthermore, as we discuss below, there should be a pronounced difference in the observed wave pattern between mergers involving normal and self-bound strange stars. In contrast to other observational differences between normal and strange stars, which could have multiple sources, the differences observed in gravitational radiation would be relatively unambiguous and therefore, possibly, unique.

Complementary to observational constraints on neutron star structure are laboratory measurements which can restrict the range of nuclear parameters such as the incompressibility, the symmetry energy and its density dependence, nucleonic effective masses and nuclear specific heats, the high-density pressure-

density relation, and hyperon-nucleon couplings. We briefly review laboratory work involving dense matter and its relation to neutron star structure and compositions (we provide references to more detailed summaries). This experimental information ranges from measurements of nuclear masses (including high- $N$  and low- $Z$  nuclei in Radioactive Isotope Accelerators), nuclear charge radii, neutron skin thicknesses, frequencies of giant monopole and dipole resonances, and collective flow, multifragmentation and isospin diffusion information from heavy ion collisions.

### A. Personal note (James Lattimer)

I would like to take this opportunity to add some personal recollections of interactions with Hans Bethe. I was introduced to Hans in the summer of 1978 when I was an Urbana postdoc visiting Gerry Brown in Copenhagen. Gerry and Hans were interested in my work with Geoff Ravenhall on finite temperature nuclear phase coexistence [8] and Hans had developed his “low entropy” thesis that was so valuable to understanding gravitational collapse supernovae. During this time, I was invited to become a co-author of the paper that we, at least, have since referred to as BBAL [9]. I was greatly honored, of course. But when I was given a draft of the paper and saw it began with the phrase “Massive stars live for eons and eons ...”, I had second thoughts. I conveyed my misgivings about the astronomy to Gerry, but he assured me that Hans was very happy to accept criticism. I agreed to collaborate and began rewriting, much to Gerry’s chagrin. After my return to Urbana, and Hans to Ithaca, Gerry would distribute my rewrites to Hans and Hans’ to me. This iteration did not seem to rapidly converge, the paper developed into a 46-page journal article with seven appendices, and did not get submitted until the following Spring. Gerry still blames me for the delay, probably because a competing letter (with not dissimilar conclusions) I wrote at Urbana with Don Lamb, Chris Pethick and Geoff Ravenhall [10] had appeared shortly beforehand.

Another memorable occasion occurred in 1981, a year or two after I came to Stony Brook (partly, at least, on the back of BBAL). I had frequently cooked breakfast and dinner for Hans during summer trips to Copenhagen over the previous few years; he especially loved meat and always liked the rare steaks I cooked for him in Denmark (at least, what passed for steaks in Denmark). Gerry decided I should host a dinner for Hans at which all the graduate students in our group would attend. I decided to cook a leg of lamb on the barbecue. Around this time, Hans had become interested in neutrino diffusion in supernovae, and was intrigued by comments from Don Lamb that the boundary in collapsing material between trapped and freely-streaming neutrinos was particularly important in supernovae. Hans referred to this theory as the joint of Lamb. So, of course, when I took my leg of lamb off the grill and put it on the table before Hans, I pronounced it “the joint of lamb”. Hans, who loved puns, had a great laugh over this.

### B. Personal note (Madappa Prakash)

I distinctly recall my first meeting with Hans Bethe. One morning during my early years as a postdoc at Stony Brook, Gerry Brown came into my office and said “Come and tell Hans what you’re doing now; we’re in the common room”, and left. Expecting to see Hans Hansson, a friendly particle physicist, I grabbed my coffee cup and went into the common room. Sitting there was Hans Bethe, eating raisins one by one. Gerry said, “Go on, write something on the board and entertain us.” I recall feeling very ill. I said, “Could I bring my notes?” Gerry said, “Ok, if you really need them.” I ran into my room, grabbed my notes and returned to the common room where the two of them were waiting. I started writing on the board feeling more and more ill, but fortunately I was interrupted. Hans Bethe said, “Why are you keeping so many terms in the expansion?” (The physics issue was the influence of effective masses on the pressure of supernova matter.) I somehow found the courage to say, “I also have an exact and short

expression.” Bethe seemed to like that and said “If you have to keep more than one term in the expansion, you’re expanding about the wrong point.” Later, Gerry told me that Hans liked what I was doing, which was very gratifying. The work I was reporting to Bethe was later written up (with Tom Ainsworth, Jean-Paul Blaizot and Herman Wolter as co-authors) for Gerry Brown’s 60th Birthday Conference Proceedings “Windsurfing the Fermi Sea” [11].

My most memorable meeting with Bethe took place in Seattle during the “Supernova Physics” program, organized by Gerry Brown during the early years of the U.S. Institute for Nuclear Theory and held in a building some distance away from the old Physics Department. I was in awe that Bethe had solved two coupled differential equations to three decimal point accuracy using his slide rule, while others were still cajoling their computers. One afternoon, Gerry asked me to bring Bethe to the brown-bag lunch in the Physics Department, where Stan Woosley was to speak. We started walking toward the Physics building. Bethe walked slowly, so we were getting late. To make matters worse, he stopped now and then to pop raisins into his mouth. We arrived at a street crossing light, which turned green as we approached it. I hurried Bethe as best as I could, but when we were half-way across the lights turned red again. To my utter horror, the perpendicular traffic was accelerating toward us! I stood in the middle of the road with my arms widespread to stop the racing cars. Fortunately, Bethe ambled across to safety, while I was busy stopping impatient drivers in the middle of the road! Imagine the thoughts in my head! (I would be forever known as the man who got Bethe killed!) When we arrived at the lunch meeting, I was really angry at Gerry, who just smiled and said “Why did you think I asked you to bring him here?”

I wish there were more people like Hans Bethe. He was very kind to me, always made me feel good, and I learned a whole lot from him. I am very fortunate to have known him.

## II. SOME MAXIMAL ATTRIBUTES OF NEUTRON STARS

### A. The maximum mass

General relativity introduces a profound change to Newtonian hydrostatic equilibrium: the existence of a maximum mass. In general relativity, hydrostatic equilibrium is expressed by

$$\frac{dp(r)}{dr} = -\frac{G}{c^2} \frac{[p(r) + \epsilon(r)][M(r) + 4\pi r^3 p(r)/c^2]}{r(r - 2GM(r)/c^2)}, \quad \frac{dM(r)}{dr} = 4\pi^2 \rho(r), \quad (1)$$

where  $\epsilon = \rho c^2$  is the total mass-energy density. Rhoades & Ruffini [5] derived an upper limit of  $3.2 M_\odot$  to neutron star masses under the assumptions that the EOS (1) is less stiff than that of non-interacting degenerate neutron matter up to a fiducial mass (energy) density  $(\rho_f)\epsilon_f$ , which they chose to be  $\rho_f = \epsilon_f/c^2 = 4.6 \times 10^{14} \text{ g cm}^{-3}$ , and (2) is limited by causality at higher densities. In other words, they assumed the EOS

$$p(\epsilon) = p_{neutron}(\epsilon), \quad \epsilon \leq \epsilon_f; \quad p(\epsilon) = \epsilon - \epsilon_f + p_f, \quad \epsilon \geq \epsilon_f, \quad (2)$$

where  $p_f$  is the density at  $\epsilon_f$ . Hartle & Sabbadini [12] later showed this limit almost perfectly scales with  $\epsilon_f$  such that

$$M_{max} = 4.2 \sqrt{\epsilon_f/\epsilon_s} M_\odot. \quad (3)$$

Scaling results for “minimum period” EOSs

Eq.	$R_{sph}^{max} c^2 / GM_{sph}^{max}$	$(M_{sph}^{max})^2 \rho_c$		$(M_{sph}^{max})^2 \rho_{cent,sph}^{max}$		$\rho_{cent,sph}^{max} / \rho_c$	$P_{min} / M_{sph}^{max}$
		$c = G = 1$	$M_{\odot}^2 \text{ g cm}^{-3}$	$c = G = 1$	$M_{\odot}^2 \text{ g cm}^{-3}$	—	$M_{\odot}^{-1} \text{ ms}$
(6)	2.825	0.007247	$4.476 \times 10^{15}$	0.02193	$13.55 \times 10^{15}$	3.026	0.200
(7)	2.87	0.00725	$4.478 \times 10^{15}$	0.0219	$13.54 \times 10^{15}$	3.026	0.203

TABLE I: The quantities  $R_{sph}^{max}$ ,  $M_{sph}^{max}$  and  $\rho_{cent,sph}^{max}$  refer to the radius, mass and central mass density of the maximum mass configuration.  $P_{min}$  is the Keplerian rotational limit of the maximum mass configuration. The first line of results corresponds to Eq. (6); the second line is for Eq. (7).

## B. Maximum compactness

Concerning the maximum compactness, Lindblom [13] determined that the maximum redshift, for  $\rho_f \geq 3 \times 10^{14} \text{ g cm}^{-3}$  and assuming causality, is

$$z = \frac{1}{\sqrt{1 - 2GM/Rc^2}} - 1 \leq 0.863, \quad (4)$$

which is equivalent to

$$R \geq 2.83GM/c^2. \quad (5)$$

This result is relatively insensitive to the value of  $\rho_f$  and is consistent with the empirical limit established by Glendenning [14].

Koranda et al. [15] have given a very elegant and rigorous causal limit that is independent of any other assumptions about the EOS. They emphasized the special nature of the “minimum period” EOS (so named for reasons made evident below)

$$p(\epsilon) = 0, \quad \epsilon \leq \epsilon_c; \quad p(\epsilon) = \epsilon - \epsilon_c, \quad \epsilon \geq \epsilon_c. \quad (6)$$

This EOS contains a single parameter,  $\epsilon_c$  or  $\rho_c$ , and as a result the general relativistic structure equations, Eq. (1), then contain only one free parameter and one dimensional parameter,  $\epsilon_c$ , which corresponds to the surface energy density. All properties of spherical (*i.e.* non-rotating) stars with this EOS must therefore scale as  $M \propto R$  and  $\epsilon \propto M^{-2}$ . These considerations must apply, in particular, to the maximum mass configuration, whose radius, mass and central density are  $R_{sph}^{max}$ ,  $M_{sph}^{max}$  and  $\epsilon_{cent,sph}^{max}$  (or  $\rho_{cent,sph}^{max}$ ), respectively. Furthermore, this being the maximally stiff EOS at high density, and the minimally stiff EOS at low density, it will support the largest mass with the smallest radius. For a given value of  $\epsilon_c$ , the maximum mass configuration obviously is the most compact configuration. Integration of the dimensionless structure equations then yields the scaling relations shown in the first line of Table I for the maximum mass configurations.

Of course, the EOS in Eq. (6) is unrealistic in that the density at the surface of the star is finite, with a value generally well above the nuclear equilibrium density. A less rigorous, but more realistic, causally limited EOS consists of using a reasonably understood model (here chosen to be the FPS EOS [16]) for  $p(\epsilon)$  up to a matching energy density  $\epsilon_m$  where the pressure is  $p_m$ :

$$p(\epsilon) = p_{FPS}(\epsilon), \quad \epsilon \leq \epsilon_m; \quad p(\epsilon) = p_{FPS}(\epsilon_m), \quad \epsilon_m \leq \epsilon \leq \epsilon_c; \quad p(\epsilon) = \epsilon - \epsilon_c + p_m, \quad \epsilon \geq \epsilon_c. \quad (7)$$

Between  $\epsilon_m$  and  $\epsilon_c$ , the pressure is fixed, and above  $\epsilon_c$ , the EOS is causal. Choosing a matching baryon number density  $n_m = 0.1 \text{ fm}^{-3}$ , one has for the FPS EOS  $\epsilon_m = 1.262 \times 10^{-4} \text{ km}^{-2}$  and  $p_m = 5.69 \times 10^{-7} \text{ km}^{-2}$  (units where  $c = G = 1$ ). The maximum mass configurations retain, to a high accuracy, the scalings

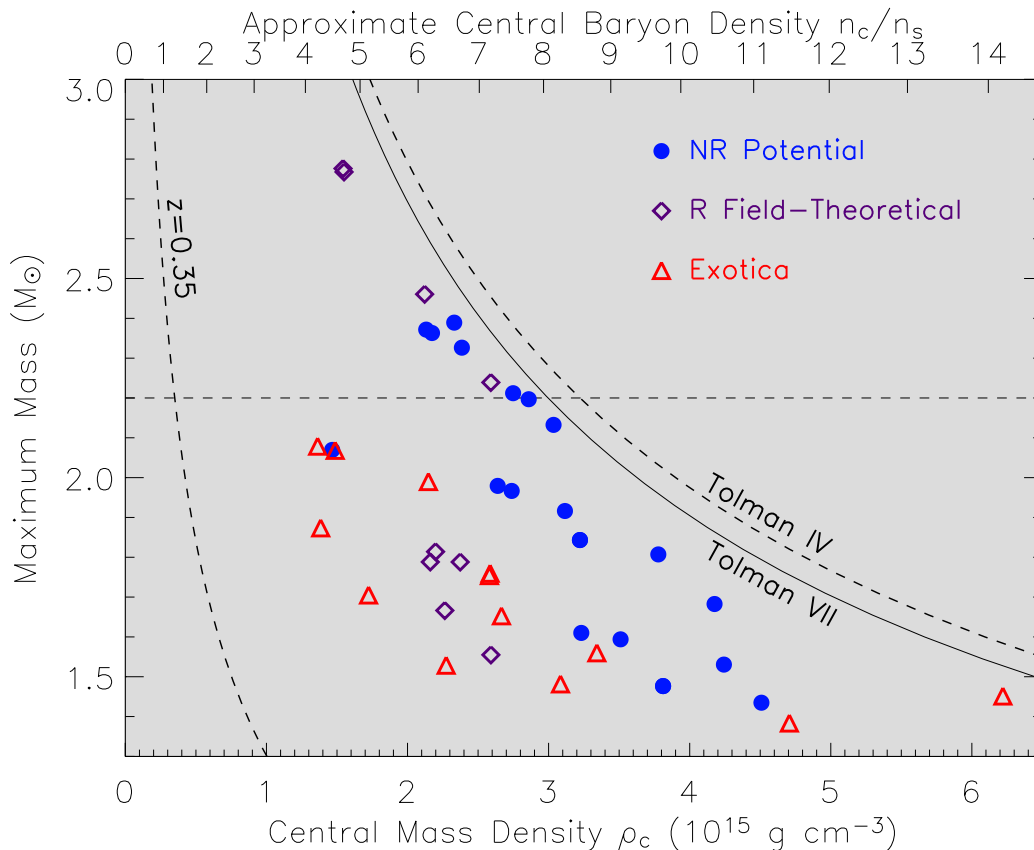


FIG. 1: The maximum mass - central density relation predicted by causality coupled with the Tolman VII and Tolman IV analytic GR solutions are compared with structure integration results for a variety of EOSs. NR refers to non-relativistic potential EOSs, R refers to relativistic field-theoretical EOSs, and Exotica refers to EOSs with considerable softening at high density due to kaon condensation or strange quark matter deconfinement. A possible redshift measurement of  $z = 0.35$  is also shown. Figure taken from. Ref. [17].

of the EOS Eq. (6), but the integration constants are slightly altered, as shown in the second line of Table I. These stars have slightly larger maximum masses and radii for a given value of  $\epsilon_c$ . Also note that the revised compactness limit is practically the same as established by Lindblom [13].

### C. Maximum central density

The “minimum period” EOS predicts the smallest radius possible for a given mass, with  $R \geq 2.87GM/c^2$ . Dimensionally,  $\rho \propto MR^{-3}$ , so a plausible conjecture would be that this EOS also predicts the largest possible value of the central density for a given mass. However, this is not the case. Lattimer & Prakash [17] investigated the maximum density question, with an eye toward using measured masses to set upper limits to the density of static matter in the universe. Their empirical results demonstrate that the predicted value of  $M^2\rho_{cent}$  for the “minimum period” EOS is close to, but less than, the actual limiting value. They found that an empirical limit can be found by combining the causality limit  $R \geq 2.87GM/c^2$  with the central density-mass relation implied by the Tolman VII analytic solution [18] of the general

relativistic structure equations. The Tolman VII solution has the explicit energy density-radius relation

$$\rho = \rho_{cent} \left[ 1 - \left( \frac{r}{R} \right)^2 \right], \quad (8)$$

which, combined with the causality limit, results in

$$\rho_{cent} M^2 = \frac{15}{8\pi} \left( \frac{M}{R} \right)^3 \leq \frac{15}{8\pi} \left( \frac{c^2}{2.87G} \right)^3 = 15.3 \times 10^{15} M_{\odot}^2 \text{ g cm}^{-3}. \quad (9)$$

This relation, and results for various EOSs, are displayed in Fig. 1. From Table I note that the “minimal period” EOS predicts a maximum central density with a coefficient of  $13.5 \times 10^{15}$  in Eq. (9), about 10% smaller than the empirical limit.

It should be emphasized that Eq. (9) represents the upper limit to the central density of the measured star. Since the maximum neutron star mass must be larger than that of any measured star, and the central density increases with mass for a given EOS, the central density of the actual maximum mass star must be smaller than the value given by Eq. (9) using the largest measured mass. With a mass measurement of  $2.1 M_{\odot}$ , for example, the limiting mass density is  $3.4 \times 10^{15} \text{ g cm}^{-3}$ . If the maximum mass was in fact about 10% larger, the limiting mass density becomes  $2.8 \times 10^{15} \text{ g cm}^{-3}$ . Note that this mass density corresponds to a baryon density of only about  $7n_s$ . This could be small enough to call into question the applicability of perturbative QCD in invoking the presence of a quark phase in neutron star cores. It must be stressed, however, that precocious perturbativeness may indeed occur in the quark matter sector.

#### D. Maximum spin rate

The compactness limits above are also intimately connected to the Keplerian, or mass-shedding, rotational limit obtained when the equatorial surface velocity equals the orbital speed just above the surface. The most compact star, assuming uniform rotation, has the highest rotational frequency. For a uniform rigid sphere of mass  $M$  and radius  $R$ , the mass-shedding limit in Newtonian gravity is

$$P_{min}^N = 2\pi \sqrt{\frac{R^3}{GM}} = 0.545 \left( \frac{M_{\odot}}{M} \right)^{1/2} \left( \frac{R}{10 \text{ km}} \right)^{3/2} \text{ ms}. \quad (10)$$

It is interesting and fortunate that the minimum spin period in fully relativistic calculations [19, 20] employing realistic hadronic EOSs is given to a good approximation by a similar formula

$$P_{min} \simeq 0.83 \left( \frac{M_{\odot}}{M_{sph}^{max}} \right)^{1/2} \left( \frac{R_{sph}^{max}}{10 \text{ km}} \right)^{3/2} \text{ ms}. \quad (11)$$

This spin period obtains for the maximum mass configuration, which has the smallest radius for hadronic EOSs. This formula takes into account not only general relativity, but also the deformation of rotating stars, yet is still expressed in terms of the non-rotating values of the maximum mass and radius. Therefore, the same scaling  $P_{min} \propto \sqrt{R^3/M}$  exists for both Newtonian and GR gravitation.

The same scaling exists for the “minimum period” EOS [15]: the scaling  $R_{sph}^{max} \propto M_{sph}^{max}$  for maximum mass stars implies that  $P_{min} \propto M_{sph}^{max}$ . Koranda et al. [15] determined the proportionality constant  $0.200 \text{ ms } M_{\odot}^{-1}$  for this case (see Table I). This translates into a coefficient of approximately 0.74 in Eq. (11). The ultra-compactness of stars constructed with the “minimum period” EOS accounts for the considerably smaller coefficient compared to that originally calculated for more realistic EOSs.

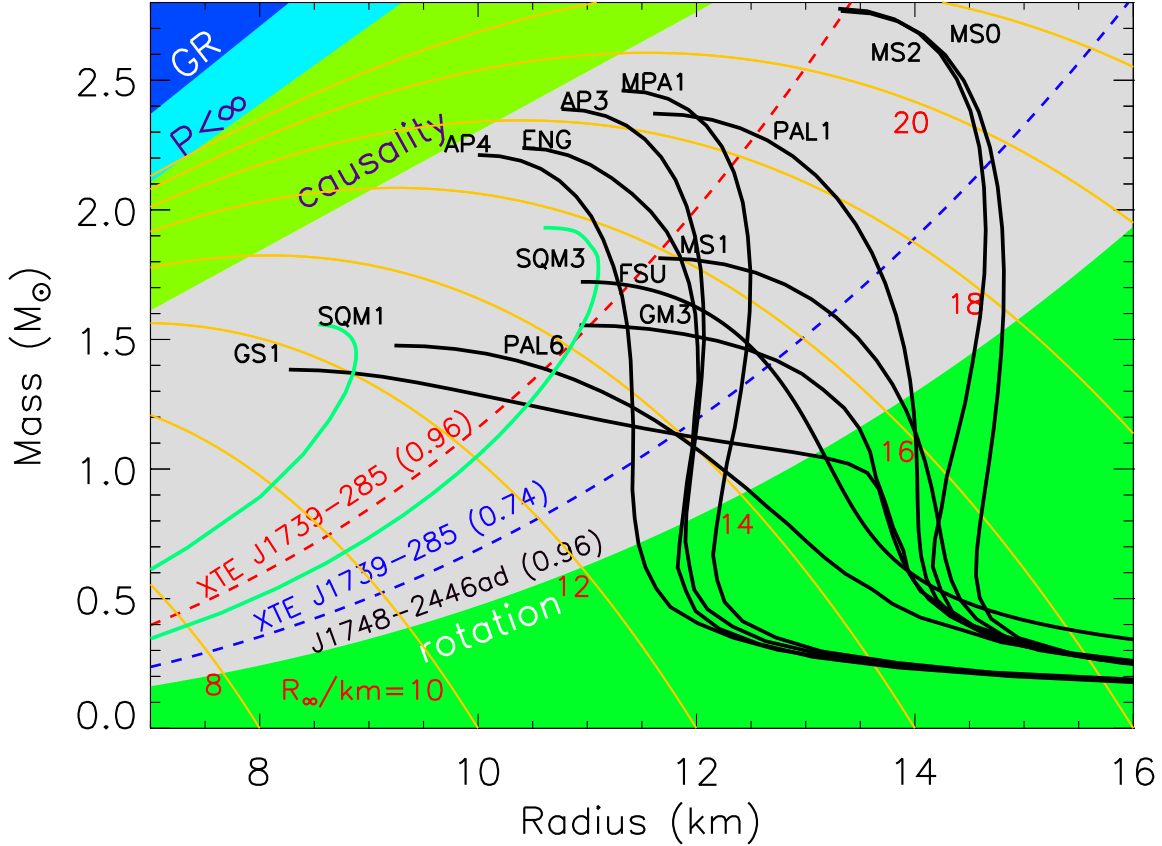


FIG. 2: Mass-radius trajectories for typical EOSs (see [6] for notation) are shown as black curves. Green curves (SQM1, SQM3) are self-bound quark stars. Orange lines are contours of radiation radius,  $R_\infty = R/\sqrt{1 - 2GM/Rc^2}$ . The dark blue region is excluded by the GR constraint  $R > 2GM/c^2$ , the light blue region is excluded by the finite pressure constraint  $R > (9/4)GM/c^2$ , and the green region is excluded by causality,  $R > 2.9GM/c^2$ . The light green region shows the region  $R > R_{max}$  excluded by the 716 Hz pulsar J1748-2446ad [22] using Eq. (12). The upper red dashed curve is the corresponding rotational limit for the 1122 Hz X-ray source XTE J1739-285 [23]; the lower blue dashed curve is the rigorous causal limit using the coefficient 0.74 ms in Eq. (12).

The relation in Eq. (11) applies only to the maximum mass configuration. Lattimer & Prakash [21] empirically found a somewhat more useful result which applies to an *arbitrary* neutron star mass, *so long as that mass is not close to the maximum mass*:

$$P_{min} \simeq (0.96 \pm 0.03) \left( \frac{M_\odot}{M_{sph}} \right)^{1/2} \left( \frac{R_{sph}}{10 \text{ km}} \right)^{3/2} \text{ ms}. \quad (12)$$

In this equation,  $M_{sph}$  and  $R_{sph}$  refer to the non-rotating mass and radius. Inasmuch as an observed neutron star is likely to be at least slightly smaller than the maximum mass, Eq. (12) can be used to limit masses and radii for observed stars:

$$R_{sph} < 10.4 \left( \frac{1000 \text{ Hz}}{\nu} \right)^{2/3} \left( \frac{M_{sph}}{M_\odot} \right)^{1/3} \text{ km}, \quad (13)$$

where the spin frequency  $\nu = 1/P$ .

The most rapidly rotating pulsar is PSR J1748-2446ad with a spin rate of 716 Hz [22]. With this value, Eq. (13) suggests that for a  $1.4 M_{\odot}$  star, the non-rotating radius would be limited by  $R < 14.3$  km as shown in Fig. 2. However, there is some likelihood that this star spun up through the accretion of a few tenths of a solar mass. If this star is, for example,  $1.7 M_{\odot}$ , the upper limit to the non-rotating radius would be 15.3 km. Unfortunately, neither limit is very restrictive at present.

Recently, however, an 1122 Hz X-ray burst oscillation from the neutron star X-ray transient XTE J1739-285 has been reported [23]. The stability of this oscillation frequency strongly suggests that it is the spin rate of the neutron star. If true, this sets relatively stringent limits to the radius that this star would have had if it was not rotating. According to the empirical relation Eq. (13), the maximum radii are 10.8 and 12.2 km, assuming the mass of this star to be 1.4 and  $2.0 M_{\odot}$ , respectively. Generally, these limits apply for stars not in the immediate vicinity of their maximum mass or for quark matter stars. As shown in Fig. 2 this constraint would rule out a number of EOSs. The rigorous causal limit, from Table I, yields 12.6 and 14.2 km, respectively. It will obviously be important to confirm this observation.

### III. RECENT MASS MEASUREMENTS AND THEIR IMPLICATIONS

Several recent observations of neutron stars have direct bearing on the determination of the maximum mass. The most accurately measured masses are from timing observations of the radio binary pulsars. As shown in Fig. 3, which is compilation of the measured neutron star masses as of November 2006, observations include pulsars orbiting another neutron star, a white dwarf or a main-sequence star. The compact nature of several binary pulsars permits detection of relativistic effects, such as Shapiro delay or orbit shrinkage due to gravitational radiation reaction, which constrains the inclination angle and allows the measurement of each mass in the binary. A sufficiently well-observed system can have masses determined to impressive accuracy. The textbook case is the binary pulsar PSR 1913+16, in which the masses are  $1.3867 \pm 0.0002$  and  $1.4414 \pm 0.0002 M_{\odot}$ , respectively [40].

One significant development concerns mass determinations in binaries with white dwarf companions, which show a broader range of neutron star masses than binary neutron star pulsars. Perhaps a rather narrow set of evolutionary circumstances conspire to form double neutron star binaries, leading to a restricted range of neutron star masses [53]. This restriction is likely relaxed for other neutron star binaries. Evidence is accumulating that a few of the white dwarf binaries may contain neutron stars larger than the canonical  $1.4 M_{\odot}$  value, including the intriguing case [45] of PSR J0751+1807 in which the estimated mass with  $1\sigma$  error bars is  $2.1 \pm 0.2 M_{\odot}$ . In addition, to 95% confidence, one of the two pulsars Ter 5 I and J has a reported mass larger than  $1.68 M_{\odot}$  [43].

Whereas the observed simple mean mass of neutron stars with white dwarf companions exceeds those with neutron star companions by  $0.25 M_{\odot}$ , the weighted means of the two groups are virtually the same. The  $2.1 M_{\odot}$  neutron star, PSR J0751+1807, is about  $4\sigma$  from the canonical value of  $1.4 M_{\odot}$ . *It is furthermore the case that the  $2\sigma$  errors of all but two systems extend into the range below  $1.45 M_{\odot}$ , so caution should be exercised before concluding that firm evidence of large neutron star masses exists.* Continued observations, which will reduce the observational errors, are necessary to clarify this situation.

Masses can also be estimated for another handful of binaries which contain an accreting neutron star emitting x-rays, as shown in Fig. 3. Some of these systems are characterized by relatively large masses, but the estimated errors are also large. The system of Vela X-1 is noteworthy because its lower mass limit ( $1.6$  to  $1.7 M_{\odot}$ ) is at least mildly constrained by geometry [26].

Raising the limit for the neutron star maximum mass could eliminate entire families of EOSs, especially those in which substantial softening begins around  $2$  to  $3n_s$ . This could be extremely significant, since exotica (hyperons, Bose condensates, or quarks) generally reduce the maximum mass appreciably.

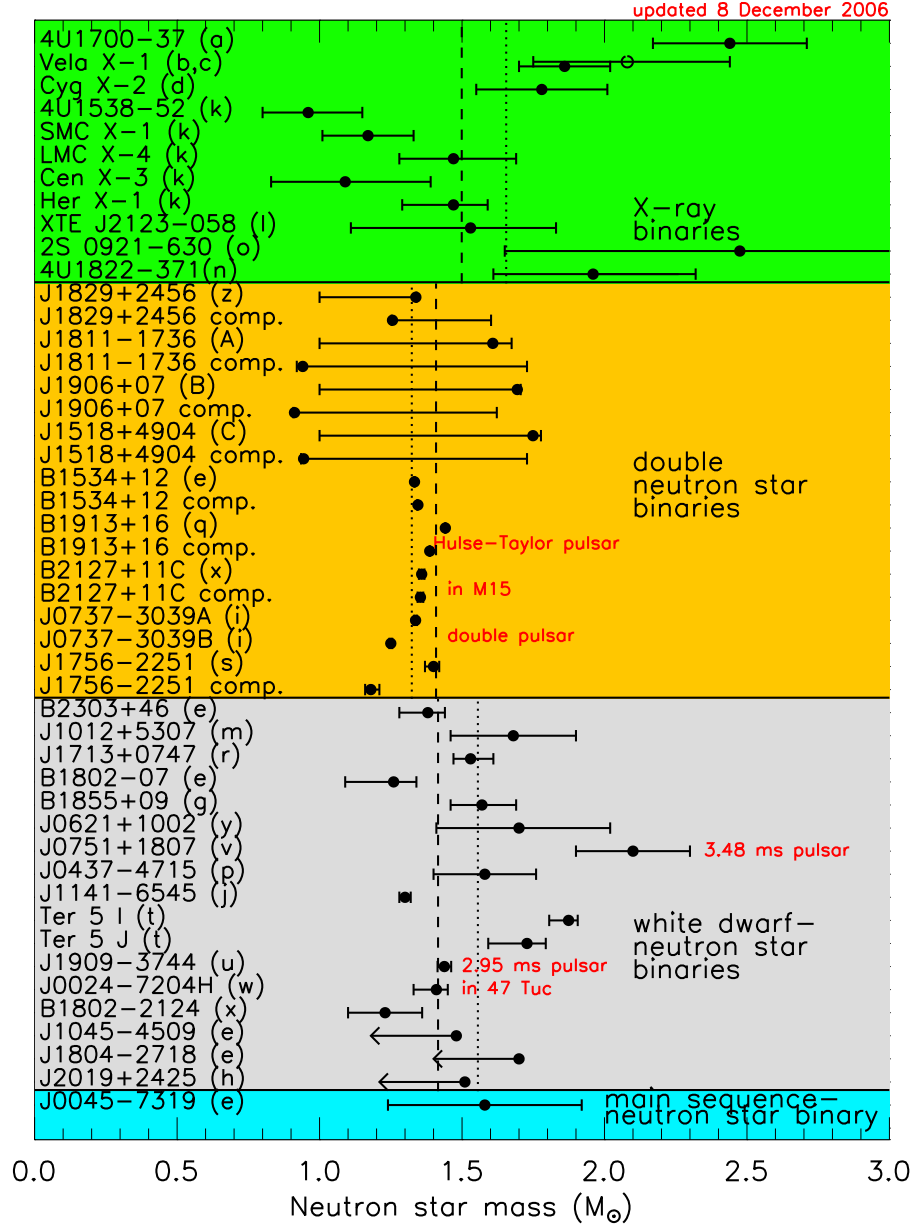


FIG. 3: Measured and estimated masses of neutron stars in radio binary pulsars (gold, silver and blue regions) and in x-ray accreting binaries (green). For each region, simple averages are shown as dotted lines; weighted averages are shown as dashed lines. The labels (a) = [24] through (C) = [52] are references cited in the bibliography. For the stars with references z-C, a lower limit to the pulsar mass of  $1 M_{\odot}$  was assumed.

Assuming that the hyperon-nucleon couplings are comparable to the nucleon-nucleon couplings typically results in the appearance of  $\Lambda$  and  $\Sigma^-$  hyperons around 2 to  $3 n_s$  in neutron star matter [54, 55, 56, 57]. In beta equilibrated neutron star matter, the various chemical potentials satisfy the relations  $\mu_n - \mu_p = \mu_e = \mu_{\Sigma^-}$  and  $\mu_n = \mu_{\Lambda}$ . As a consequence, the proton fraction in such matter is quite small, of order 5-10%. Little is known about the symmetry dependence of the hyperon-nucleon couplings as these couplings are chiefly determined from hyperon binding energies in more or less symmetric nuclei. If

hyperons indeed appear at as low a density as 2-3  $n_s$ , the maximum neutron star mass becomes relatively small, typically less than 1.6  $M_\odot$  [56].

The suggestion of Kaplan and Nelson [58] that, above some critical density, the preferred state of matter might contain a Bose-Einstein condensate of negatively charged kaons has been examined extensively [62, 63, 64, 65, 66, 67, 68]. The astrophysical consequences have been explored in some detail in Ref. [68]. The physics is that in medium, the strong attraction between  $K^-$  mesons and baryons increases with density and lowers the energy of the zero-momentum state. A condensate forms when this energy becomes equal to the kaon chemical potential,  $\mu$  which is related to the electron and nucleon chemical potentials by  $\mu = \mu_n - \mu_p = \mu_e = \mu_\mu$  due to chemical equilibrium in the various reactions. Typically, the critical density for condensation (which depends primarily on the symmetry energy of nucleonic matter) is  $\sim (3-4)n_s$ , although it is model and parameter dependent. Relative to matter without a kaon-condensed state and depending upon the models employed, maximum masses only as high as 1.5 to 1.6  $M_\odot$  can be obtained with kaon condensation.

If a different form of strangeness can appear prior to hyperons or Bose condensates, for example, deconfined  $u$ ,  $d$ , and  $s$  quark matter, maximum masses up to approximately 2.0  $M_\odot$  are possible [69], but only with special fine-tuning of the nucleonic and quark matter parameters. Therefore a confirmation of a neutron star mass in excess of 2  $M_\odot$  would be especially interesting.

A parameter of increasing interest, as the database of neutron star masses expands, concerns the *minimum* mass of neutron stars. It is believed that neutron stars are created in the aftermath of gravitational collapse supernovae and must therefore pass through a proto-neutron star state in which a large number of neutrinos are trapped and a moderate entropy exists [3]. For such a configuration, the range of stable masses is much narrower than for cold, catalyzed systems. The minimum mass of a cold star is about 0.09  $M_\odot$ , only slightly sensitive to the EOS around  $\rho_s$ . A star with a trapped lepton fraction  $Y_L \sim 0.35 - 0.4$  and an entropy per baryon  $s \sim 1 - 2$  has a minimum mass of about 0.85  $M_\odot$  [70] for stability. The smallest reliably estimated neutron star mass is the companion of the binary pulsar J1756-2251 whose mass is  $1.18 \pm 0.02 M_\odot$  [42]. It will be interesting to see if smaller neutron stars are found.

#### IV. THE RADIUS CONSTRAINT

As previously mentioned, the radius of a neutron star is primarily determined by the density dependence of the symmetry energy. This connection arises through the relation between the neutron star radius and the internal pressure of matter at intermediate densities ( $1.5n_s < n < 2 - 3 n_s$ ). That such a relation exists can be seen most clearly by considering Newtonian polytropes. For the pressure-density relation

$$p = K\rho^{1+1/n}, \quad (14)$$

where  $K$  is a constant and  $n$  is the polytropic index, hydrostatic equilibrium implies that

$$R \propto K^{n/(3-n)} M^{(1-n)/(3-n)}. \quad (15)$$

Realistic EOSs typically have  $n \simeq 1$ , but  $K$  is uncertain by a factor of 5 or 6. For some average density  $\rho_*$ , in the vicinity of  $(1-2)m_b n_s$ , suppose the pressure is  $p_*$ . For the case  $n = 1$ , one therefore has

$$R \propto p_*^{1/2} \rho_*^{-1} M^0. \quad (16)$$

The independence of  $R$  from  $M$  is a characteristic result of the mass-radius trajectories for EOSs without extreme low-density softening, as seen in Fig. 2. Equation (16) suggests that the radius scales with the square root of the fiducial pressure  $p_*$ . However, general relativity plays an important role, and with its

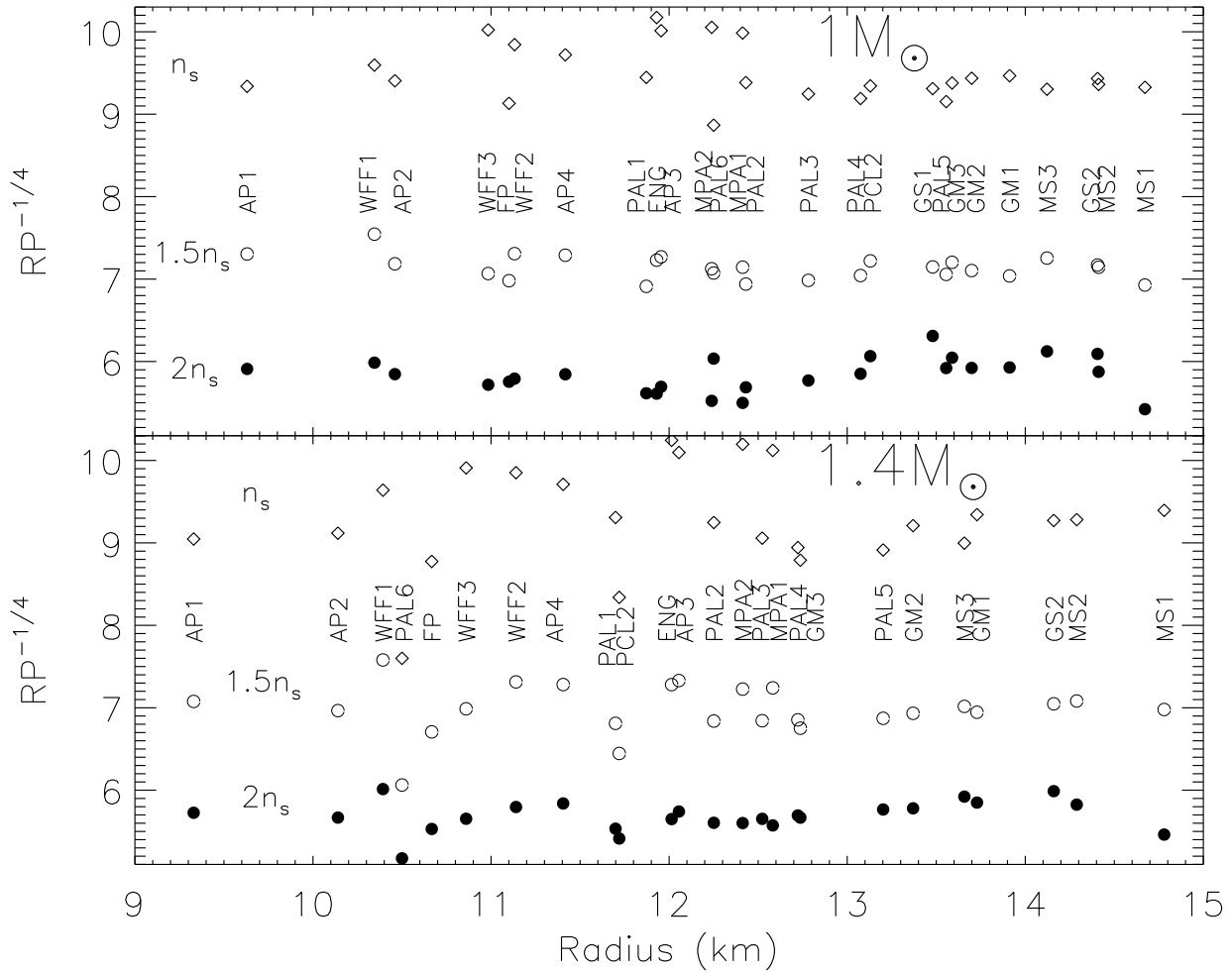


FIG. 4: Empirical demonstration of the constancy  $Rp_*^{-1/4}$ , for  $1 M_\odot$  (upper panel) and  $1.4 M_\odot$  (lower panel) stars. For each mass, 3 fiducial number densities are selected. Figure and EOS labels are from reference [6].

inclusion, the scaling is such that  $R \propto p_*^{1/4}$  [6]. This is an empirical result, and is graphically illustrated in Fig. 4. It is important to note that it applies to nearly all neutron star EOSs, not just those that have a portion of the  $M - R$  curve with vertical slope. The exceptions to the  $R \propto p_*^{1/4}$  rule are the EOSs for strange quark stars or EOSs with extreme softening near  $\rho_s$ . The correlation is more robust if the fiducial density is taken to be  $2n_s$  rather than  $n_s$ .

Using the only known analytic solution of Einstein's equations with vanishing surface energy density and an explicit pressure - density relation, this scaling can be analytically demonstrated. This solution, due to Buchdahl [71], assumes the EOS

$$\epsilon = 12\sqrt{p_*p} - 5p, \quad (17)$$

where  $p_*$  is a parameter. For low densities, when  $p \ll p_*$ , one sees that this EOS is that of an  $n = 1$  polytrope, so this solution is a reasonable approximation for a neutron star. For this solution, the radius is an implicit function of  $M$  and  $p_*$ :

$$R = (1 - \beta)\sqrt{\frac{\pi}{288p_*(1 - 2\beta)}}, \quad (18)$$

where  $\beta = GM/Rc^2$ . In turn, these relations lead to

$$\left. \frac{d \ln R}{d \ln p} \right|_{n,M} = \frac{1}{2} \frac{(1-\beta)(1-2\beta)}{(1-3\beta+3\beta^2)} \frac{6-5\sqrt{p/p_*}}{6+\sqrt{p/p_*}}. \quad (19)$$

Choosing for typical values  $M = 1.4 M_\odot$ ,  $R = 13$  km, and  $\epsilon = 1.5m_b n_s = 2.97 \times 10^{-4} \text{ km}^{-2}$ , one finds  $\beta = 0.318$  and, using Eq. (17),  $p/p_* = 0.141$ . Substitution in Eq. (19) yields  $d \ln R/d \ln p = 0.230$ , quite close to the empirical result of about 1/4.

This correlation is significant because the pressure of degenerate neutron-star matter near the nuclear saturation density  $n_s$  is, in large part, determined by the symmetry properties of the EOS. For the present discussion, we introduce the incompressibility  $K$  and the skewness  $K'$ , and expand the nucleonic energy per particle about its values at  $n_s$  and  $x = 1/2$ , where  $x$  is the proton fraction:

$$E(n, x) = -16 + \frac{K}{18} \left(1 - \frac{n}{n_s}\right)^2 + \frac{K'}{27} \left(1 - \frac{n}{n_s}\right)^3 + E_{sym}(n)(1-2x)^2 \dots \quad (20)$$

Here,  $E_{sym}$  is the symmetry energy function, approximately the energy difference at a given density between symmetric and pure neutron matter. The symmetry energy parameter is defined as  $S_v \equiv E_{sym}(n_s)$ . For the total energy, leptonic contributions (mainly from electrons as that from muons is small in the vicinity of the nuclear equilibrium density)

$$E_e = (3/4)\hbar c x(3\pi^2 n x^4)^{1/3} \quad (21)$$

must be added to  $E(n, x)$ . Because catalyzed matter in neutron stars is in beta equilibrium, i.e.,  $\mu_e = \mu_n - \mu_p = -\partial E/\partial x$ , the equilibrium proton fraction at  $n_s$  is

$$x_s \simeq (3\pi^2 n_s)^{-1} (4S_v/\hbar c)^3 \simeq 0.04. \quad (22)$$

This small value of  $x_s$  enables the pressure at  $n_s$  to be expressed as

$$P(n_s, x_s) = \left( n^2 \frac{\partial [E(n, x) + E_e(n, x)]}{\partial n} \right)_{n_s, x_s} = n_s(1-2x_s)[n_s S'_v(1-2x_s) + S_v x_s] \simeq n_s^2 S'_v, \quad (23)$$

where  $S'_v \equiv (\partial E_{sym}/\partial n)_{n_s}$ . The pressure depends primarily upon  $S'_v$ , because the terms proportional to  $x_s$  are relatively small. The equilibrium pressure at moderately larger densities is similarly insensitive to  $K$  and  $K'$ . Experimental constraints to the compression modulus  $K$ , most importantly from analyses of giant monopole resonances give  $K \simeq 220$  MeV [72]. The skewness parameter  $K'$  has been estimated to lie in the range (1780–2380) MeV [73]. Evaluating the pressure for  $n = 1.5n_s$ ,

$$P(1.5n_s) = 2.25n_s[K/18 - K'/216 + n_s(1-2x)^2(\partial E_{sym}/\partial n)_{1.5n_s}]. \quad (24)$$

Note that the contributions from  $K$  and  $K'$  largely cancel leading to the result that the pressure is dominated by the term involving the density derivative of the symmetry energy.

The density dependence of the symmetry energy is constrained by laboratory data such as nuclear mass fits, giant dipole resonances, and neutron skin thicknesses of neutron-rich nuclei. However, significant difficulties are encountered in obtaining the quantity  $S'_v$  in the necessary supra-nuclear density range. First of all, nuclei sample nucleonic matter in the density range  $n < n_s$ . However, to determine neutron star radii, we need the symmetry energy in the range  $n_s$  to  $2n_s$ . Secondly, nuclear mass fits and giant dipole resonance data predict a strong correlation between the volume symmetry energy  $S_v$  and the surface symmetry energy

$S_s$  parameters in a liquid-drop sense. Neutron skin thickness is predicted to be proportional to the ratio  $S_s/S_v$ . If the nuclear energy per baryon can be expressed as in Eq. (20), a simplified Thomas-Fermi model for the nucleus shows that  $S_s/S_v$  and the neutron skin thickness are proportional to the integral quantity Refs. [74, 75]

$$\int_0^{n_s} \frac{(S_v/E_{sym}(n) - 1)}{\sqrt{n(E(n, 1/2) + 16)}} dn. \quad (25)$$

Although  $S'_v$  is constrained by this relation, it cannot be uniquely determined from it.

## V. NEUTRON STAR CRUSTS AND THEIR CONSTRAINTS

There are a number of observations that pertain to properties of the neutron star crust, which specifically is the region between the nuclear surface and the phase transition separating uniform nuclear matter and matter containing nuclei. The phase transition occurs at about  $1/3$  to  $1/2$   $\rho_s$ , or about  $10^{14}$  g cm $^{-3}$ , depending on the nuclear compression modulus and the density dependence of the nuclear symmetry energy. For example, if pulsar glitches are due to interactions between the neutron superfluid confined to the crust and the bulk of the star, the rate of angular momentum transfer can be related to the fraction of the moment of inertia of the star which resides in the crust [76]. Quasi-periodic oscillations observed in X-ray emission following X-ray bursts on neutron stars are likely related to fundamental and overtone vibrational frequencies of neutron star crusts [77]. Finally, the cooling observed over the first several years following superbursts from neutron stars or giant flares from magnetars is likely due to the cooling of the crust and can be a sensitive indicator of its extent [78].

### A. Theoretical considerations

It is possible to relate both the relative thickness of the crust,  $\Delta/R$ , and the relative fraction of the moment of inertia contained in the crust  $\Delta I/I$ , to the mass, radius and a single parameter of the core-crust interface which depends on the EOS. To see this, first consider the crust thickness  $\Delta = R - R_t$  where  $R_t$  is the radius of the core-crust interface. Begin with hydrostatic equilibrium in the crust, setting  $M(r) = M$ , ignoring  $P$  relative to both  $\epsilon$  and to  $Mc^2/4\pi R^3$ , and ignoring the internal energy per baryon compared to  $m_b c^2$ . Then, since  $\rho \simeq m_b n$ ,

$$\frac{dp(r)}{m_b n} = \frac{d\mu}{m_b} = -\frac{GM}{r^2 - 2GMr/c^2} dr, \quad (26)$$

where  $\mu = \mu_n$  is the baryon chemical potential in beta equilibrium. Integrating from the base of the crust (values of physical variables here are denoted by the subscript  $t$ ) to the surface (denoted by subscript 0), Eq. (26) becomes

$$\frac{\mu_t - \mu_0}{m_b c^2} = \frac{1}{2} \ln \frac{r_t(R - 2GM/c^2)}{R(r_t - 2GM/c^2)}. \quad (27)$$

Note that  $r_0 = R$  and  $r_t = R - \Delta$ . Approximately,  $\mu_0 \simeq -9$  MeV. Upon defining

$$\mathcal{H} \equiv e^{2(\mu_t - \mu_0)/m_b c^2}, \quad (28)$$

Eq. (27) can be manipulated to yield

$$\frac{\Delta}{R} = \frac{\mathcal{H} - 1}{\mathcal{H}(1 - 2\beta)^{-1} - 1}. \quad (29)$$

In general,  $\mathcal{H} - 1 \ll 1$ , whence Eq. (29) implies that  $\Delta \propto (1 - 2\beta)R^2/M$ .

In a similar way, one can determine the crustal moment of inertia fraction. One begins with the definition of the moment of inertia in general relativity [79]:

$$I = -\frac{2c^2}{3G} \int_0^R r^3 \omega(r) \frac{dj(r)}{dr} dr = \frac{8\pi}{3c^2} \int_0^R r^4 (\rho(r) + p(r)/c^2) e^{\lambda(r)} j(r) \omega(r) dr, \quad (30)$$

where  $j(r) = e^{-(\nu(r)+\lambda(r))/2}$  and  $\omega(r)$  is the rotational drag. The metric functions  $\nu(r)$  and  $\lambda(r)$  satisfy

$$\frac{d\nu(r)}{dr} = 2G \frac{M(r) + p(r)/c^2}{r(r - 2GM(r)/c^2)}, \quad e^{-\lambda(r)} = 1 - \frac{2GM(r)}{rc^2}, \quad (31)$$

whereas the rotational drag satisfies

$$\frac{d}{dr} \left( r^4 j(r) \frac{d\omega(r)}{dr} \right) = -4r^3 \omega(r) \frac{dj(r)}{dr}. \quad (32)$$

The relevant boundary conditions are

$$\begin{aligned} e^{\nu(R)} = e^{-\lambda(R)} = 1 - 2\beta, \quad j(R) = 1, \quad \frac{dj(R)}{dr} = 0, \quad \omega(R) = 1 - \frac{2GI}{R^3 c^2}, \\ \frac{d\nu(0)}{dr} = \frac{d\lambda(0)}{dr} = \frac{dj(0)}{dr} = \frac{d\omega(0)}{dr} = 0. \end{aligned} \quad (33)$$

Substitution of Eqs. (32) and (33) into Eq. (30) yields

$$I = \frac{c^2}{6G} R^4 \frac{d\omega(R)}{dr}. \quad (34)$$

While these equations are straightforward to solve for a given EOS, it is useful to employ a fit established by Lattimer & Schutz [80] which is valid for realistic hadronic EOSs that permit maximum masses greater than about  $1.6 M_\odot$ :

$$I \simeq (0.237 \pm 0.008) M R^2 (1 + 2.84\beta + 18.9\beta^4) M_\odot \text{ km}^2 \equiv \alpha M R^2 f(\beta), \quad (35)$$

which defines  $\alpha$  and  $f(\beta)$  for future reference.

One can estimate the moment of inertia connected with the crust by employing the right-hand form of Eq. (30) together with hydrostatic equilibrium, Eq. (1), and the approximations  $4\pi r^3 p(r) \ll M(r)c^2$ ,  $M(r) \simeq M$ ,  $j(r)\omega(r) \simeq \omega(R)$ , to find

$$\Delta I = \frac{8\pi}{3c^2} \int_{R-\Delta}^R r^4 (\rho + p/c^2) e^{-\lambda(r)} j(r) \omega(r) dr \simeq \frac{8\pi\omega(R)}{3Mc^2} \int_{R-\Delta}^R r^6 dp. \quad (36)$$

If one assumes that  $p \propto \rho^\gamma$  in the crust, and that  $p(R - \Delta) \equiv p_t$ , the integral  $\int r^6 dp$  is approximately

$$\int_{R-\Delta}^R r^6 dp \simeq R^6 p_t \exp\left(-\frac{6\gamma}{2\gamma - 1} \frac{\Delta}{R}\right). \quad (37)$$

Combining Eqs. (38), (33) and (35), one finds

$$\frac{\Delta I}{I} \simeq \frac{8\pi}{3c^2} \frac{R^4 p_t}{M^2} [\alpha^{-1} f(\beta)^{-1} - 2\beta] \exp\left(-\frac{6\gamma}{2\gamma - 1} \frac{\Delta}{R}\right). \quad (38)$$

Considering the importance of the location of the core-crust interface, it is worthwhile analyzing how this depends upon EOS assumptions. A heuristic determination of  $\mathcal{H}$  can be made as follows. The core-crust interface corresponds to the phase transition between nuclei and uniform matter. The uniform matter is nearly pure neutron matter, with a proton fraction of just a few percent determined by the condition of beta equilibrium. Ignoring the finite size effects due to surface and Coulomb energies of nuclei, one can consider the critical density for which uniform  $npe$  matter becomes unstable to separation into two coexisting phases (one corresponding to nuclei, the other to a nucleonic sea) [81]. This is a first approximation to the actual case, in which surface and Coulomb effects are not negligible and in addition the dense phase disappears when its volume fraction is finite [82]. The weak interactions conserve both baryon number and charge. At zero temperature, the first law of thermodynamics can be written as

$$du = -pdv - \hat{\mu}dq, \quad (39)$$

where  $u$  is the internal energy per baryon,  $v = 1/n$ ,  $q = x - Y_e$  is the charge density,  $x$  is the proton fraction in the baryons,  $Y_e$  is the electron concentration, and  $\hat{\mu} = \mu_n - \mu_p = \mu_e$  from beta equilibrium. Stability of the uniform phase requires that  $e(v, q)$  is convex [83], or

$$-\left(\frac{\partial p}{\partial v}\right)_q - \left(\frac{\partial p}{\partial q}\right)_v \left(\frac{\partial q}{\partial v}\right)_\mu > 0, \quad \text{and} \quad -\left(\frac{\partial \hat{\mu}}{\partial q}\right)_v > 0. \quad (40)$$

We assume baryonic and electronic energies of the form Eqs. (20) and (21), which we rewrite as

$$E_N \simeq V(n) + E_{sym}(n)(1 - 2x)^2, \quad E_e = \frac{3}{4}Y_e\hat{\mu}. \quad (41)$$

The beta equilibrium condition is

$$\hat{\mu} = 4E_{sym}(n)(1 - 2x) = \hbar c(3\pi^2nx)^{1/3}, \quad (42)$$

where charge neutrality  $x = Y_e$  is used. The conditions in Eq. (40) therefore become equivalent to

$$n^2 \frac{d^2V}{dn^2} + 2n \frac{dV}{dn} + (1 - 2x)^2 \left[ n^2 \frac{d^2E_{sym}}{dn^2} + 2n \frac{dE_{sym}}{dn} - 2E_{sym}^{-1} \left( n \frac{dE_{sym}}{dn} \right)^2 \right] > 0$$

$$-\left(\frac{\partial q}{\partial \hat{\mu}}\right)_v = \frac{1}{8S_v} + \frac{3Y_e}{\hat{\mu}} > 0. \quad (43)$$

The second of these is always true, so the first one determines stability.

As an example, consider the following simple density dependences for  $V$  and  $E_{sym}$ :

$$V(n) = -16 + \frac{K}{18} \left(1 - \frac{n}{n_s}\right)^2, \quad E_{sym}(n) = T_k \left(\frac{n}{n_s}\right)^{2/3} + (S_v - T_k) \left(\frac{n}{n_s}\right)^i, \quad (44)$$

where the kinetic contribution to the symmetry energy is  $T_k \simeq 13$  MeV. A convenient parameter describing the density dependence is  $S'_v$ , defined by

$$n_s \frac{S'_v}{S_v} = \left( \frac{d \ln E_{sym}}{d \ln n} \right)_{n_s} = \frac{2T_k/3 + i(S_v - T_k)}{S_v}. \quad (45)$$

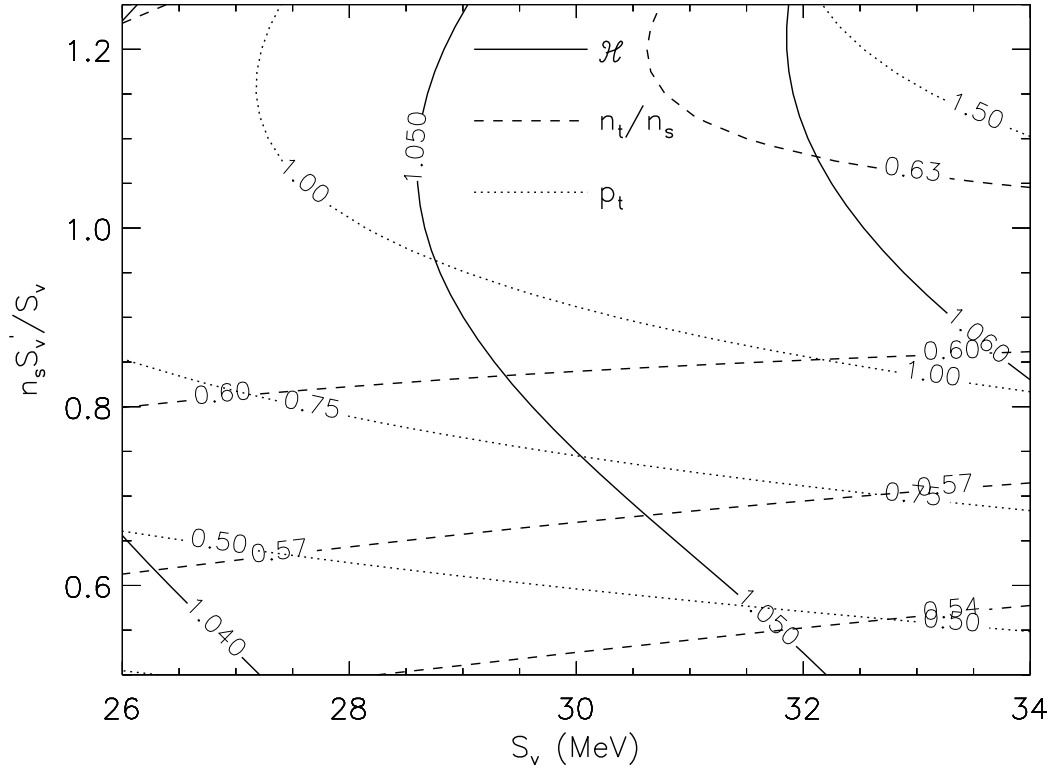


FIG. 5: Contours of enthalpy  $\mathcal{H}_t$ , transition density  $n_t/n_s$ , and pressure  $p_t$  are displayed as functions of  $S_v$  and the logarithmic derivative of  $E_{sym}$  at  $n_s$  for the simple model described by Eq. (44).

Applying the stability condition Eq. (43) determines the phase boundary density  $n_t$ . For reasonable ranges of  $S_v$  and  $S'_v$ , one finds  $0.5 < n_t/n_s < 0.7$  as seen in Fig. 5. The quantity  $\mathcal{H}$  is related to the neutron chemical potential,

$$\mu_n(n_t) = -16 + \frac{K}{18} \left(1 - \frac{n_t}{n_s}\right) \left(1 - 3\frac{n_t}{n_s}\right) + E_{sym}(n_t)(1 - 4x_t^2) + \left(n \frac{dE_{sym}(n)}{dn}\right)_{n_t} (1 - 2x_t)^2, \quad (46)$$

by Eq. (28). The pressure at the boundary,  $p_t$ , is given by

$$p_t = \frac{K n_t^2}{9 n_s} \left(\frac{n_t}{n_s} - 1\right) + n_t(1 - 2x_t) \left[ x_t E_{sym}(n_t) + \left(n \frac{dE_{sym}(n)}{dn}\right)_{n_t} (1 - 2x_t) \right]. \quad (47)$$

The quantities  $\mathcal{H}$  and  $p_t$  at the phase boundary are also shown in Fig. 5 for this simple model, using  $n_s = 0.16 \text{ fm}^{-3}$  and  $K = 225 \text{ MeV}$ . The boundary density  $n_t$  and  $p_t$  are *much more sensitive to the density dependence of the symmetry energy than to  $S_v$  or  $K$* . The general traits found in this simple model apply to realistic EOSs. In particular, for realistic EOSs [6],

$$1.04 \leq \mathcal{H} \leq 1.07; \quad 0.20 \text{ MeV fm}^{-3} < p_t < 0.65 \text{ MeV fm}^{-3}. \quad (48)$$

These ranges are measures of the current uncertainty in the density dependence of the symmetry energy. The range of values for  $\mathcal{H}_t$  found for the simple model (and shown in Fig. 5) is very similar. However, the realistic values for  $p_t$  are somewhat smaller than predicted by the simple model, due to the neglect of finite-size effects. Finite-size effects are much less significant for the neutron chemical potential.

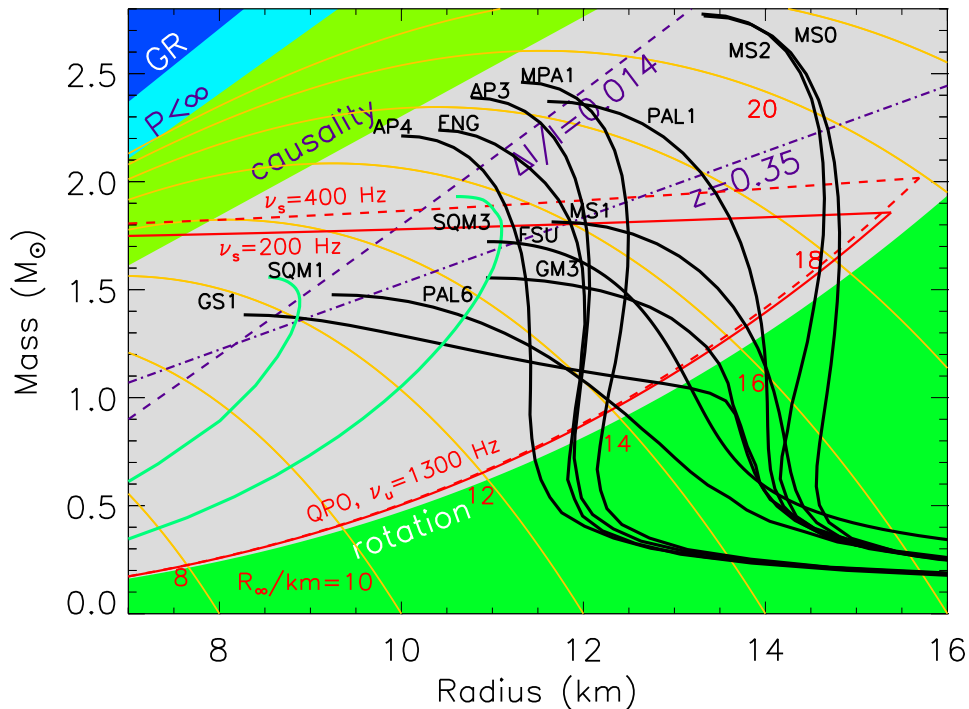


FIG. 6: The same as Fig. (2), but with additional contours of fixed redshift  $z = 0.35$  (dot-dashed blue line), crustal fraction of moment of inertia  $\Delta I/I = 0.14$  (dashed blue line), and QPO constraints (red solid and dashed lines). For the Vela pulsar, the  $\Delta I/I$  constraint and the assumption that the pressure at the core-crust interface satisfies  $p_t < 0.65 \text{ MeV fm}^{-3}$  implies that allowed masses and radii lie to the right of the dashed line [76].

### B. Observational application 1: Pulsar glitches

Pulsar glitches, which are sudden discontinuities in the spin-down of pulsars, seem to involve the transfer of angular momentum from an isolated component to the entire star. A leading model for glitches supposes that the isolated component consists of superfluid neutrons in the crust [84]. As the star spins down due to pulsar electromagnetic emissions, the superfluid component's angular velocity differs to a greater and greater extent from that of the non-superfluid component. When this differential becomes large enough, angular momentum is suddenly transferred from the superfluid component to the non-superfluid part through vortex unpinning. In the case of the Vela pulsar, some 30 years of observations indicate a steady overall angular momentum transfer rate that indicates at least 1.4 of the total moment of inertia of the star is involved with the isolated component [76]. Eq. (36) indicates that the crustal fraction of the moment of inertia is most sensitive to the pressure at the transition from the crust to the core. The location of the transition and the pressure there are sensitive to, among other nuclear parameters, the density dependence of the nuclear symmetry energy. Using the upper limit of  $p_t$  from Eq. (48) in Eq. (38) allows one to set a minimum  $R$  for a given  $M$  for Vela [76] which is displayed in Fig. 6 and is approximately:

$$R \geq 3.6 + 3.9 \frac{M}{M_\odot} \text{ km}. \quad (49)$$

Better understanding of the nuclear symmetry energy would permit a lower upper limit of  $p_t$  to be determined, which could tighten this constraint.

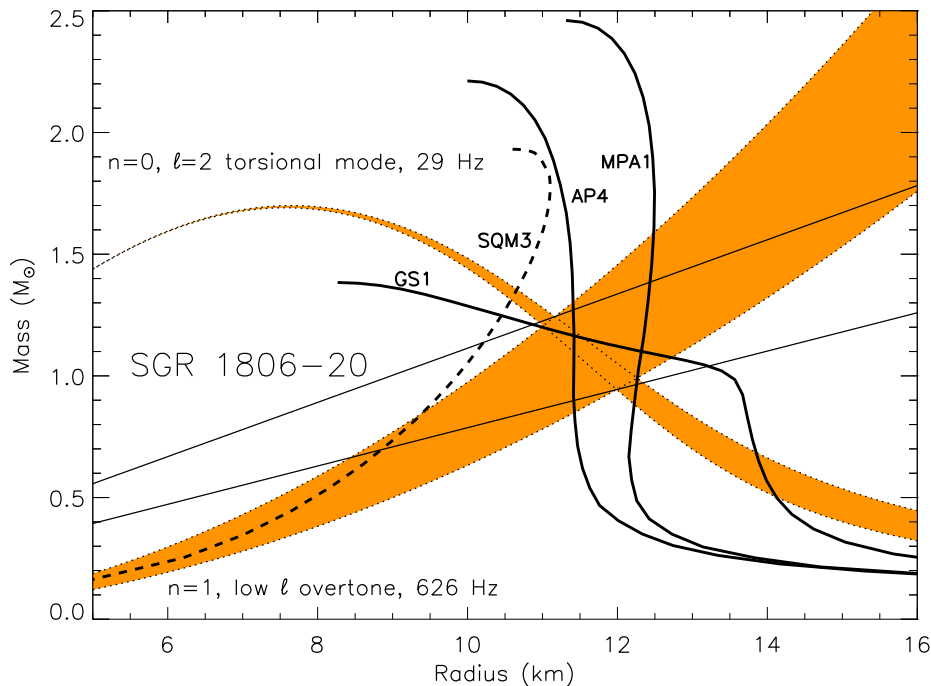


FIG. 7: Mass-radius diagram showing the constraints from neutron star seismology from the soft gamma-ray repeater SGR 1806-20.  $\mathcal{H}$  values in the range 1.04 (lower boundaries of permitted regions) to 1.07 (upper boundaries) were assumed. A few representative  $M - R$  curves from Fig. 2 are shown for reference. The straight lines follow the values of  $\beta(\mathcal{H} = 1.04) = 0.116$  and  $\beta(\mathcal{H} = 1.07) = 0.165$ , determined from the observed frequencies, and show how the  $(M, R)$  values change as the shear velocities are varied.

It should be pointed out that the standard picture of the outer core, in which superfluid neutrons coexist with type II superconducting protons, has been challenged by Link [85]. He notes that observations of the long-term precession in several pulsars indicates an incompatibility with creeping neutron vortices, which predict too large precession frequencies. Furthermore, the observations seem to require that the vortices of the inner crust must be able to move with little dissipation with respect to the solid, which could be incompatible with a neutron superfluid in the crust in precessing neutron stars. Nevertheless, since there is no evidence as yet that the Vela pulsar is precessing, Link’s argument may not apply to this pulsar. Why some stars show precession and others do not is an unsolved problem, and until this is better understood, radius limits based upon glitches remain tentative.

### C. Observational application 2: Neutron star oscillations

Another kind of limitation on radii can be obtained from observations of quasi-periodic oscillations in the X-ray emissions following giant flares in three soft gamma-ray repeaters, SGR 0526-66 [86], SGR 1806-20 [87] and SGT 1900+14 [88], presumably due to torsional vibrations of the star’s crust [77]. Neglecting magnetic fields and the effects of superfluids in the crust, the frequencies of the fundamental mode and overtones have been estimated [89] to be

$$\omega_{n=0,\ell=2} = 2v_t \sqrt{\frac{e^\nu}{RR_t}}, \quad \omega_{n>0} = e^{(\nu-\lambda)/2} \frac{n\pi v_r}{\Delta}, \quad (50)$$

where  $\nu$  and  $\lambda$  refer to the average values of the metric functions, and  $v_r$  and  $v_t$  are the average radial and transverse shear speeds, respectively. Higher order modes ( $\ell > 2$  in the case  $n = 0$  and  $\ell > 1$  in the case  $n > 0$ ) are ignored for a simple analysis. To a good approximation, one may assume  $e^\nu = e^{-\lambda} = 1 - 2\beta$ . In the isotropic limit,  $v_r = v_t$  and we assume this; the shear velocities are of order  $10^8$  cm s $^{-1}$ . Since the crust thickness  $\Delta$  is small compared to  $R$  one has, roughly,  $\omega_{n=0} \propto R_\infty^{-1}$ , where  $R_\infty = R/\sqrt{1-2\beta}$  is the so-called radiation radius (see §VI). Also,  $\omega_{n>0} \propto (1-2\beta)/\Delta \propto R^2/M$ .

Following the general approach of reference [89], in which this simple analysis is compared to more sophisticated numerical models, one can write, using Eq. (29) for  $\Delta/R$ , the frequencies ( $f = \omega/2\pi$ )

$$\begin{aligned} f_{n=0,\ell=2} &\simeq 263.3 \left(\frac{\text{km}}{R}\right) \sqrt{\frac{(\mathcal{H}-1+2\beta)(1-2\beta)}{\beta\mathcal{H}}} \text{ Hz}, \\ f_{n>0} &\simeq 1170n \left(\frac{\text{km}}{R}\right) \frac{\mathcal{H}-1+2\beta}{\mathcal{H}-1} \text{ Hz}. \end{aligned} \quad (51)$$

If more than one frequency can be measured, these relations can be used to uniquely identify  $R$  and  $\beta$ , that is,  $R$  and  $M$ , modulo uncertainties in  $\mathcal{H}$ .

The chief model dependence of the above approach lies in the velocities  $v_r$  and  $v_t$ . In the above, they are taken to be equal and are fitted to numerical simulations ignoring magnetic fields and superfluidity. In a more realistic analysis, they could differ from these values. However, if  $v_r \simeq v_t$ , Eqs. (51) indicates that  $\beta(\mathcal{H})$  can be found by eliminating  $R$ : it is the solution of a quadratic equation.

The soft gamma-ray repeater SGR 1806-20 has quasi-periodic oscillations which correspond to the  $n = 0, \ell = 2, 6, 10$  and  $n = 1, \ell = 1$  modes [89]. The identification of the larger  $\ell$  modes is more speculative, but the frequencies  $f_{n=0,\ell=2} \simeq 29$  Hz and  $f_{n=1,\ell=1} \simeq 626.5$  Hz are claimed. Fig. 7 shows the allowed regions in the mass-radius plane for the two modes, and their overlap, assuming  $1.04 \leq \mathcal{H} \leq 1.07$ . It is clear that the overtones are much more sensitive to assumptions about  $\mathcal{H}$  (an EOS attribute) than is the fundamental mode. The two values of  $\beta$  associated with these values of  $\mathcal{H}$  are  $\beta(\mathcal{H} = 1.04) = 0.116$  and  $\beta(\mathcal{H} = 1.07) = 0.165$ , respectively. Because lines of constant  $\beta$  are approximately parallel to the overtone constraint, but perpendicular to the fundamental mode constraint, uncertainties in the velocity would be reflected as relatively larger uncertainties in the latter than the former.

#### D. Observational application 3: Thermal relaxation of the crust

After the formation of a proto-neutron star in the aftermath of a gravitational collapse supernova event, cooling of the core proceeds via neutrino emission, leading to temperatures of order  $10^9$  K within years (see §VIII). During this period, the star is not in complete thermal equilibrium due to the relatively long thermal relaxation time of the crust, which is expected to be of order 10 to 100 years [90]. The excess heat of the crust is preferentially transported by electron conduction into the star's isothermal core, dominating radiation by thermal emission from the surface. However, after a time which we will denote by  $t_w$ , the surface will finally come into thermal equilibrium with the core, causing a reduction in the surface temperature. Depending upon whether or not the core neutrino emission processes are rapid or conventional (see the terminology in §VIB), the drop in surface temperature will be a factor of 2 (and relatively slow) to 10 (and relatively abrupt). Following this reduction, the surface temperature stabilizes at a value about 100 times the core temperature [91]. The time  $t_w$  is simply related to the thermal conductivity and specific heat of the crust, its thickness, and redshift [90, 92], so that its observation could be used to constrain neutron star structure and composition.

In addition, some accreting neutron stars are observed to undergo long-duration X-ray bursts, sometimes called superbursts, which appear to be powered by thermonuclear He fusion. During the burst, some

of the heat is transported into the interior, warming the crust. Observations of quiescent thermal emission following the bursts would therefore probe the thermal relaxation timescale of the crust as well as the rate of core neutrino emission [78]. It is therefore useful to investigate the relation between the thermal relaxation time and the structure of neutron stars.

To begin, it is necessary to supplement the hydrostatic equilibrium equations, Eq. (1), with those of relativistic heat transport,

$$\begin{aligned} L_\nu &= -4\pi r^2 K e^{-(\lambda-\nu)/2} \frac{\partial T e^{\nu/2}}{\partial r}, \\ \frac{\partial e^\nu L_\nu}{\partial r} &= -4\pi r^2 e^{(\lambda+\nu)/2} C_V \frac{\partial T}{\partial t}, \end{aligned} \quad (52)$$

where  $L_\nu(r)$  is the local neutrino luminosity,  $C_V$  is the specific heat capacity at fixed volume, and  $K$  is the thermal conductivity. Explicit neutrino emission is neglected in Eq. (52). Following thermal relaxation, the redshifted temperature  $T(r)e^{\nu(r)/2}$  becomes constant within the star. Applying these equations to the crust, and assuming  $\Delta/R \ll 1$  so that  $e^\nu \simeq e^{-\lambda} \simeq \sqrt{1 - 2GM/Rc^2}$  throughout the crust, and defining  $x = (R - r)/\Delta$ , one finds

$$\left(\frac{R}{\Delta}\right)^2 \frac{\partial}{\partial x} \left[ K \frac{\partial T}{\partial x} \right] = C_V e^{3\lambda/2} \frac{\partial T}{\partial t}. \quad (53)$$

If it is assumed that the conductivity  $K$  and specific heat  $C_V$  can each be written as separable functions of density and temperature, then one can make the same assumption for  $T$ :  $T(r, t) = T_0 \psi(r) \phi(t)$ . Generally,  $C_V \propto T$ , and  $K \propto T^0$  or  $T$  depending on density. The temporal dependence  $\phi$  in these two cases is then either linear or quadratic:  $\phi = 1 - t/t_w$  or  $\phi = \sqrt{1 - t/t_w}$ , where the thermal lifetime of the crust is

$$t_w \propto \Delta^2 e^{3\lambda/2}, \quad (54)$$

with the proportionality constant scaling as  $C_V/K$ . This behavior is borne out in detailed numerical simulations of neutron star cooling [90] in which, for superfluid crusts,

$$t_w \sim 5 \left(\frac{\Delta}{\text{km}}\right)^2 \left(1 - \frac{2GM}{Rc^2}\right)^{-3/2} \text{ yr}. \quad (55)$$

For non-superfluid crusts, the cooling times are about a factor of 3.5 times larger.

Although no newly-formed neutron stars have ever been observed so young as to show this surface temperature drop, it has been suggested that the reason magnetars (highly magnetized neutron stars) have abnormally large surface temperatures is that they have heat sources (presumably powered by magnetic field decay) located in a thin layer in the outer crust [93]. If the heat source was located deeper, the energy would be radiated efficiently by neutrinos and could not heat the crust. This heat source warms up the crust and produces an inhomogeneous temperature distribution within the star, with parts of the crust much warmer than the deep crust and core. The thermalization times calculated above are consistent with observations, but tell us more about the heat source than about structural constraints.

This theory can be applied to superbursts or other cases in which the crust is heated for a long-enough duration that the crust thermalizes throughout. For example, observations of the soft X-ray transient 1H 1905+000, which underwent a burst about 20 years ago, indicate that the crust cooling times are somewhat shorter than Eq. (55) predicts, suggesting that the crust's thermal conductivity is higher than expected or that enhanced core neutrino cooling is taking place [94]. Another source, KS 1731-260 [95, 96], which produced a superburst lasting about 12 years, went into quiescence and has since shown a strong decline of X-ray luminosity, also suggesting a high thermal conductivity for the crust and rapid neutrino core cooling. Further work needs to be done, however, to test the assumption that the crusts of these sources are being heated to complete thermal equilibrium as otherwise shorter cooling times might be expected.

## VI. COOLING NEUTRON STARS

### A. Observations of thermal emission

The quantity inferred from thermal observations of a neutron star's surface is the so-called radiation radius

$$R_\infty = R/\sqrt{1 - 2GM/Rc^2}, \quad (56)$$

which results from a combination of flux and temperature measurements, both redshifted at the Earth from the neutron star's surface. For example, the un-redshifted Kirchoff's law for a black body,

$$F = \left(\frac{R}{d}\right)^2 \sigma T^4, \quad (57)$$

becomes

$$F_\infty = \left(\frac{R_\infty}{d}\right)^2 \sigma T_\infty^4 \quad (58)$$

when redshifted to the Earth. Contours of the quantity  $R_\infty$  are displayed in Fig. 2. A measured value of  $R_\infty$  sets upper limits to both  $R$  and  $M$ , but without an independent estimate of mass or radius only limited constraints are possible. The major uncertainties involved in the determination of  $R_\infty$  include the distance, interstellar H absorption that is important near the peak and at lower energies of the spectrum, and details concerning the composition of the atmosphere and its magnetic field strength and structure. The most reliable measurements will originate from sources for which one or more of these uncertainties can be controlled. For example, the nearby sources RX J1856-3754 [97] and Geminga [98] have measured parallaxes, and the quiescent X-ray binaries in globular clusters for which reliable distances are (or will soon be) available. In addition, the X-ray binaries in globular clusters, having undergone recent episodes of accretion, are expected to have low magnetic field H-rich atmospheres, presumably, the simplest of all situations.

A characteristic of these X-ray sources, in the cases in which the distances are small enough to allow detection of optical emission, is that the optical fluxes are a factor  $f \simeq 5 - 7$  times the amount expected from extrapolating the X-ray blackbody fits onto the Rayleigh-Jeans tail. This is one consequence of the neutron star atmosphere and its redistribution of the flux from a simple blackbody. The slope of the Rayleigh-Jeans tail is a measure of the optical temperature, and typically  $T_{opt} \sim T_X/2$ . Therefore, in order to properly fit the overall flux distribution, a larger radius is needed than the X-ray fit alone would imply. The optical flux may be written as

$$F_{opt} \propto 4\pi \left(\frac{R_{opt}}{d}\right)^2 T_{opt} = 4\pi f \left(\frac{R_X}{d}\right)^2 T_X, \quad (59)$$

whereas the total stellar radius is a function of the effective optical and X-ray radii:

$$R = \sqrt{R_{opt}^2 + R_X^2} = R_X \sqrt{1 + \frac{T_X}{T_{opt}} f} \simeq R_X \sqrt{1 + 2f}. \quad (60)$$

This explicitly shows that a factor  $f \sim 5 - 7$  results in an increase in inferred radius of about a factor 3-4 over that inferred from X-rays alone. Radii inferred from X-ray data alone are therefore suspect, and often much too small.

Results from atmospheric fitting of the data for RX J1856-3754 and various globular cluster sources are displayed in Fig. 8. An interesting feature of Fig. 8 is that if one accepts the results at face value,

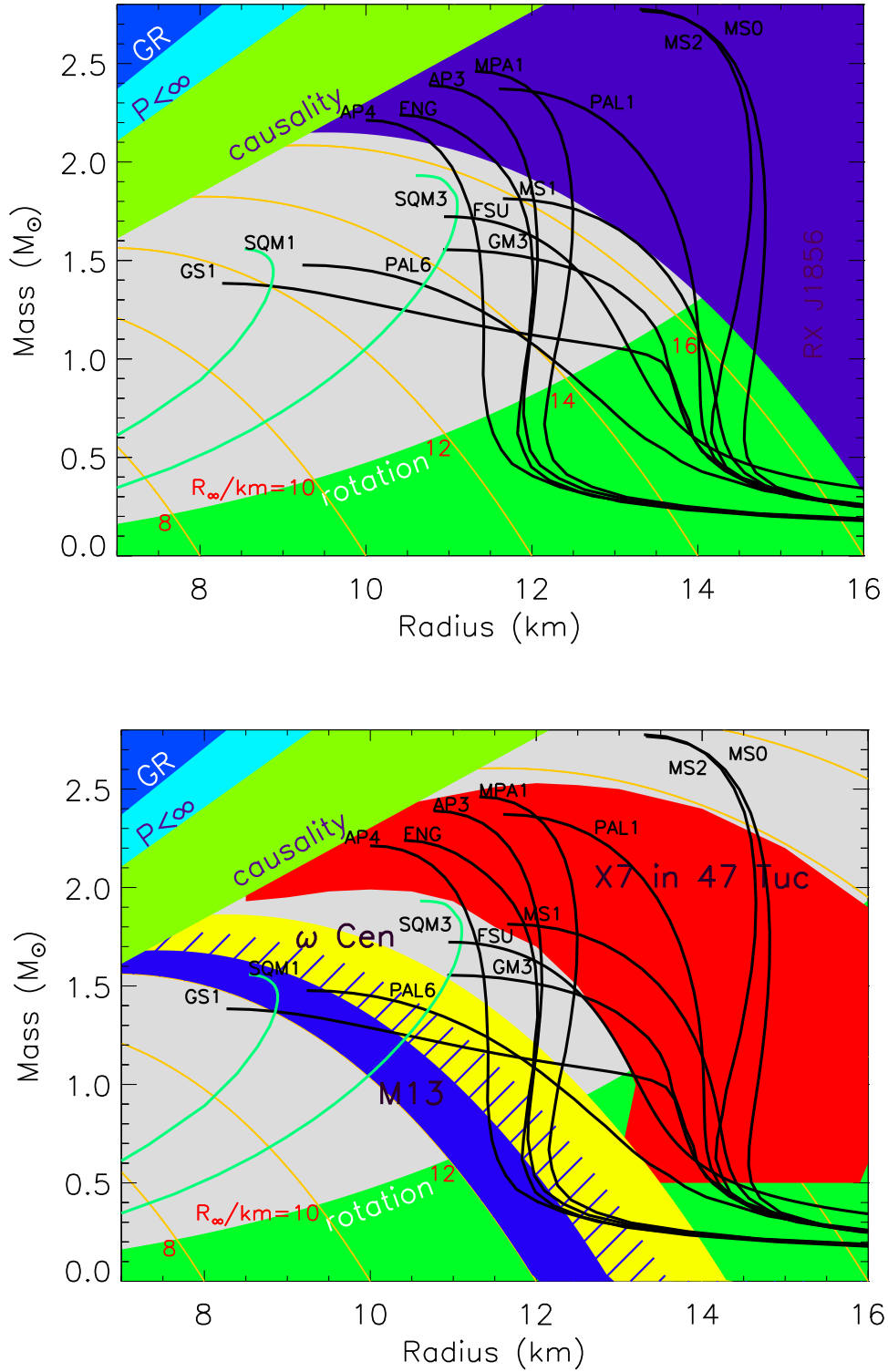


FIG. 8: The same as Fig. 2, but displaying allowed mass and radius regions for thermally-emitting neutron stars. Top panel is for RX J1856-3754 (assuming a distance of 120 pc) [97], while the bottom panel shows results for globular cluster sources in M13 [99],  $\omega$  Cen [100] and 47 Tuc [101].

only EOS curves that pass through all the permitted regions can be accepted. This would eliminate several relativistic field-theoretical EOSs such as GM3, FSU, MS0, MS1 and MS2, while still permitting non-relativistic potential models like AP3 and AP4. (It must be stressed, however, that the approach of Muller & Serot, of which the EOSs MS0, MS1 and MS2 are typical examples, can be straightforwardly generalized to yield results that can accommodate the mass and radius constraints implied in Fig. 8.) The Dirac-Brueckner relativistic field-theoretical models like ENG and MPA1 are allowed. Note that the surviving EOSs all support large masses, which could be crucial if the  $2.1 M_{\odot}$  value for PSR J0751+1807 remains robust.

## B. Implications for neutron star cooling

For many years, it was common to adopt a *standard cooling* scenario, with relatively slow cooling, in which the dominant neutrino processes were the relatively slow modified Urca processes involving nucleons. However, neutrino production would become significantly more rapid if the symmetry energy and proton fraction is large or in the presence exotic matter such as hyperons, kaons or deconfined quarks, which would permit the direct Urca processes [102, 103].

The direct Urca process involving baryons is the simple weak decays and the reverse reactions

$$B_1 \rightarrow B_2 + \ell + \bar{\nu}_{\ell}; \quad B_2 + \ell \rightarrow B_1 + \nu_{\ell}, \quad (61)$$

where  $B_1$  and  $B_2$  are baryons, and  $\ell$  is a lepton, either an electron or a muon. When the decaying baryon is a neutron, the occurrence of this process is contingent upon the presence of a sufficient number of protons (determined entirely by the density dependent symmetry energy) so that energy and momentum can be conserved simultaneously.

In contrast to the direct Urca process, the modified Urca process includes a bystander baryon that facilitates the simultaneous conservation of energy and momentum. The additional particle slows the neutrino energy emission rate by a factor  $\sim (T/T_F)^2$ , where  $T_F \sim 30$  MeV is the Fermi energy at the equilibrium density  $n_s$ . Since a typical temperature is of order  $0.1 - 1.0$  MeV, the modified Urca rate is millions of times slower than the direct Urca rate. However, the direct Urca process becomes possible, albeit with a smaller strength (matrix element), when a Bose condensate, deconfined quarks, or hyperons are present.

The paradigm of slow standard (as opposed to rapid exotic) behavior stemmed from models of the nuclear force which had relatively small isospin dependences, such that the beta equilibrium proton and electron fractions would be very small and the direct Urca process among baryons would be forbidden. With the realization that newer versions of nuclear force models have greater isospin dependence and predict larger proton fractions has come the possibility that the direct Urca process can occur even in the absence of exotic matter [102]. Therefore, the detection of a rapidly cooling neutron star is not sufficient to unambiguously prove the existence of exotic matter in a neutron star interior. Compounding the difficulty of interpreting cooling observations is the role of superfluidity, which can turn off the direct Urca process near the superfluid's critical temperature.

While it is outside the intended scope of this review to develop the details of neutron star cooling (see, *e.g.*, Ref. [104] and references therein), it should be clear that it sensitively involves the internal composition. Inasmuch as the internal composition depends on the overall mass of the neutron star, an indirect measure of the mass of the star is possible. This is especially pertinent for those supernova remnants which have yet to yield detectable sources of thermal emission, such as 3C58 [105], and supernova remnants G084.2-0.8, G093.3+6.9, G127.1+0.5 and G315.4-2.3 [106]. If these remnants in fact contain neutron stars, the stars may have cooled rapidly due to one of the several direct Urca processes, which

is much more efficient than standard cooling due to the modified Urca process. Stars with high proton fractions may cool via the direct Urca process, and this depends upon the density dependence of the symmetry energy. A radiation radius determination for the same star would allow an extraction of the radius itself.

## VII. OTHER RADIUS OBSERVABLES

Besides measurements of radiation radii from cooling neutron stars, their limits to the radius could be set by pulse profiles, redshifts, explosions or accretion on neutron star surfaces with Eddington-limited fluxes, quasi-periodic oscillations (QPO's) from accreting neutron stars, and measurements of the moment of inertia of binary pulsars. We highlight these avenues in turn below.

### A. Pulse profiles

Gravitational lensing strongly suppresses the amplitude of variations from pulsing (rotating) neutron stars. Essentially, gravitational light-bending allows an observer to see much more than the facing hemisphere. Therefore, analysis of pulsations in the thermal emission from pulsars allows limits to be placed on the ratio  $M/R$ . The locally emitted flux is proportional to the local temperature to the fourth power, which varies since it is controlled by the local magnetic field strength. Assuming dipole fields, it has been shown for many pulsars that pulse fractions comparable to the observed ones can be obtained only with stellar radii larger than those which are predicted by current models of neutron star structure, or with low stellar masses [59]. However, different field geometries can alter this conclusion.

The same physics influences other pulsed emissions from neutron stars, such as Her X-1, which is an eclipsing X-ray emitting source with X-ray pulsations. The emission is observed to be occulted by the inner-disk edge which implies that the neutron star emits a pencil beam from its near pole and a fan beam from its far pole [60]. Gravitational light-bending strongly influences the emission, and Leahy [61] derived  $M/R \simeq 0.121 - 0.128 M_{\odot} \text{ km}^{-1}$ , or  $z \simeq 0.247 - 0.268$ , for this source. For the inferred mass of Her X-1,  $1.29 - 1.59 M_{\odot}$  [34], this translates into a radius range  $10.1 < R/\text{km} < 13.1$ . This result may be model dependent, and more complex geometries and emissivities should be considered, but it nevertheless indicates the potential of the technique.

### B. Redshift

Another observable is the redshift

$$z = \left(1 - \frac{2GM}{Rc^2}\right)^{-1/2} - 1. \quad (62)$$

Possibly the best case is that of the active X-ray burster EXO 0748-676 [107] for which a pair of resonance scattering lines consistent with Fe XXV and XXVI imply  $z \simeq 0.345$ . Later, 45 Hz oscillations in the average power spectrum of 38 thermonuclear X-ray bursts were found and interpreted as the neutron star spin frequency [108]. Furthermore, the widths of the lines observed by Ref. [107] are consistent with this spin frequency as long as the star's radius is between about 10 and 15 km [108]. However, the spectral identification of Ref. [107] is not universally accepted [109]. Importantly, as long as the star's spin frequency is less than about 600 Hz, the measured  $z$ , which refers to the equatorial radius of the spinning star, is less than 2% different to that of the non-spinning star [110]. More observations and

better modeling of the line profiles could lead to additional parameters involving  $M$  and  $R$  and serve as useful constraint. Other sources with lines have been claimed, but never confirmed with more sensitive instruments.

Clearly, a simultaneous measurement of  $R_\infty$  and  $z$  would determine both  $M$  and  $R$ :

$$\begin{aligned} R &= R_\infty(1+z)^{-1}, \\ M &= \frac{c^2}{2G}R_\infty(1+z)^{-1}[1-(1+z)^{-2}]. \end{aligned} \quad (63)$$

The contour  $z = 0.35$  is shown in comparison to typical mass-radius curves in Fig. 6. However, it is often the case that it is the quantity  $R_\infty/d$  that is determined, where  $d$  is the distance to the source, which is often uncertain.

It is expected that planned X-ray missions, like Constellation-X which has a resolution and effective area several times larger than Chandra and XMM, will discover and precisely measure more spectral lines from neutron star surfaces.

### C. Eddington limit

A major hurdle in determining radii from observations of thermal radiation from cooling neutron stars is that the distances,  $d$ , to the sources are generally not well known. Even if a source's redshift can be determined, an additional relation involving  $M$ ,  $R$  and/or  $d$  is needed to independently find  $M$  and  $R$ . Burst sources, which are believed to involve thermonuclear X-ray bursts on neutron star surfaces, have long been known to have peak fluxes that are to order of magnitude comparable to the Eddington limited flux:

$$F_{edd,\infty} = \frac{cGM}{\kappa d^2} \sqrt{1 - 2GM/Rc^2}, \quad (64)$$

where  $\kappa$  is the opacity. If the opacity is assumed to be dominated by electron scattering, one has

$$\kappa = 0.2(1+X) \text{ cm}^2 \text{ g}^{-1}, \quad (65)$$

where  $X$  is the hydrogen mass fraction. Following a burst, the source apparently relaxes to a quiescent state, which is believed to involve the radiation of thermal emission. Study of the X-ray spectrum can then yield a cooling flux and temperature  $F_\infty$  and  $T_\infty$  observed at Earth:

$$F_\infty/(\sigma T_\infty^4) = (T_{eff}/T_\infty)^4 R^2 d^{-2} (1 - 2GM/Rc^2)^{-1}, \quad (66)$$

where  $T_{eff}$  is the effective temperature and  $T_\infty$  is the observed color temperature. The ratio  $T_{eff}/T_\infty$  is a color correction factor that depends on the composition, gravity and  $T_{eff}$  [111].

If the observed peak flux is approximately the Eddington flux, if the opacity and color correction factor are well-understood, if the quiescent flux observed in-between bursts is thermal emission with a measureable temperature  $T_\infty$ , and if spectral features are observed which permit a determination of the object's redshift, these multiple observations then contain the information needed to identify uniquely the mass and the radius of a single star. To make this clear, combine Eqs. (62), (64) and (66):

$$\begin{aligned} M &= \frac{c^5}{4G\kappa F_{edd,\infty}} \alpha [1 - (1+z)^{-2}]^2 (1+z)^{-3}, \\ R &= \frac{c^3}{2\kappa F_{edd,\infty}} \alpha [1 - (1+z)^{-2}] (1+z)^{-3}, \end{aligned}$$

$$d = \frac{c^3}{2\kappa F_{edd,\infty}} \frac{\sqrt{\alpha}}{[1 - (1+z)^{-2}](1+z)^{-2}}. \quad (67)$$

In the above, the factor  $\alpha = (T_\infty/T_{eff})^4 F_\infty/(\sigma T_\infty^4) = (R_\infty/d)^2$ . The burst source EXO 0748-676 is especially amenable to analysis [112], as this is one of the few sources with an estimated redshift (see above),  $z = 0.345$ . Its peak flux, to be identified with  $F_{edd}$ , is  $2.25 \pm 0.23 \times 10^{-8} \text{ erg cm}^{-2} \text{ s}^{-1}$ , and the ratio  $F_\infty/(\sigma T_\infty^4)$  is observed to be  $1.14 \pm 0.10 \text{ (km/kpc)}^2$ . Using Eqs. (67) and these observables, along with standard assumptions for  $\kappa$  and  $T_\infty/T_{eff}$ , Ozel [112] finds for this burst source  $M = 2.1 \pm 0.28 M_\odot$ ,  $R = 13.8 \pm 1.8 \text{ km}$ , and  $d = 9.2 \pm 1.0 \text{ kpc}$ . These errors do not include uncertainties in the assumed opacity or color-corrections.

Note, however, that statistical studies [113] indicate that the average maximum luminosity of X-ray bursts at infinity are about 60% larger than Eq. (64) predicts. Various suggestions have been proposed to explain the super-Eddington luminosities in these bursts. Additionally, the value of  $\kappa$  is as yet difficult to ascertain to good precision because the composition is uncertain and contributions from bound-free opacities are uncertain. Nevertheless, if these problems can be addressed, observations of this source could ultimately lead to the simultaneous determination of the mass and radius of a neutron star. In short, this is a promising avenue to pursue as it holds the promise to establish the mass and radius of the same neutron star.

An interesting variation of the theme of the Eddington flux concerns the emission from neutron stars from accretion in low-mass X-ray binaries (LMXBs). In the spreading layer model [114], accreting matter spreads from the equator to the poles on the neutron star surface, locally radiating at the Eddington flux. The total emission can approach the Eddington limit if the matter spreads all the way from the equator to the poles. Calculations indicate that the overall emitted spectrum is that of a diluted blackbody. Schematically, the effective temperature of the radiation (*i.e.*, the Eddington temperature  $T_{Edd}$ , is determined by the balance between surface gravity and radiative acceleration:

$$\frac{GM}{R\sqrt{1 - 2GM/Rc^2}} = \frac{\sigma T_{Edd}^4 \kappa}{c}, \quad (68)$$

where  $\kappa = 0.2(1+X) \text{ cm}^2 \text{ g}^{-1}$  is the electron scattering opacity and  $X$  is the hydrogen mass fraction. The observed color temperature is

$$T_c = T_{Edd} f_c \ell^{1/4} \sqrt{1 - 2GM/Rc^2}, \quad (69)$$

where  $\ell \sim 0.8$  is the correction for centrifugal reduction of gravity and  $f_c$  is a correction factor for spectral hardening. As a result, the neutron star radius can be found from

$$R^2 = \frac{\ell f_c^4 c^3}{2\sigma T_c^4 \kappa} \frac{2GM}{c^2} \left(1 - \frac{2GM}{Rc^2}\right)^{3/2}. \quad (70)$$

This is essentially equivalent to the middle formula in Eq. (67). In practice, modeling of the radiative transfer makes some corrections to the above, but it can be observed that the contours in an  $M - R$  diagram for fixed values of  $T_c$  are nearly orthogonal to contours of  $R_\infty$ , and are less sensitive to variations in  $M$ . For  $1.4 M_\odot$  neutron stars, and taking  $X \sim 1$  and  $2.3 < T_c/\text{keV} < 2.5$  (the observed range in LMXBs), this method implies  $12 < R/\text{km} < 15$  [115]. It is important to note that the spreading layer method only utilizes the color temperature of the source. If the same source could be observed after accretion ceases, the information obtained during accretion could be supplemented during quiescence to independently determine  $M$  and  $R$  as in the preceding analysis for EXO 0748-676.

### D. Quasi-periodic oscillations from accreting stars

Accreting matter in LMXRBs flows from the companion through its inner Lagrangian point into an accretion disc. Through viscous dissipation, the matter slowly loses angular momentum and spirals closer to the neutron star. Eventually, the matter reaches the inner edge of the accretion disc, which is thought to be close to the innermost circular stable orbit (ISCO), which in the Schwarzschild geometry is  $R_{ISCO} = 6GM/c^2$ . Thereafter, the matter quickly spirals onto the neutron star's surface, emitting X-rays as gravitational potential energy is converted into thermal energy. In some of these binaries, 25 so far [116], Fourier analysis of the X-ray emission shows quasi-periodic oscillations, or QPOs. Usually, a frequency of 200-400 Hz is observed, which is thought to be either the spin frequency of the star or half of that. In addition, two high frequency kHz peaks are also seen, separated by the presumed neutron star spin frequency. Explanations of the QPOs range from beat-frequency models connected with the ISCO frequency and the star's spin [117] to vertical epicyclic frequencies or resonant interactions [118]. Observations indicate that these QPOs rise slowly in frequency and suffer a drop in their quality factor as these frequencies saturate at their largest values [119]. The quality factor is the frequency divided by the peak's full width at half maximum. This behavior is what is expected if the drop is produced by the approach of accreting matter to the ISCO. It should be noted that all proposed models connect the upper kHz QPO with the ISCO orbital frequency to within a percent for neutron stars.

Since the orbital frequency at the ISCO is a function of neutron star mass (if the star is rotating slowly), and the inner edge of the accretion disc must lie at or outside the ISCO, the inferred frequency thus provides a limiting mass for the neutron star. Inferred ISCO frequencies range from  $\nu_{ISCO} \simeq 1220$  Hz for 4U 1636-53,  $\nu_{ISCO} \simeq 1230$  Hz for 4U 1608-52, and  $\nu_{ISCO} \simeq 1310$  Hz for 4U 1728-34 [119]. The inferred upper limit to the masses, including the lowest order correction for neutron star spin, is [117]

$$M \leq \left( \frac{2200 \text{ Hz}}{\nu_{ISCO}} \right) \left( 1 + 0.75 \frac{cJ}{GM^2} \right) M_{\odot}, \quad (71)$$

where  $J = 2\pi fI$  is the angular momentum of a star spinning with frequency  $f$ .  $I$  is the moment of inertia (see §VII E). Eq. (71) is a slowly varying function of  $R$ , and the upper limit is shown by the nearly straight lines in the range 1.8-2.0  $M_{\odot}$  in Fig. 6 for  $\nu_{ISCO} = 1300$  Hz and neutron star spin frequencies  $f = 200$  and 400 Hz. The closer the observed QPO frequency is to that of the ISCO, the closer the neutron star mass must be to this upper limit.

In addition, the neutron star radius must be smaller than the ISCO, which implies [117]

$$R \leq \left( \frac{1950 \text{ Hz}}{\nu_{ISCO}} \right) \left( 1 + 0.20 \frac{cJ}{GM^2} \right) \text{ km}. \quad (72)$$

Radii limits for masses less than the upper limit Eq. (72) scale with  $M^{1/3}$  and are also shown in Fig. 6, for the same  $\nu_{ISCO}$  and  $f$ 's as for the mass limit. These radii limits are somewhat more restrictive than that implied by the 716 Hz pulsar J1748-2446ad.

As upper limits to mass and radius, QPOs are not yet restrictive. However, if the measured frequencies are actually measurements of the ISCO, the implied masses are near 2  $M_{\odot}$ . Interestingly, in the case of 4U 1636-536, phase-resolved spectroscopy with the VLT suggest the neutron star is in the range of 1.6–1.  $M_{\odot}$  [120], providing support for this interpretation and for the existence of high-mass neutron stars.

### E. Moments of inertia

The discovery of the double-pulsar system PSR J0737-3039A & B [32, 121] provides physicists with the most relativistic system yet. Perhaps most intriguingly, it could provide a measurement of spin-orbit

coupling that could eventually lead to a determination of the moment of inertia  $I_A$  of star A [32]. Spin-orbit coupling advances the periastron of the orbit (apsidal motion) beyond the standard post-Newtonian advance as well as causing a precession of the orbital plane about the direction of the total angular momentum of the system [122] (geodetic precession). Since the masses of both stars are already accurately determined, and the moment of inertia can be expressed as a tight relation involving only  $M$  and  $R$  and no other EOS parameters, the measurement of  $I_A$  could have enormous importance.

To date, the best-determined moment of inertia is for the Crab pulsar [123]. This was based on an estimate [124] for the mass of the ionized portion of the Crab's remnant,  $4.6 \pm 1.8 M_\odot$ , which implies a lower limit to the Crab pulsar's moment of inertia of  $97 \pm 38 M_\odot \text{ km}^2$ . This limit would rule out only very soft EOSs.

According to Barker [125], the spin and orbital angular momenta evolve satisfying

$$\dot{\vec{S}}_i = \frac{G(M_i + 3M)}{2M_i a^3 c^2 (1 - e^2)^{3/2}} \vec{L} \times \vec{S}_i, \quad (73)$$

$$\vec{L}^{\dot{SO}} = \sum_i \frac{G(4M_i + 3M)}{2M_i a^3 c^2 (1 - e^2)^{3/2}} (\vec{S}_i - 3 \frac{\vec{L} \cdot \vec{S}_i}{|\vec{L}|^2} \vec{L}), \quad (74)$$

where the superscript  $SO$  refers to the spin-coupling contribution only (there are also first- and second-order post-Newtonian terms, 1PN and 2PN, respectively, unrelated to the spins, that contribute to this order). Here  $a$  is the semimajor axis of the effective one-body orbital problem (sum of the semi-major axes of the two stellar orbits),  $e$  is the eccentricity,  $M = M_A + M_B$ , and  $M_i$  refers to the mass of either binary component. To this order, one may employ the Newtonian relation for the orbital angular momentum:

$$|\vec{L}| = \frac{2\pi M_A M_B a^2 (1 - e^2)^{1/2}}{P} = M_A M_B \sqrt{\frac{Ga(1 - e^2)}{M}}, \quad (75)$$

where  $P$  is the orbital period and  $M = M_A + M_B$ . Then, from Eq. (73), the spin precession periods are

$$P_{p,i} = \frac{2c^2 a P M (1 - e^2)}{G(M - M_i)(M_i + 3M)}, \quad (76)$$

which are not identical for the two components unless they are of equal mass. Note that the spin precession periods are independent of the spins. Also note that if the spins are parallel to  $\vec{L}$ , there is, first, no spin precession, and second, the spin-orbit contribution to the advance of the periastron is in the opposite sense to the direction of motion.

The relevant observational parameters for PSR J0737-3039 extracted from Ref. [32] are:

$$\begin{aligned} M_A &\simeq 1.34 M_\odot, & M_B &\simeq 1.25 M_\odot, & a/c &= 2.93 \text{ s}, & e &\simeq 0.088, \\ P_A &\simeq 22.7 \text{ ms}, & P_B &\simeq 2.77 \text{ s}, & P &\simeq 0.102 \text{ day}. \end{aligned} \quad (77)$$

From these values, we observe that  $P_{pA} \simeq 74.9$  yrs and  $P_{pB} \simeq 70.6$  yrs. With these parameters, we can form the useful combinations

$$\frac{GM}{ac^2} = 4.32 \times 10^{-6}, \quad \frac{I_A}{Ma^2} = (7.74 \times 10^{-11}) I_{A,80}, \quad \text{and} \quad \frac{P}{P_A} = 3.88 \times 10^5, \quad (78)$$

where  $I_{A,80} = I_A / (80 M_\odot \text{ km}^2)$  is a typical value for the moment of inertia.

The spin precession leads to changes in the directions of the pulsar beams. In many cases, this will lead to the periodic appearance and disappearance of the pulsar beam from the Earth. Second, since the

total angular momentum is conserved (to this order), the orbital plane will change orientation, which will be observed as a change in the inclination angle  $i$ . Damour & Schaefer [122] have considered the question of how these effects affect the timing of binary pulsars. For the change in  $i$ ,

$$\frac{di}{dt} = \frac{G}{ac^2} \frac{\pi}{(1-e^2)^{3/2}} \sum_i \frac{I_i(4M_i + 3M_{-i})}{M_i a^2 P_i} \sin \theta_i \cos \phi_i, \quad (79)$$

where  $\theta_i$  is the angle between  $\vec{S}_i$  and  $\vec{L}$ , and  $\phi_i$  is the angle between the line of sight to pulsar  $i$  and the projection of  $\vec{S}_i$  on the orbital plane. The amplitude of the change in the orbital inclination angle  $i$  due to A's precession will be

$$\delta_i = \frac{|\vec{S}_A|}{|\vec{L}|} \sin \theta_A \simeq \frac{I_A M}{a^2 M_A M_B (1-e^2)^{1/2} P_A} \sin \theta_A. \quad (80)$$

This will cause a periodic departure from the expected time-of-arrival of pulses from pulsar A of amplitude

$$\delta t_A = \frac{M_B a}{M c} \delta_i \cos i = \frac{a}{c} \frac{I_A}{M_A a^2} \frac{P}{P_A} \sin \theta_A \cos i, \quad (81)$$

if one can assume that the orbital eccentricity is small. The facts that the orbit of PSR J0737-3039 is seen nearly edge-on and that  $\vec{S}_A$  is only slightly misaligned from  $\vec{L}$  makes this a special case in which the amplitude of the timing change produced by the orbital plane precession will be extremely small,  $\delta t_A \simeq (1.05 \pm 1.33) I_{A,80} \mu\text{s}$  [80]. Not only is the magnitude very small, but the large relative uncertainties in both  $\cos i$  ( $|\cos i| \simeq 0.028 \pm 0.028$ ) and in  $\sin \theta_A$  ( $\sin \theta_A \simeq 0.22 \pm 0.17$ ) combine to give a huge uncertainty in  $\delta t_A$ . We do not consider this effect further, but it could be relevant for future discoveries of binary pulsars with more favorable inclinations.

For the advance of the periastron, the ratio of the spin-orbit and 1PN contributions is [122]

$$\frac{A_p}{A_{1PN}} = -\frac{P}{6(1-e^2)^{1/2} M a^2} \sum_i \frac{I_i(4M_i + 3M_{-i})}{M_i P_i} (2 \cos \theta_i + \cot i \sin \theta_i \sin \phi_i). \quad (82)$$

In the case that  $|\vec{S}_A| \gg |\vec{S}_B|$ , only the  $i = A$  term contributes substantially. For comparison, the ratio of the 2PN to 1PN contributions is [122]

$$\begin{aligned} \frac{A_{2PN}}{A_{1PN}} &= \frac{GM}{4ac^2} \sum_i \left( \left[ 27 + 6 \frac{M_i}{M} + 6 \left( \frac{M_i}{M} \right)^2 \right] (1-e^2)^{-1} - 1 - \frac{46M_i}{3M} + \frac{10}{3} \left( \frac{M_i}{M} \right)^2 \right) \\ &\simeq \frac{GM}{12ac^2} \left( \frac{189}{1-e^2} - 47 \right), \end{aligned} \quad (83)$$

where both  $i = A$  and  $i = B$  terms contribute. The second line of Eq. (83) is valid in the case that  $M_A = M_B$ . Observational effects of the periastron advance are proportional to  $\cos i$  and so the effect is maximized in this system. Furthermore, Eq. (82) illustrates that uncertainties in the angle  $\phi_A$  are largely irrelevant in the case  $i \simeq 90^\circ$ . The 1PN periastron advance for PSR J0737-3039 is

$$A_{1PN} = \frac{6\pi}{1-e^2} \frac{GM}{ac^2} \text{ radians per orbit}, \quad (84)$$

or 0.294 radians per year. The periastron advance ratio works out to be [80]

$$A_{pA}/A_{1PN} \simeq 6.6_{-0.6}^{+0.2} 10^{-5} I_{A,80}. \quad (85)$$

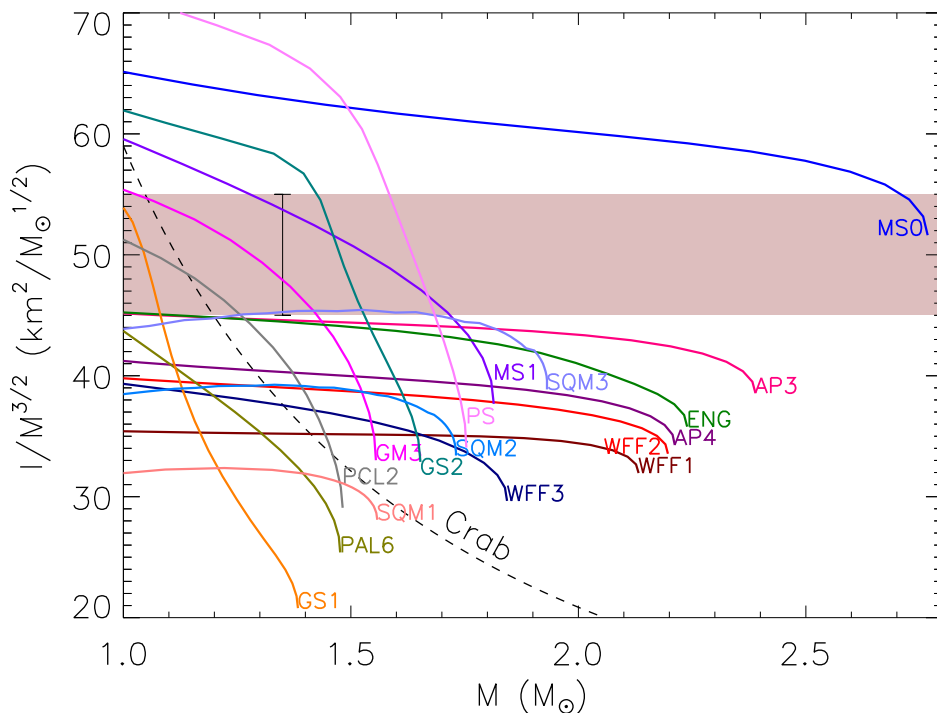


FIG. 9: The moment of inertia scaled by  $M^{3/2}$  as a function of stellar mass  $M$  for EOSs described in [6]. The shaded band illustrates a  $\pm 10\%$  error on a hypothetical  $I/M^{3/2}$  measurement with centroid  $50 \text{ km}^2 M_{\odot}^{-1/2}$ ; the error bar shows the specific case in which the mass is  $1.34 M_{\odot}$  with essentially no error. The dashed curve labelled "Crab" is the lower limit derived by [123] for the Crab pulsar.

However, a practical difficulty remains. The spin-orbit contribution depends upon the individual masses, not just the total mass which is known to extremely high precision, requiring for our purposes the determination of essentially three post-Newtonian parameters, as Damour [122] has emphasized, to an accuracy of a part in  $10^5$ . The accuracy of  $a_B \sin i$  at present is a few parts in  $10^3$ , and the determination of  $I_A$  depends on its refinement by a factor of 100 or more. There is reason to be optimistic that this can occur within a decade [80].

A sufficiently accurate measurement of  $I$  say, to within 10%, would usefully discriminate among families of EOSs because the mass will be known to great precision. This is displayed in Fig. 9, in which the quantity  $I/M^{3/2}$  (in order to reduce the vertical range) is plotted versus  $M$ . The shaded band illustrates a hypothetical measured value with error bars of  $\pm 10\%$ . Only curves that pass through the line with the error bar would be allowed. In this hypothetical case, the vast majority of the EOSs illustrated would not be adequate. For comparison, the lower limit derived for the Crab pulsar [123], which rules out only the softest EOSs, is also shown in Fig. 9. This limit is not nearly so restrictive.

The fit in Eq. (35) for EOSs previously cited as supporting masses greater than about  $1.6 M_{\odot}$  is reasonably tight. This relation may be inverted to yield a radius estimate given  $I$  and  $M$ . Furthermore, since  $I \propto R^2$ , the inferred relative error of  $R$  using this procedure would be approximately half the relative measured error of  $I$  itself.

## VIII. NEUTRINO EMISSION FROM A PROTO-NEUTRON STAR

A proto-neutron star (PNS) is born in the aftermath of a successful supernova explosion resulting from the gravitational collapse of the core of a massive star. During the first tens of seconds of evolution, nearly all ( $\sim 99\%$ ) of the remnant's binding energy is radiated away in neutrinos of all flavors [3, 126, 127, 128, 129, 130]. The neutrino luminosities and the emission timescale are controlled by several factors including the total mass of the PNS and the opacity of neutrinos at supranuclear density, which depend on the star's composition and the EOS of strongly interacting dense matter. One of the chief objectives in modeling PNSs is to infer their internal compositions through future supernova neutrino signals detected in neutrino observatories like SuperK, SNO and others, including UNO [131].

### A. The birth of proto-neutron stars

The evolution of a PNS proceeds through several distinct stages [3, 132] and with various outcomes [133, 134], as shown schematically in Fig. 10. Immediately following core bounce and the passage of a shock through the PNSs outer mantle, the star contains an unshocked, low entropy core of mass  $\simeq 0.7 M_\odot$  in which neutrinos are trapped (stage I in the figure). The core is surrounded by a low density, high entropy ( $5 < s < 10$ ) mantle that is both accreting matter from the outer iron core falling through the shock and also rapidly losing energy due to electron captures and thermal neutrino emission. The mantle extends up to the shock, which is temporarily stalled about 200 km from the center prior to an eventual explosion.

After a few seconds (stage II), accretion becomes less important if the supernova is successful and the shock has ejected the stellar envelope. Extensive neutrino losses and deleptonization will have led to a loss of lepton pressure and the collapse of the mantle. If enough accretion has occurred, however, the star's mass could increase beyond the maximum mass capable of being supported by the hot, lepton-rich matter. If this occurs, the remnant collapses to form a black hole and its neutrino emission is believed to quickly cease [135].

Neutrino diffusion deleptonizes the core on time scales of 10–15 s (stage III). Diffusion time scales are proportional to  $R^2(c\lambda_\nu)^{-1}$ , where  $R$  is the star's radius and  $\lambda_\nu$  is the effective neutrino mean free path. This generic relation illustrates how both the EOS and the composition influence evolutionary time scales. The diffusion of high-energy (200–300 MeV)  $\nu$ 's from the core to the surface where they escape as low-energy (10–20 MeV)  $\nu$ 's generates heat (a process akin to joule heating) through neutrino-matter interactions. The core's entropy approximately doubles, producing temperatures in the range of 30–60 MeV during this time, even as neutrinos continue to be prodigiously emitted from the star's effective surface, or neutrinosphere.

Strange matter, in the form of hyperons, a Bose condensate, or quark matter, suppressed when neutrinos are trapped, could appear at the end of the deleptonization. Its appearance would lead to a decrease in the maximum mass that the internal pressure of matter is capable of supporting against gravity, implying metastability of the neutron star and another chance for black hole formation [133, 134]. This would occur if the PNSs mass, which must be less than the maximum mass of hot, lepton-rich matter (or else a black hole would already have formed), is greater than the maximum mass of hot, lepton-poor matter. However, if strangeness does not appear, the maximum mass instead increases during deleptonization and the appearance of a black hole would be unlikely unless accretion in this stage remains significant.

The PNS is now lepton-poor, but it is still hot. While the star has vanishing net neutrino number, thermally produced neutrino pairs of all flavors dominate the emission. The average neutrino energy slowly decreases, and the neutrino mean free path increases. After approximately 50 seconds (stage IV),  $\lambda \simeq R$ , and the star finally becomes transparent to neutrinos. The neutrino luminosity rapidly decreases beyond this time. Since the threshold density for the appearance of strange matter decreases with decreasing

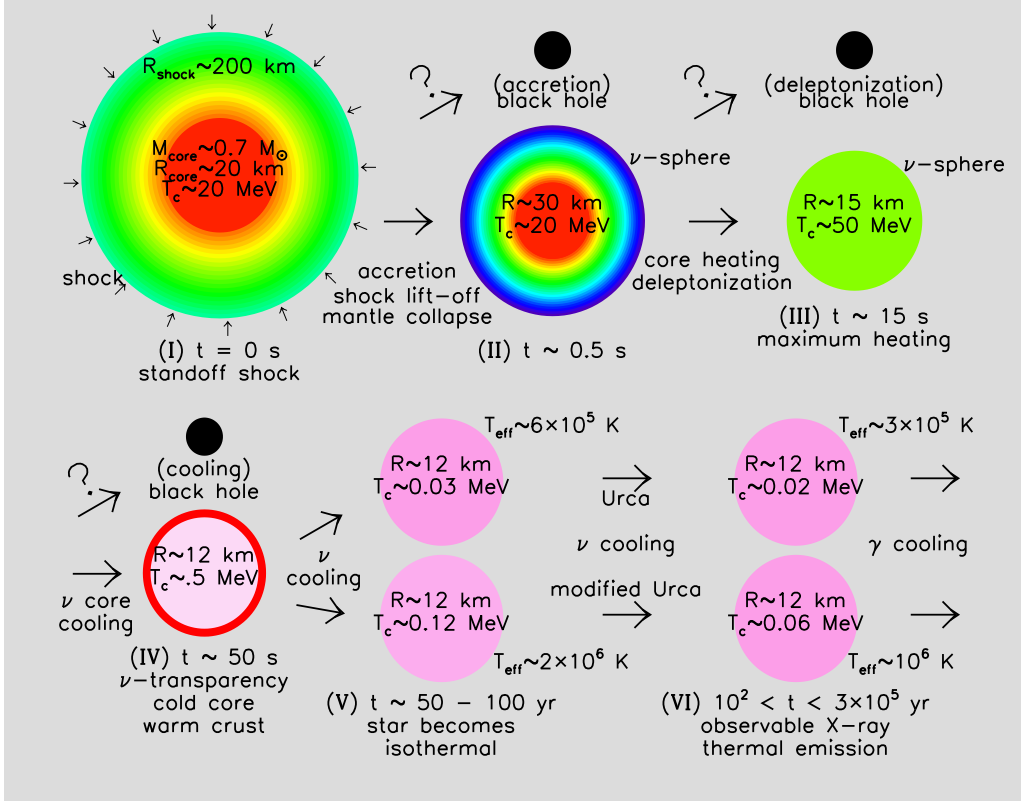


FIG. 10: The main stages of evolution of a neutron star, from Ref.[133]. Shading indicates approximate relative temperatures.

temperature, a delayed collapse to a black hole is still possible during this epoch.

Following the onset of neutrino transparency, the core continues to cool by neutrino emission, but the star's crust remains warm and cools less quickly. The crust serves as an insulating blanket which prevents the star from coming to complete thermal equilibrium and keeps the surface relatively warm ( $T \approx 3 \times 10^6$  K) for up to 100 years (stage V). The temperature of the surface after the interior of the star becomes isothermal (stage VI) is determined by the rate of neutrino emission in the star's core and the composition of the surface.

## B. Theoretical expectations

To understand what aspects of the EOS and structure can be probed by neutrinos, we examine some analytic models for proto-neutron star evolution [133, 136]. For clarity and simplicity, we employ Newtonian gravitation, as this does not affect the qualitative conclusions we will draw. We will assume that the neutrino distribution function is well-approximated by a Fermi-Dirac distribution, so the neutrino number density is  $n_\nu = \int_0^\infty n_\nu(E_\nu) dE_\nu$ , where

$$n_\nu(E_\nu) = \frac{E_\nu^2}{2\pi^3(\hbar c)^3} f_\nu(E_\nu), \quad \text{and } f_\nu(E_\nu) = [1 + e^{(E_\nu - \mu_\nu)/T}]^{-1}. \quad (86)$$

We also make the diffusion approximation, in which both number and energy fluxes are driven by density gradients:

$$\begin{aligned} F_\nu &= -\frac{c}{3} \int_0^\infty \left[ \lambda_\nu \frac{\partial n_\nu(E_\nu)}{\partial r} - \lambda_{\bar{\nu}} \frac{\partial n_{\bar{\nu}}(E_\nu)}{\partial r} \right] dE_\nu, \\ L_\nu &= -4\pi r^2 \int_0^\infty \sum_i \frac{c\lambda_E^i}{3} \frac{\partial \epsilon_i(E_\nu)}{\partial r} dE_\nu, \end{aligned} \quad (87)$$

where  $F_\nu$  and  $L_\nu$  are the net electron neutrino number flux and total neutrino luminosity, respectively,  $\lambda_\nu$  ( $\lambda_{\bar{\nu}}$ ) and  $\lambda_E^i$  are the mean free paths for number and energy transport, respectively, and  $\epsilon_i$  is the neutrino energy density.  $i = [\nu_e, \bar{\nu}_e, \nu_\mu, \bar{\nu}_\mu, \nu_\tau, \bar{\nu}_\tau]$  refers to the neutrino species. The net changes in electron lepton number  $Y_L = Y_e + Y_\nu - Y_{\bar{\nu}}$  and the total entropy per baryon are

$$\begin{aligned} n \frac{\partial Y_L}{\partial t} &= -\frac{1}{r^2} \frac{\partial}{\partial r} (r^2 F_\nu), \\ nT \frac{\partial s}{\partial t} &= -\frac{1}{4\pi r^2} \frac{\partial L_\nu}{\partial r} - n \sum_j \mu_j \frac{dY_j}{dt}, \end{aligned} \quad (88)$$

where  $j = n, p, e, \nu_e$ .

The net neutrino mean free paths  $\lambda_\nu$  and  $\lambda_E^i$  are due to both absorption and scattering and should also include inverse processes. In what follows, we will want to have an approximation for  $\lambda_\nu$  under degenerate conditions and when electron neutrino absorption dominates. Similarly, we will want to have an approximation for  $\lambda_E^i$  under non-degenerate conditions and when it is dominated by scattering. In that case, the transport is dominated by all neutrino types other than  $\nu_e$ , and one can replace the sum in Eq. (88) by a single term involving the scattering mean free path. Ref. [136] shows that suitable approximations are then

$$\begin{aligned} \lambda_\nu &\simeq \lambda_0 \left( \frac{T_0}{T} \right) \left[ 1 + \left( \frac{E_\nu - \mu_\nu}{\pi T} \right) \right]^{-1}, \\ \lambda_E^i &\simeq \lambda_C \left( \frac{T_0^3}{TE_\nu^2} \right) \left( \frac{n_s}{n} \right)^{1/3}, \end{aligned} \quad (89)$$

where  $\lambda_0 \simeq 50$  cm,  $\lambda_C \simeq .2$  km and  $T_0 \simeq 10$  MeV. Finally we note a property of the Fermi distribution function under degenerate conditions:

$$\frac{\partial f_\nu}{\partial r} \simeq \frac{f_\nu(1-f_\nu)}{T} \frac{\partial \mu_\nu}{\partial r} \simeq \delta(E_\nu - \mu_\nu) \frac{\partial \mu_\nu}{\partial r}. \quad (90)$$

It is convenient to examine two distinct periods of proto-neutron star evolution: the deleptonization era and the cooling era. During the first of these, the transport within the star is dominated by degenerate electron neutrinos propagating through degenerate matter. Only near the surface do these conditions break down. We can use the first of Eqs. (88) to examine the loss of leptons from the star. Using Eq. (89) for  $\lambda_\nu$ , Eq. (87) for  $F_\nu$ , and Eq. (90), one has

$$\frac{\partial n Y_L}{\partial t} = \frac{c\lambda_0}{18\pi^2(\hbar c)^3} \frac{1}{r^2} \frac{\partial}{\partial r} \left[ r^2 \left( \frac{T_0}{T} \right)^2 \frac{\partial \mu_\nu^3}{\partial r} \right]. \quad (91)$$

Using  $\partial Y_L / \partial Y_\nu \simeq (\partial Y_L / \partial Y_\nu)_0 \simeq 5$  and  $6\pi^2 n Y_\nu (\hbar c)^3 = \mu_\nu^3$  for degenerate neutrinos, ignoring spatial variations of  $T$  since the core is nearly isothermal, and separating the spatial and temporal variations using  $\mu_\nu^3 = \mu_{\nu,0}^3 \psi(x) \phi(t)$ , this can be rewritten as

$$\frac{\tau_D}{\phi} \frac{d\phi}{dt} = \frac{1}{x^2 \psi} \frac{\partial}{\partial x} \left[ x^2 \frac{\partial \psi}{\partial x} \right] = -1, \quad (92)$$

where

$$x = r \frac{x_1}{R}, \quad \tau_D = \frac{3}{c\lambda_0} \left( \frac{R}{x_1} \right)^2 \left( \frac{T_c}{T_0} \right)^2 \left( \frac{\partial Y_L}{\partial Y_\nu} \right)_0. \quad (93)$$

$T_c$  is the assumed uniform temperature. The quantity  $x_1$  is the value of  $x$  for which  $\psi$  first vanishes. The second equality of Eq. (92) is the Lane-Emden equation of index 1 for which the solution is  $\psi(x) = \sin(x)/x$  and has the outer boundary  $x_1 = \pi$ . The first equality of Eq. (91) is an exponential decay  $\phi(t) = \exp(-t/\tau_D)$  and  $\tau_D$  is clearly the diffusion timescale. It is interesting that  $\tau_D$  is independent of  $\mu_{\nu,0}$  but does depend sensitively on the ambient temperature  $T_c$ . Since one expects  $T_c \propto n_{center}^{2/3}$  at fixed entropy,  $\tau_D$  will scale with the mass of the remnant like  $M^{4/3}$  since  $R$  changes very slowly with  $M$ .

From Eq.(87), one can determine the neutrino flux

$$F_\nu(x, t) = -\frac{c\lambda_0}{18\pi^2} \left( \frac{\mu_{\nu,0}}{\hbar c} \right)^3 \left( \frac{T_0}{T_c} \right)^2 \frac{x_1}{R} \frac{\partial \psi(x)}{\partial x} \phi(t). \quad (94)$$

At the outer boundary, where  $x\partial\psi/\partial x = -1$ , the emerging flux is then

$$F_\nu(R, t) = \frac{c\lambda_0}{18\pi^2 R} \left( \frac{\mu_{\nu,0}}{\hbar c} \right)^3 \left( \frac{T_0}{T_c} \right)^2 \phi(t) \simeq \frac{cF_2(0)}{8\pi^2} \left( \frac{T_e(t)}{\hbar c} \right)^3, \quad (95)$$

where  $T_e(t)$  is thereby defined as the effective blackbody temperature, and  $F_i$  is the standard Fermi integral of index  $i$ . We assume that the effective value of the chemical potential when the neutrinos decouple from the matter is  $\mu_{\nu,e} \leq T$ . The effective temperature is therefore

$$T_e(t) \simeq \left( \frac{4\lambda_0}{9RF_2(0)} \right)^{1/3} \left( \frac{T_0}{T_c} \right)^{2/3} \mu_{\nu,0} \phi(t)^{1/3}. \quad (96)$$

The average emergent neutrino energy is then

$$\langle E_\nu \rangle \simeq T_e(t)(F_3(0)/F_2(0)) \simeq 3.15T_e(t), \quad (97)$$

and the star's emergent luminosity will be  $4\pi R^2 F_\nu \langle E_\nu \rangle$ . The effective value of the chemical potential at decoupling can be estimated using the Eddington approximation, which gives

$$\psi_e = -\frac{4\lambda_e}{3R} \quad (98)$$

where  $\lambda_e$  is the neutrino mean free path at the decoupling point. From this, one can show that  $\mu_e \lesssim T_e$  so we are justified in using zero arguments in the above Fermi integrals.

During the beginning of the proto-neutron star phase,  $R \simeq 20$  km and  $T_c \sim 20$  MeV. One thus obtains  $\tau_D = 16$  s,  $F_\nu(R, 0) = 2.5 \times 10^{42}$  neutrinos  $\text{cm}^{-2} \text{s}^{-1}$ ,  $T_e \simeq 2.9$  MeV and  $\langle E_\nu \rangle \simeq 9.2$  MeV. The initial electron neutrino luminosity due to deleptonization is  $L_\nu(R, 0) = 2.1$  bethe  $\text{s}^{-1}$ . We remark that the initial luminosity burst predicted by detailed models is much larger, around 100 bethe  $\text{s}^{-1}$ , but these are neutrinos originating from the outer mantle of the proto-neutron star near the neutrinosphere. Within a few seconds, as the mantle deleptonizes and collapses, the emergent luminosity becomes dominated by core emission.

Energy transport is also important during the deleptonization stage. Noting that

$$\sum_j \mu_j dY_j = (-\mu_n + \mu_p + \mu_e - \mu_\nu) dY_e + \mu_\nu dY_L, \quad (99)$$

the first term on the right-hand side vanishes in beta equilibrium. For electron neutrinos, which dominate in the interior, the mean free paths are so small that the first term on the right-hand side of Eq. (88) is negligible during deleptonization compared to the second term. We therefore have

$$\frac{s}{a} \frac{ds}{dt} \simeq -\mu_\nu \frac{\partial Y_L}{\partial t} \simeq - \left( \frac{\partial Y_L}{\partial Y_\nu} \right)_0 \left( \frac{Y_\nu}{Y_{\nu,0}} \right)^{1/3} \mu_{\nu,0} \frac{\partial Y_\nu}{\partial t} \quad (100)$$

This shows that continuous replenishment of diffusing neutrinos enhances the growth of entropy in the star. For degenerate matter,  $s \simeq aT$  where  $a \sim 0.05 \text{ MeV}^{-1}$  is the supra-nuclear specific heat. Integration leads to

$$s_f^2 - s_i^2 \simeq \frac{3a}{2} \left( \frac{\partial Y_L}{\partial Y_\nu} \right)_0 \mu_{\nu,0} Y_{\nu,0} \simeq 5, \quad (101)$$

where  $s_f$  and  $s_i$  are the final and initial entropies. For  $s_i \sim 1$  one obtains  $s_f \sim 2.5$ . The final entropy scales roughly as  $M^{1/6}$ . Thus it is clear that the central portions of the star heat significantly during deleptonization.

Following deleptonization, when the central temperature reaches a maximum, core cooling begins. By this time,  $\mu_\nu \leq T$  and its gradient is also small. The second term in the second of Eq. (88) becomes negligible. Assuming that the energy transport mean free paths of all flavors of neutrinos are roughly equal, we can replace the sum in the second of Eq. (87) by a factor 6, and the neutrino luminosity becomes

$$L_\nu = -4\pi r^2 \frac{c\lambda_C}{6} \left( \frac{T_0}{\hbar c} \right)^3 \frac{\partial T}{\partial r}. \quad (102)$$

where we used the fact that  $\int_0^\infty E f dE = \pi^2 T^2/12$ . During the cooling phase, the density gradients in the star's center are small, and one can remove the density dependence from the integral in the energy transport equation, which becomes

$$T \frac{\partial s}{\partial T} \frac{dT}{dt} = \frac{c\lambda_C}{6n_s} \left( \frac{n_s}{n_*} \right)^{4/3} \left( \frac{T_0}{\hbar c} \right)^3 \frac{1}{r^2} \frac{\partial}{\partial r} \left[ r^2 \frac{\partial T}{\partial r} \right]. \quad (103)$$

We let  $n_*$  be the density in the star's center. The matter specific heat is dominated by baryons, so that

$$s \simeq a \left( \frac{n_s}{n_*} \right)^{2/3} T, \quad (104)$$

where  $a \simeq 0.1$  is the level density of nucleons at  $n_s$ . Once again, we can seek a separable solution with  $T = T_* \psi(x) \phi(t)$ :

$$\tau_C \frac{\partial \phi}{\partial t} = \frac{1}{\psi^2 x^2} \frac{\partial}{\partial x} \left[ x^2 \frac{\partial \psi}{\partial x} \right] = -1, \quad (105)$$

with

$$\tau_C = \frac{6an_s T_* R^2}{c\lambda_C x_1^2} \left( \frac{\hbar c}{T_0} \right)^3 \left( \frac{n_*}{n_s} \right)^{2/3}, \quad (106)$$

where  $x_1^2 \simeq 19$  is the eigenvalue for the index 2 Lane-Emden equation. The temporal solution is trivial,  $\phi = 1 - t/\tau_C$ .  $T_*$  is the core temperature at the end of deleptonization and the beginning of cooling ( $t = 0$  in the immediate above).

We can establish the emergent luminosity and define an effective temperature with

$$L_\nu(R, t) = -4\pi R T_* \frac{c\lambda_C}{6} \left( \frac{T_0}{\hbar c} \right)^3 \left( x \frac{\partial \psi}{\partial x} \right)_{x_1} \phi(t) = \frac{cF_3(0)}{2(\hbar c)^3} R T_e(t)^4. \quad (107)$$

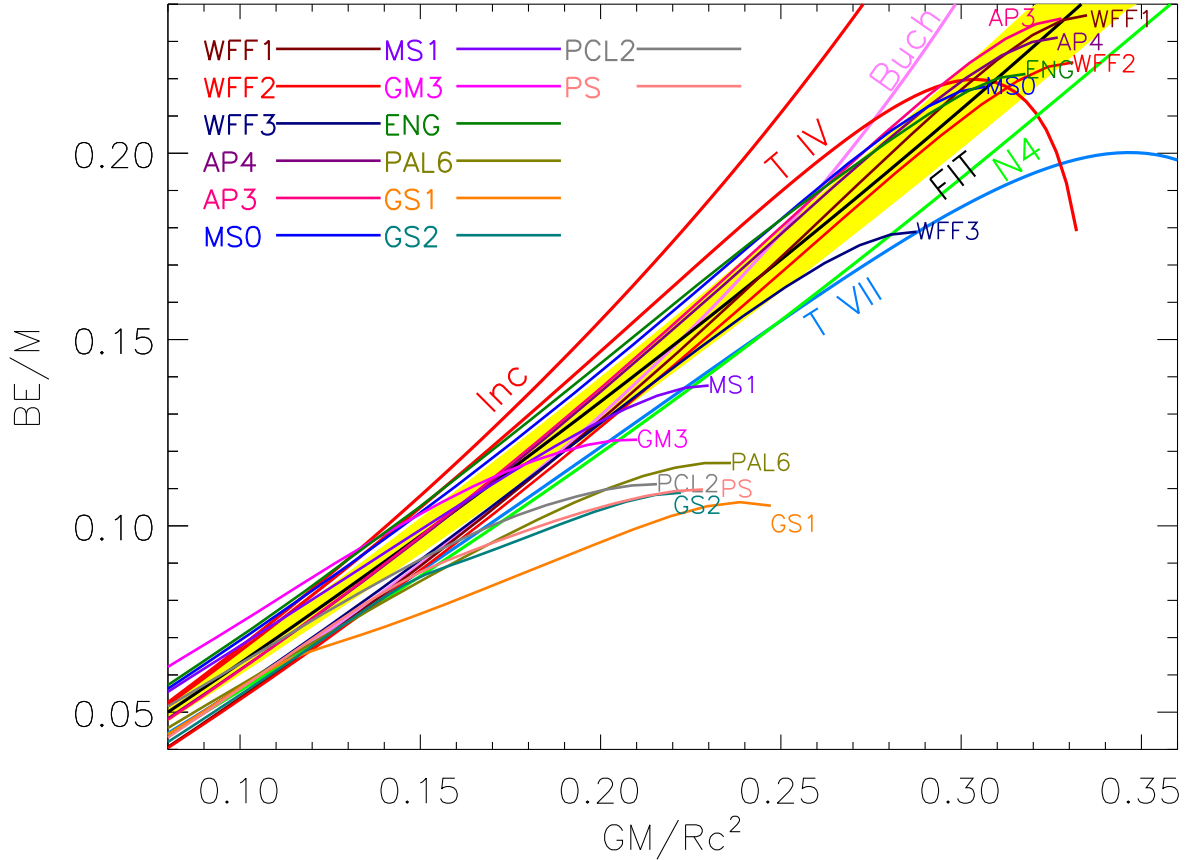


FIG. 11: The binding energy per unit mass of various EOSs as a function of  $M/R$ . The lighter curves are EOSs for nucleonic stars as well as those containing hyperons, Bose condensates and deconfined quark matter (see Ref. [6] for details). The five heavier curves are for analytic solutions of GR structure equations. The shaded band is the fit with error extents as given in Eq. (108). Figure taken from Ref. [6].

For the index 2 Lane-Emden equation,  $-(x\partial\psi/\partial x)_{x_1} \simeq 0.56$ . Inserting values for  $T_* = 50$  MeV and  $n_* = 4n_s$ , we find  $\tau_C \simeq 18$  s,  $L_\nu(R, 0) \simeq 11$  bethe  $s^{-1}$ ,  $T_e(0) \simeq 5.5$  MeV, and  $\langle E_\nu \rangle \simeq 17$  MeV. Note that  $T_e$  at the beginning of the cooling era is nearly twice as large as at the beginning of deleptonization. This is attributable to core heating which occurs during deleptonization and results in a steady increase in the average energy of emitted neutrinos during the deleptonization era. Finally, note that like  $\tau_D$ ,  $\tau_C \propto M^{4/3}$ . Also  $T_e \propto T_*^{1/4} \propto M^{1/6}$ .

In summary, there are a multitude of observables that can provide details of the proto-neutron star: timescales, average energies, and neutrino light curves. Of course, the unknown details of the proto-neutron star such as its mass, EOS and opacities are not related to these variables in unambiguous ways. However, one observable that does not depend upon opacities can be considered: the total neutrino emission which equals the binding energy released in the gravitational collapse to form the neutron star. In Newtonian gravity, the binding energy of a uniform sphere is  $BE = 3GM^2/(5R)$ . Ref. [6] determined an approximate fit to the binding energies for EOSs that is valid for EOSs which permit maximum masses larger than about  $1.65 M_\odot$ :

$$BE/M \simeq (0.60 \pm 0.05)\beta(1 - \beta/2)^{-1}, \quad (108)$$

where  $\beta = GM/Rc^2$ . The binding energies of neutron stars formed from a variety of EOSs is shown, together with the above fit, in Fig. 11. Additionally are shown binding energies for five analytic solutions of GR applicable to neutron or self-bound stars [6]. With the detection of thousands or millions of neutrinos, the binding energy could be determined to better than a percent, and the tightness of this fit would imply a correspondingly tight relation between  $M$  and  $R$  to be established.

### C. Model calculations

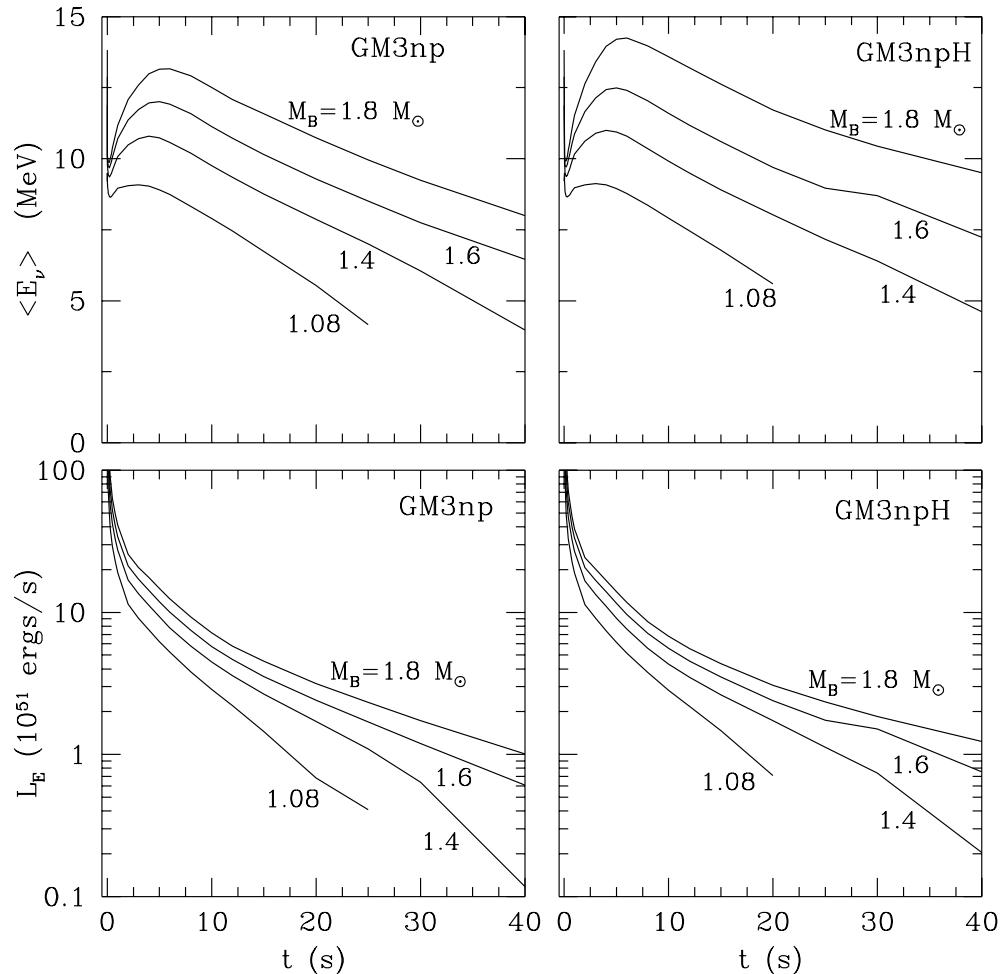


FIG. 12: The evolution of the average energy and total luminosity of neutrinos in PNSs composed of baryons only (left panel) and baryons and hyperons (right panel). The figure is from Ref. [128].

Neutrino signals from PNSs depend on many stellar properties, including the mass; initial entropy, lepton fraction and density profiles; and neutrino opacities. In Figs. 12 – 14, the dependence of neutrino emission on PNS characteristics are shown from the detailed study of Pons et al. [128, 129, 130]. The generic results (see Fig. 12) are that both  $L_\nu$  and  $\langle E_\nu \rangle$  increase with increasing mass [3, 128].  $\langle E_\nu \rangle$  for all flavors increases during the first 2-5 seconds of evolution, and then decreases nearly linearly with time. For times larger than about 10 seconds, and prior to the occurrence of neutrino transparency, the  $L_\nu$  decays exponentially with a time constant that is sensitive to the high-density properties of matter.

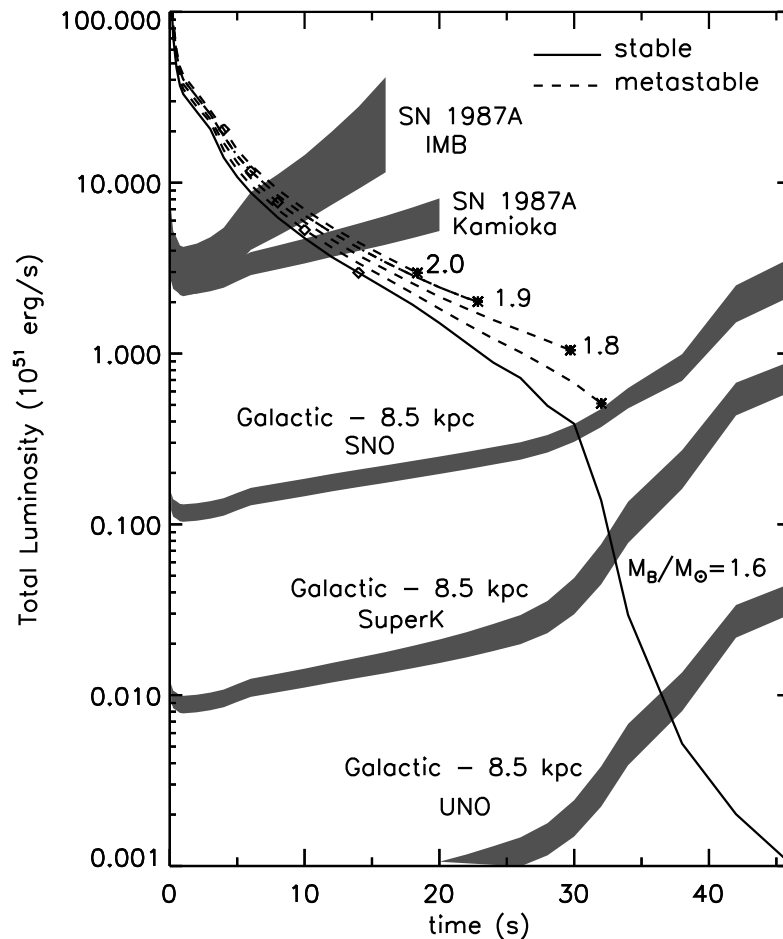


FIG. 13: The evolution of the total neutrino luminosity for  $npQ$  PNSs. Shaded bands illustrate the limiting luminosities corresponding to a count rate of 0.2 Hz, assuming a supernova distance of 50 kpc for IMB and Kamioka, and 8.5 kpc for SNO and SuperK. The widths of the shaded regions represent uncertainties in the average neutrino energy from the use of a diffusion scheme for neutrino transport. Figure taken from Ref. [130].

Significant variations in neutrino emission occur beyond 10 seconds:  $L_\nu$  is larger during this time for stars with smaller radii and with the inclusion of hyperons in the matter. Finally, significant regions of the stars become convectively unstable during the evolution, as several works have found [137].

The main effect of the larger mean free paths produced by in-medium corrections [127, 138] is that the inner core deleptonizes more quickly. In turn, the maxima in central temperature and entropy are reached on shorter timescales. In addition, the faster increase in thermal pressure in the core slows the compression associated with the deleptonization stage, although after 10 s the net compressions of all models converge. The relatively large, early, changes in the central thermodynamic variables do not, however, translate into similarly large effects on observables such as  $L_\nu$  and  $\langle E_\nu \rangle$ , relative to the baseline simulation. It is especially important that at and below nuclear density, the corrections due to correlations are relatively small. Since information from the inner core is transmitted only by the neutrinos, the time scale to propagate any high density effect to the neutrinosphere is the neutrino diffusion time scale. Since the neutrinosphere is at a density approximately  $0.01n_s$ , and large correlation corrections occur only above

$n_s/3$  where nuclei disappear, correlation corrections have an effect at the neutrinosphere only after 1.5 s. However, the corrections are still very important during the longer-term cooling stage, and result in a more rapid onset of neutrino transparency compared to the Hartree results [127, 138].

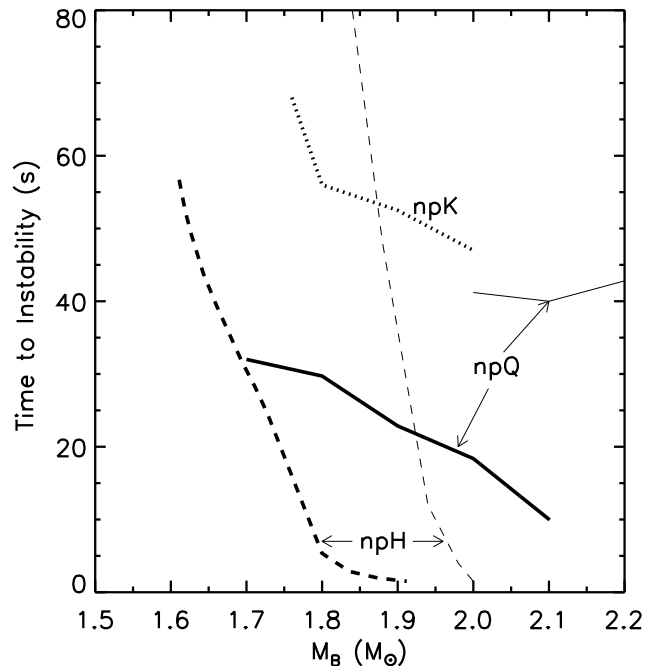


FIG. 14: Lifetimes of metastable stars versus the PNS baryon mass  $M_B$ . Thick lines denote cases in which the maximum gravitational masses of cold, catalyzed stars are near  $1.45 M_\odot$ , which minimizes the metastability lifetimes. The thin lines for the  $npQ$  and  $npH$  cases are for EOSs with larger maximum gravitational masses ( $1.85$  and  $1.55 M_\odot$ , respectively.) Figure taken from Ref. [130].

A comparison of the signals observable with different detectors is shown in Fig. 13, which displays  $L_\nu$  as a function of baryon mass  $M_B$  for stars containing quarks in their cores. In the absence of accretion,  $M_B$  remains constant during the evolution, while the gravitational mass  $M_G$  decreases. The two upper shaded bands correspond to estimated SN 1987A (50 kpc distance) detection limits with KII and IMB, and the lower bands correspond to estimated detection limits in SNO, SuperK, and UNO, for a Galactic supernova (8.5 kpc distance). The detection limits have been set to a count rate  $dN/dt = 0.2$  Hz [129]. It is possible that this limit is too conservative and could be lowered with identifiable backgrounds and knowledge of the direction of the signal. The width of the bands represents the uncertainty in  $\langle E_{\bar{\nu}_e} \rangle$  due to the diffusion approximation [128, 129, 130]. It appears possible to distinguish between stable and metastable stars, since the luminosities when metastability is reached are always above conservative detection limits.

#### D. Metastable proto-neutron stars

Proto-neutron stars in which strangeness appears following deleptonization can be metastable if their masses are large enough [139, 140]. This stems from the interesting behavior that the expression of strangeness is suppressed in hot, lepton-rich stars because of the large value of  $\mu_e$ . However, as stars

deleptonize,  $\mu_e$  falls and it is possible that strangeness eventually appears in the star's core. Generally, this softens the equation of state, causing a decrease in the effective maximum mass. This leads to a possibly important diagnostic that could shed light on the internal composition of neutron stars: the abrupt cessation of the neutrino signal when a deleptonizing strangeness-containing star suddenly finds that its mass exceeds the maximum mass. This would be in contrast to a normal star of similar mass for which the signal continues to fall until it is obscured by the background. In Fig. 14 the lifetimes for stars containing hyperons ( $npH$ ), kaons ( $npK$ ) and quarks ( $npQ$ ) are compared [129]. In all cases, the larger the mass, the shorter the lifetime. For the kaon and quark PNSs, however, the collapse is delayed until the final stage of the Kelvin-Helmholtz epoch, while this is not necessarily the case for hyperon-rich stars. In addition, there is a much stronger mass dependence of the lifetimes for the hyperon case.

Clearly, the observation of a single case of metastability, and the determination of the metastability time alone, will not necessarily permit one to distinguish among the various possibilities. Only if the metastability time is less than 10–15 s, could one decide on this basis that the star's composition was that of  $npH$  matter. However, as in the case of SN 1987A, independent estimates of  $M_B$  might be available [141]. In addition, the observation of two or more metastable neutron stars might permit one to differentiate among these models. This highlights the need for breakthroughs in lattice simulations of QCD at finite baryon density in order to unambiguously determine the EOS of high density matter. In the meantime, intriguing possible extensions of supernova and PNS simulations with  $npQ$  and  $npK$  matter include the consideration of heterogeneous structures and quark matter superfluidity [142].

## IX. MAGNETIC MATTERS

Recent investigations of the effects of ultra-strong magnetic fields ( $B > 10^{14}$  Gauss) on neutron stars are spurred by several independent arguments that link the class of soft  $\gamma$ -ray repeaters and perhaps certain anomalous X-ray pulsars with neutron stars having ultra strong magnetic fields – the so-called magnetars [143, 144, 145, 146]. In addition, some soft  $\gamma$ -ray repeaters directly imply, from their periods and spin-down rates, surface fields in the range  $2 - 8 \times 10^{14}$  Gauss. (See Table I from Cardall et. al. [147] for a summary of observations.) Kouveliotou et al. [148] argue from the population statistics of soft  $\gamma$ -ray repeaters that magnetars constitute about 10% of the neutron star population. While some observed white dwarfs have large enough fields to give ultra-strong neutron star magnetic fields through flux conservaton, it does not appear likely that such isolated examples could account for a significant fraction of ultra-strong field neutron stars. Therefore, an alternative mechanism seems necessary for the creation ultra-strong magnetic fields in neutron stars. Duncan & Thompson [149, 150] suggested that large fields (up to  $3 \times 10^{17} \times (1 \text{ ms}/P_i)$  Gauss, where  $P_i$  is the initial rotation period) can be generated in nascent neutron stars through the smoothing of differential rotation and convection.

The effects of magnetic fields on the EOS at low densities, relevant for neutron star crusts, has been extensively studied (see for example, Refs. [151, 152, 153, 154]). Only a handful of works have considered the effects of very large magnetic fields on the EOS of dense neutron star matter [155, 156, 157]. Lai and Shapiro [151] considered non-interacting, charge neutral, beta-equilibrated matter at subsaturation densities, whereas Chakrabarty and co-authors [155, 156] studied dense matter including interactions using a field-theoretical description. These authors found large compositional changes in matter induced by ultra-strong magnetic fields due to the quantization of orbital motion. Acting in concert with the nuclear symmetry energy, Landau quantization substantially increases the concentration of protons compared to the field-free case, which in turn leads to a softening of the EOS. This lowers the maximum mass relative to the field-free value. In these works, however, the electromagnetic field energy density and pressure, which tend to stiffen the EOS, were not included. In addition, changes in the general relativistic structure induced by the magnetic fields (studied in detail by Bocquet et al. [158] who, however, omitted the

compositional changes in the EOS due to Landau quantization) were also ignored. Calculations including the combined effects of the magnetic fields on the EOS and on the general relativistic structure have been reported by Cardall, Prakash & Lattimer [147].

The most intriguing questions are:

1. What is the largest frozen-in magnetic field a stationary neutron star can sustain?, and,
2. What is the effect of such ultra-strong magnetic fields on the maximum neutron star mass?

### A. Magnetic effects on the EOS

The answers to both of these questions hinge upon the effects strong magnetic fields have both on the EOS of neutron-star matter and on the structure of neutron stars. The magnitude of the magnetic field strength  $B$  needed to dramatically affect neutron star structure directly can be estimated with a dimensional analysis [151] equating the magnetic field energy  $E_b \sim (4\pi R^3/3)(B^2/8\pi)$  with the gravitational binding energy  $E_{B.E.} \sim 3GM^2/5R$ , yielding the so-called virial limit

$$B \sim 1.4 \times 10^{18} \left( \frac{M}{1.4M_\odot} \right) \left( \frac{R}{10 \text{ km}} \right)^{-2} \text{ Gauss}, \quad (109)$$

where  $M$  and  $R$  are, respectively, the neutron star mass and radius.

The magnitude of  $B$  required to directly influence the EOS can be estimated by considering its effects on charged particles. Charge neutral, beta-equilibrated, nucleonic matter contains both negatively charged leptons (electrons and muons) and positively charged protons. Magnetic fields quantize the orbital motion (Landau quantization) of these charged particles. Relativistic effects become important when the particle's cyclotron energy  $e\hbar B/(mc)$  is comparable to its rest mass energy. The magnitudes of the so-called critical fields (although there is nothing critical about this) are

$$\begin{aligned} B_c^e &= (\hbar c/e) \lambda_e^{-2} = 4.414 \times 10^{13} \text{ Gauss}, \\ B_c^\mu &= (m_\mu/m_e)^2 B_c^e = 1.755 \times 10^{18} \text{ Gauss}, \\ B_c^p &= (m_p/m_e)^2 B_c^e = 1.487 \times 10^{20} \text{ Gauss}, \end{aligned} \quad (110)$$

for the electron, muon and proton, respectively ( $\lambda_e = \hbar/m_e c \simeq 386 \text{ fm}$  is the Compton wavelength of the electron). When the Fermi energy of the proton becomes significantly affected by the magnetic field, the composition of matter in beta equilibrium is significantly affected. In turn, the pressure of matter is significantly affected. In neutron star matter this situation occurs when  $B^* \equiv B/B_c^e \sim 10^5$ , and will lead to a general softening of the EOS as shown by Broderick, Prakash & Lattimer [159].

In neutron stars, magnetic fields may well vary in strength from the core to the surface. The scale lengths of such variations are, however, usually much larger than the microscopic magnetic scale  $l_m$ , which depends on the magnitude of  $B$ . For low fields, for which the quasi-classical approximation holds,

$$l_m \simeq (\lambda_e^2 / B^*) (3\pi^2 n_e)^{1/3} \approx 10^5 (n_e/n_s)^{1/3} / B^* \text{ fm}, \quad (111)$$

where  $n_e$  is the number density of electrons and  $n_s$  is the normal nuclear saturation density (about  $0.16 \text{ fm}^{-3}$ ). For high fields, when only a few Landau levels are occupied,

$$l_m \simeq 2\pi^2 n_e (\lambda_e^2 / B^*)^2 \approx 7 \times 10^9 (n_e/n_s) / B^{*2} \text{ fm}. \quad (112)$$

In either case, the requirement that  $R \gg l_m$  is amply satisfied; hence, the magnetic field  $B$  may be assumed to be locally constant and uniform as far as effects on the EOS are concerned.

In non-magnetic neutron stars, the pressure of matter ranges from  $2 - 5 \text{ MeV fm}^{-3}$  at nuclear density to  $200 - 600 \text{ MeV fm}^{-3}$  at the central density of the maximum mass configuration, depending on the EOS [133]. These values may be contrasted with the energy density and pressure from the electromagnetic field:

$$\varepsilon_f = P_f = \frac{B^2}{8\pi} = 4.814 \times 10^{-8} B^{*2} \text{ MeV fm}^{-3}. \quad (113)$$

Note that  $\varepsilon = P_f = 1 \text{ MeV fm}^{-3}$  for a  $B^* = 4.56 \times 10^3$  or  $B \simeq 2 \times 10^{14}$  Gauss. Thus, the field contributions can dominate the matter pressure for  $B^* > 10^4$  at nuclear densities and for  $B^* > 10^5$  at the central densities of neutron stars, and must therefore be included whenever the field dramatically influences the star's composition and matter pressure.

In strong magnetic fields, contributions from the anomalous magnetic moments of the nucleons must also be considered. Experimentally,

$$\kappa_p = \mu_N \left( \frac{g_p}{2} - 1 \right) \quad \text{for the proton} \quad \text{and} \quad \kappa_n = \mu_N \frac{g_n}{2} \quad \text{for the neutron}, \quad (114)$$

where  $\mu_N$  is the nuclear magneton and  $g_p = 5.58$  and  $g_n = -3.82$  are the Landé g-factors for the proton and neutron, respectively. The energy

$$|\kappa_n + \kappa_p|B \simeq 1.67 \times 10^{-5} B^* \text{ MeV} \quad (115)$$

measures the changes in the beta equilibrium condition and to the baryon Fermi energies. Since the Fermi energies range from a few MeV to tens of MeV for the densities of interest, the contributions from the anomalous magnetic moments become significant for  $B^* > 10^5$ . In fact, complete spin polarization of the neutrons occurs when

$$|\kappa_n|B \simeq \frac{(6\pi^2 n_n)^{2/3}}{4m_n}. \quad (116)$$

At nuclear density, this leads to  $B^* \simeq 1.6 \times 10^5$  or  $B \simeq 7.1 \times 10^{18}$  Gauss. Such spin polarization results in an overall stiffening of the EOS (due to the increased degeneracy pressure of neutrons) that overwhelms the softening induced by Landau quantization [159].

Inasmuch as the anomalous magnetic moments of strangeness-bearing hyperons are similar in magnitude to those of nucleons (for a compilation, see Table 1 of [160], magnetic field interactions will be present if hyperons appear in dense matter. The influence of magnetic fields on the EOS of matter containing strangeness-bearing hyperons is characterized by a suppression of hyperons relative to the field-free case as both Landau quantization and the anomalous magnetic moment interactions serve to postpone the densities at which hyperons appear in dense matter [160].

In magnetized matter, the stress energy tensor contains terms proportional to  $HB$ , where  $H = B + 4\pi\mathcal{M}$  and  $\mathcal{M}$  is the magnetization [161]. Thus, extra terms, in addition to the usual ones proportional to  $B^2$ , are introduced into the structure equations [147]. The magnetization in a single component electron gas has been studied extensively by Blandford and Hernquist [162] for neutron star crust matter. The generalization of this formulation to the case of interacting multicomponent matter with and without the effects of the anomalous magnetic moments leads to the result that deviations of  $H$  from  $B$  occur only for field strengths  $B^* \gtrsim 10^5$  [159].

In a magnetic field, the energy of an electron receives contributions from vacuum polarization effects as well. Up to one loop level, these contributions have been calculated by Schwinger [163] with the result  $E_{vac}^e = m_e c^2 \kappa_e$ , where the dimensionless factor  $\kappa_e$  (arising from the anomalous magnetic moment of the electron) takes on sign changing values in the weak and strong field limits:

$$\kappa_e^{wf} = -m_e \frac{\alpha_e}{4\pi} B^*, \quad \text{weak field result},$$

$$\kappa_e^{sf} = \frac{\alpha_e}{2\pi} (\ln 2B^*) , \quad \text{strong field result} , \quad (117)$$

where  $\alpha_e \simeq 1/137$  is the electromagnetic fine structure constant. One can set  $|\kappa_e^{wf}| = 1$  and  $\kappa_e^{sf} = 1$  in order to gauge the fields required to induce a change in the electron Fermi energy (or chemical potential at zero temperature) by an amount  $m_e c^2$ . The results are:

$$\begin{aligned} B^* &= \frac{4\pi}{\alpha_e} \sim 1.7 \times 10^3 \quad \text{or } B \sim 10^{17} \text{ Gauss} , \quad \text{for weak fields} \\ &= \frac{\alpha_e}{2\pi} e \sqrt{2\pi/\alpha_e} \sim 2.8 \times 10^{12} \quad \text{or } B \sim 10^{26} \text{ Gauss} , \quad \text{for strong fields} . \end{aligned} \quad (118)$$

Insofar as the effects of symmetry energy (with shifts of tens of MeV's), Landau quantization and the anomalous magnetic moments of baryons overwhelm the influence on proton fractions, vacuum polarization effects of the electron are not significant except for extremely large fields.

In addition, it must be borne in mind that for super-strong fields exceeding the proton critical field of  $\sim 1.5 \times 10^{20}$  Gauss, the energy density in the field would be significantly larger than the proton's mass energy density. At the proton critical field, the field energy density  $B^2/(8\pi) \sim 0.5 \text{ GeV fm}^{-3}$  is comparable to the energy density of the proton  $\sim 1 \text{ GeV fm}^{-3}$ , which calls for taking the compositeness of the proton seriously.

Figure 15 shows typical results when the effects of Landau quantization and anomalous magnetic moments are included in nucleonic matter. The main lesson to be learned from these results is the softening of the EOS due to Landau quantization, which is, however, overwhelmed by stiffening due to the incorporation of the anomalous magnetic moments of the nucleons. These effects become significant only for fields in excess of  $B^* \sim 10^5$ , for which neutrons become completely spin polarized. Note that this field strength is substantially less than the proton critical field. In addition, the inclusion of ultra-strong magnetic fields leads to a reduction in the electron chemical potential and an increase in proton fraction. Similar results obtain upon the inclusion of hyperons [160]. These compositional changes have implications for neutrino emission via the direct Urca process and, thus, for the cooling of neutron stars [156]. The magnetization of the matter never appears to become very large, as the value of  $|H/B|$  never deviates from unity by more than a few percent.

## B. Magnetic effects on neutron star structure

We turn now to address whether or not stable stellar configurations can exist in which the magnetic field is large enough ( $B > 5 \times 10^{18}$  G) that the properties of matter are significantly affected by the magnetic field. One step in this direction was undertaken in Ref. [147], in which the limits of hydrostatic equilibrium for axially-symmetric magnetic fields in general relativistic configurations were analyzed, including the effects of the magnetic field on the EOS. As discussed in detail in Ref. [147, 158], in axially symmetric field configurations with a constant current function, the magnetic field contributes a centrifugal-like contribution to the total stress tensor. This can be understood by noting that for the field geometry considered (namely axisymmetric), a superconducting fluid can move along field lines but not across them. Thus the ‘‘pressure’’ associated with the magnetic field will only act equatorially and not vertically. This flattens an otherwise spherical star, and for large enough fields, decreases the central (energy) density even as the mass is increased. For large enough fields, the star's stability is eventually compromised.

The question of when is the magnetic field too large is answered to an extent by the results shown in Fig. 16. Results shown here are for the GM3 EOS, both excluding (lower panel) and including (upper panel) hyperons. As with rotation, magnetic fields allow neutron stars with a particular EOS and baryon number to have larger masses and equatorial radii compared to the field-free case. The maximum mass

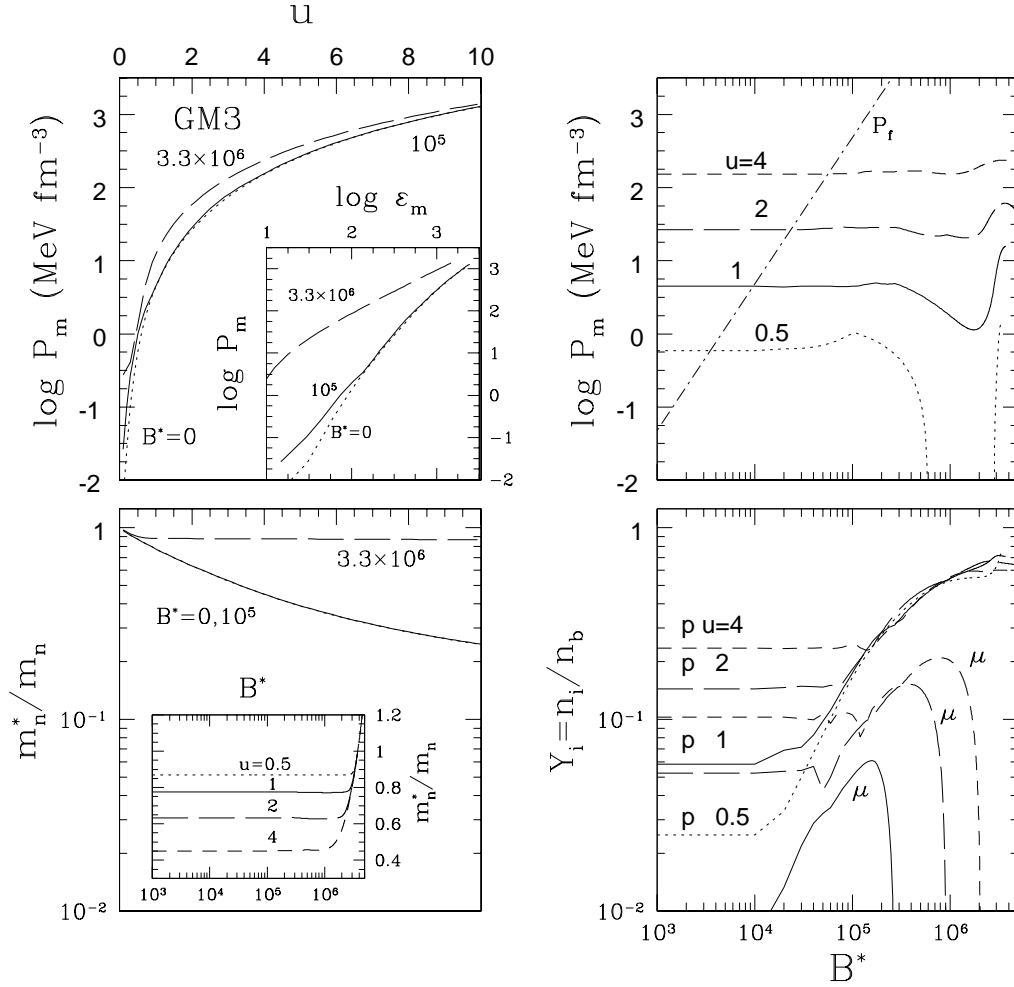


FIG. 15: Matter pressure  $P_m$ , nucleon Dirac effective mass  $m_n^*/m_n$ , and concentrations  $Y_i = n_i/n_b$  as functions of the density  $u = n_b/n_s$  (left panels;  $n_s = 0.16 \text{ fm}^{-3}$  is the fiducial nuclear saturation density) and magnetic field strength  $B^* = B/B_e^c$  (right panels;  $B_e^c = 4.414 \times 10^{13}$  Gauss is the electron critical field), for the model GM3. The inset in the upper left panel shows  $P_m$  as a function of the matter energy density  $\varepsilon_m$ . The curve labeled  $P_f$  in the upper right panel shows the  $B^2/8\pi$  contribution to the total pressure. The inset in the lower left panel shows the effective mass as a function of  $B^*$ . In the lower right panel, the electron and neutron concentrations have been suppressed for clarity ( $Y_e = Y_p - Y_\mu$  and  $Y_n = 1 - Y_p$ ). These results include the effects of Landau quantization and the anomalous magnetic moments in interacting nucleon matter. Figure taken from Ref. [159].

attainable with a magnetic field governed by a constant current function is noticeably larger than that attained by rotation. Hydrostatically stable configurations (of which some may not be stable to dynamical perturbations) are contained between the heavy solid lines. The lower heavy solid line in each panel is the usual field-free, spherical result for the mass-radius relation. The upper heavy solid line represents the largest possible stable mass for a given equatorial radius as the internal magnetic field strength is increased. Large axially-symmetric fields tend to yield flattened configurations, and if large enough, shift the maximum densities off-center (these configurations are contained in the yellow shaded regions in the figure). This results in toroidal shapes with low-density centers. As discussed in Ref. [147], regions to the

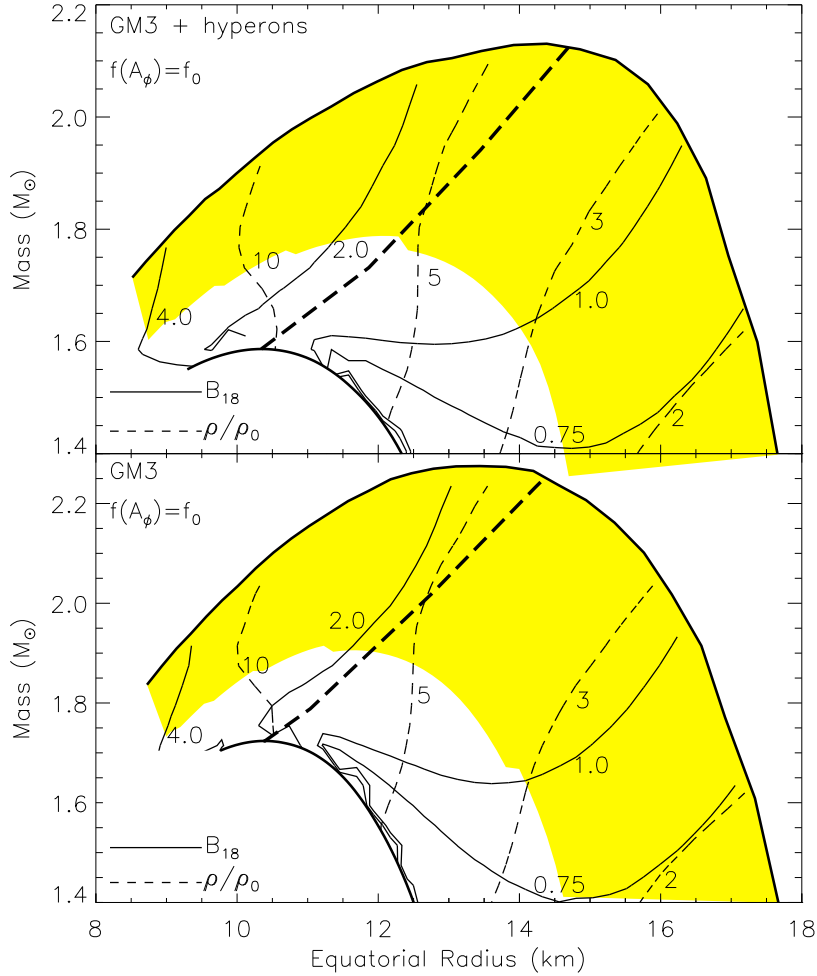


FIG. 16: Limits to hydrostatic configurations for neutron stars permeated by axially symmetric magnetic fields. The upper (lower) panel is for the EOS GM3 including (excluding) hyperons. In each panel, the lower heavy solid curve is the standard mass-radius relation for field-free stars. The upper heavy solid curve represents the largest gravitational mass possible for a given equatorial radius as the magnetic fields are increased, for the indicated current function  $f$ . The yellow shaded region contains configurations in which the maximum density point is off-center. The heavy dashed curve is the locus of minima of the contours of fixed baryon mass configurations: Ref. [147] suggested that this could be the limit to dynamical stability. Thin solid lines are contours of the maximum magnetic field strength in units of  $10^{18}$  G. Similarly, thin dashed lines are contours of maximum mass-energy density in units of the energy density  $\rho_0 = \rho_s$  at the nuclear saturation density. Figure taken from [160].

left of the heavy dashed line, which are the loci of minima of fixed baryon mass configurations, are likely unstable to small amplitude perturbations.

Superimposed on Fig. 16 are contours of maximum mass density and maximum magnetic field strength within a star. For the GM3 model, hyperons appear at zero field at about twice nuclear density. Therefore, the portions of the two panels in which the maximum density is below about 3 times nuclear density are nearly identical. In the case of the GM3 EOS, with or without hyperons, the maximum field value for any presumably stable configuration is  $B \sim 1.8 \times 10^{18}$  G. For a constant current function, and for a variety of

EOSs, Ref. [147] found that the maximum value of the magnetic field in stable stars never exceeds  $3 \times 10^{18}$  G, which corresponds to  $B^* \sim 7 \times 10^4$ . *This field strength is not nearly large enough to produce appreciable effects on the EOS.* This includes changes to the hyperon or nucleon compositions, with or without the inclusion of anomalous magnetic moments. Additionally, the magnetic fields with the assumed current function have relatively small spatial gradients so that the ratio of the maximum field to the average field within the star is not large. Therefore, the dominant effect of the field arises through the magnetic field stress  $B^2/8\pi$ , which effectively dominates the matter pressure below a few times nuclear saturation density, depending on the field's orientation. Whether other choices of current functions, or the relaxation of the condition of axial symmetry, will alter these conclusions has not been explored.

It might be that the shapes of the stars will significantly change with a different field geometry. It is even possible to imagine a disordered field for which  $\langle B^2 \rangle$  is significantly larger than  $\langle \vec{B} \rangle^2$ . In this case the pressure will be dominated by fluctuations in the field, but the stars will tend to be spherical. It is possible that strong magnetic fields may be held in the core for periods much longer than the ohmic diffusion time due to interactions between the magnetic flux tubes and the vortex tubes expected to be present in a superconducting or superfluid rotating neutron star [164]. Although the results to date imply that average fields within a neutron star cannot exceed  $2 - 3 \times 10^{18}$  G before stability is compromised, too small to have a significant impact on the EOS, it is possible that these conclusions are not true in some magnetic field geometries. This is an important subject that deserves additional investigation.

## X. GRAVITY WAVE EMISSION FROM BINARY MERGERS

Mergers of compact objects in binary systems, such as a pair of neutron stars (NS-NS), a neutron star and a black hole (NS-BH), or two black holes (BH-BH), are expected to be prominent sources of gravitational radiation [165]. The gravitational-wave signature of such systems is primarily determined by the chirp mass  $M_{chirp} = (M_1 M_2)^{3/5} (M_1 + M_2)^{-1/5}$ , where  $M_1$  and  $M_2$  are the masses of the coalescing objects. The radiation of gravitational waves removes energy which causes the mutual orbits to decay. For example, the binary pulsar PSR B1913+16 has a merger timescale of about 250 million years, and the pulsar binary PSR J0737-3039 has a merger timescale of about 85 million years [32], so there is ample reason to expect that many such decaying compact binaries exist in the Galaxy. Besides emitting copious amounts of gravitational radiation, binary mergers have been proposed as a source of the r-process elements [166] and the origin of the shorter-duration gamma ray bursters [167].

From the point of view of neutron star structure, observations of gravity waves from merger events offer a unique opportunity to simultaneously measure masses and radii, and could set extreme limits on the neutron star maximum mass. Current detectors may not have the ability to receive information expected at high frequencies from NS-NS mergers, so our discussion focuses on BH-NS binaries. From the inspiral waves, masses of the binary components can be measured. The inspiral terminates either due to tidal disruption or to the stars' reaching their mutual ISCO. In either case, measurement of the gravity-wave frequency at this point can be used to infer the neutron star radius [168]. Furthermore, from the ringdown phase, the mass of the final merged remnant can be found. The binding energy thus observed can be connected to  $M/R$  and/or the EOS (see §VIII B). Moreover, a signal might be observable from a super-sized neutron star formed from the pair if a black hole doesn't form. This would set a lower limit to the neutron star maximum mass that is substantially larger than at present. Importantly, as demonstrated below, the wave pattern emitted if one of the components is a strange quark star is substantially different than that of a normal hadronic star.

### A. Tidal disruption and mass transfer

A neutron star in a binary merger with a larger mass companion will be tidally disrupted. This occurs when the radius of the less massive component exceeds the innermost equipotential surface (*i.e.*, its Roche lobe) surrounding the two stars that includes the first, or inner, Lagrange point. If the tidal disruption occurs far enough outside the innermost stable circular orbit (ISCO) of the binary, it is expected that an accretion disc will form or that mass transfer to its companion will occur [169, 170, 171]. In either case, the gravity wave signal is expected to be significantly different than if tidal disruption occurs after the star penetrates the ISCO.

Tidal disruption or the onset of mass transfer depends upon the EOS of dense matter and the mass ratio  $q = M_1/M_2$  of the binary. If mass can be transferred quickly enough from the lighter to the heavier star, conservation of mass and orbital angular momentum can be assumed, which generally leads to a reversal of inspiral. The binary separation widens. Although this increases the Roche lobe volume, the radius of the neutron star also increases in response to the mass loss. Mass transfer will continue in a stable fashion if the lighter star can expand sufficiently fast such that it is able to continuously fill its Roche surface. Mass transfer under such conditions is termed *stable mass transfer*. Because the orbital separation now increases, the gravity wave amplitude and frequency will decrease. The signature of stable mass transfer in gravity waves should therefore be strikingly different than for an amorphous tidal disruption or a direct plunge.

As we show below, important information about the radius of a neutron star and the underlying EOS could be contained in the gravity wave signal. For example, the expected gravity-wave signal from a merger involving a neutron star should be quite different than from a self-bound strange quark matter star. In addition, the longer timescale produced by stable mass transfer might also extend the duration of the event from millisecond timescales, the orbital timescale near the ISCO, to a few seconds, which then could explain the duration of short-timescale gamma ray burst [171].

Another effect of stable mass transfer would be to modify the amount of material potentially ejected from the system. Matter from a tidally disrupted neutron star, which could be accelerated to escape velocities from the binary [166], undergoes decompression which results in heavy nuclei and an intense neutron flux leading to the copious production of r-process elements [172, 173]. In the case in which stable mass transfer occurs, sudden disruption of the neutron star near the last stable orbit is avoided, but mass could be ejected more easily at later times and at larger separations when the neutron star approaches its minimum stable mass [174].

### B. Merger evolution

Here we explore the qualitative character of a binary merger using a relatively simple model that ignores relativistic corrections to the Roche geometry and the orbital evolution but still reproduces the qualitative features of more sophisticated models [175]. This model is similar in some respects to that of Ref. [171] but correctly includes the effects of the EOS. To be definite, we consider a low-mass BH-NS system, with  $M_{NS} \simeq 1.4 M_\odot$  and  $M_{BH} \simeq 3-10 M_\odot$ . The original orbit decays by the emission of gravitational radiation. Denoting the total orbital mass  $M + M_{BH} + M_{NS}$ , the reduced mass  $\mu = M_{BH}M_{NS}/M$ , and the mass ratio  $q = M_{NS}/M_{BH}$ , the rate of change of orbital angular momentum  $J$  is [176]

$$\dot{J}_{GW} = -\frac{32}{5} \frac{G^{7/2}}{c^5} \frac{\mu^2 M^{5/2}}{a^{7/2}} = -\frac{32}{5} \frac{G^{7/2}}{c^5} \frac{q^2 M^{9/2}}{(1+q)^4 a^{7/2}}, \quad (119)$$

where  $a$  is the orbital semi-major axis and

$$J^2 = GM\mu^2 a = GM^3 a q^2 (1+q)^{-4}. \quad (120)$$

The orbital frequency is

$$\omega = \sqrt{\frac{GM}{a^3}}. \quad (121)$$

These equations are valid for circular orbits, but it can be shown that the timescale for decay of orbital eccentricity is much shorter than the timescale for decay of semi-major axis  $a$ , which for circular orbits is equivalent to the orbital separation.

The binary shrinks until tidal disruption ensues. This occurs when the neutron star fills its Roche radius, the gravitational equipotential surface that passes through the inner Lagrange point, and mass begins to flow to its companion. In Newtonian gravity, the Roche radius  $R_\ell$  is well approximated by Kopal's formula [177]

$$R_\ell/a = 0.46[q/(1+q)]^{1/3}, \quad (122)$$

or a better fit by Eggleton [178]

$$R_\ell/a = 0.49/[0.6 + q^{-2/3} \ln(1 + q^{1/3})]. \quad (123)$$

Thus, mass overflow begins at the moment that  $R_\ell = R$ , or

$$a = R(R_\ell/a)^{-1}, \quad (124)$$

where  $R$  is the neutron star radius. Note that both  $R_\ell/a$  and  $a$  are decreasing functions of  $q$  for fixed  $M$  and  $J$ . Mass transfer will continue in a stable fashion if the star's radius, after an increment of mass transfer, is less than  $R_\ell$ , so that continued gravitational radiation will result in renewed mass transfer, or

$$\frac{d \ln R}{d \ln M_{NS}} \equiv \alpha \leq \frac{d \ln R_\ell}{d \ln M_{NS}} = \frac{d \ln a}{d \ln M_{NS}} + (1+q) \frac{d \ln(R_\ell/a)}{d \ln q}, \quad (125)$$

where  $M$  is assumed constant. Eq. (125) defines the parameter  $\alpha$ , which is a function of the EOS and  $M_2$ . It is  $\alpha$  which determines both the onset of stable mass transfer and the subsequent evolution. If Kopal's formula is used, the second term on the right-hand side of Eq. (125) is just 1/3.

If the mass transfer is assumed to conserve orbital angular momentum, the evolution of the system will be defined by

$$\frac{d \ln J}{dt} = \frac{1}{2} \frac{d \ln a}{dt} + \frac{1-q}{1+q} \frac{d \ln q}{dt} = \frac{\dot{J}_{GW}}{J} = -\frac{32 G^3}{5 c^5} \frac{q M^3}{(1+q)^2 a^4}. \quad (126)$$

Combining this with Eq. (125), one finds

$$\frac{\dot{J}_{GW}}{J} \geq \left( \frac{d \ln q}{dt} \right) \frac{1}{2(1+q)} \left[ \alpha + 2(1-q) - (1+q) \frac{d \ln(R_\ell/a)}{d \ln q} \right]. \quad (127)$$

Since both  $\dot{J}_{GW}$  and  $\dot{q}$  are negative, the condition for stable mass transfer becomes

$$\alpha + 2(1-q) - (1+q) \frac{d \ln(R_\ell/a)}{d \ln q} \geq 0 \quad (128)$$

Using Kopal's formula, Eq. (122), this is simply  $\alpha \geq 2q - 5/3$ . For hadronic stars near  $1.4 M_\odot$ ,  $\alpha \sim 0$ , so  $q < 5/6$  is the condition. For strange quark stars not near the maximum mass,  $\alpha \sim 1/3$ , and  $q < 1$  is the condition. Thus, all NS-NS and BH-NS binaries containing strange quark matter stars will likely have epochs of stable mass transfer. However, some NS-NS binaries with  $q \sim 1$  may not show this phenomenon.

During stable mass transfer,  $\dot{a} > 0$  and, hence, the binary spirals apart. However, if the condition Eq. (128) is subsequently violated, mass transfer becomes unstable at that point and the remaining neutron star will quickly tidally disrupt.

Equations (125) (with the equal sign) and (126) determine the time evolution of  $a$  and  $q$ . From these quantities, all other relevant quantities can be determined during mass transfer. The details will depend upon the EOS. The two main observables will be the gravity wave amplitude and the frequency of the gravity waves as a function of time. The scalar gravitational polarization amplitude (or dimensionless strain) is

$$h_+(t) = \frac{4}{r} \frac{4G^2 M^2}{ac^4} \frac{q}{(1+q)^2} \cos 2\omega(t-r), \quad (129)$$

where  $r$  is the distance from the binary system to the observer. The observed frequency of the emitted gravitational waves will be twice the orbital frequency  $\omega$  Eq. (121). Typical values are  $|h_+ r| \simeq 2 \times 10^{-19}$  pc and  $\nu = \omega/2! \pi \simeq 0.1 - 0.5$  kHz.

### C. The EOSs of normal versus self-bound stars

It is useful to examine the behavior of the function  $\alpha(M_{NS})$  for both neutron stars and self-bound strange quark matter stars. For the discussion at hand, we will use the term normal star to refer to a star with a surface of normal matter in which the pressure vanishes at vanishing baryon density. The interior of the star, however, may contain any or a combination of exotica such as (1) strangeness-bearing matter in the form of hyperons, kaons, or quarks, (2) Bose (pion or kaon) condensed matter, and (3) quark matter.

A self-bound star, as exemplified by Witten's conjecture that strange quark matter might be more stable than normal matter at zero pressure [1, 179], has a bare quark matter surface in which the pressure vanishes at a finite but supra-nuclear baryon density. In the context of the MIT bag model with first order corrections due to gluon exchange, the baryon density at which pressure vanishes is

$$n_b(P=0) = (4B/3\pi^{2/3})^{3/4} (1 - 2\alpha_c/\pi)^{1/4}, \quad (130)$$

where  $B$  is the bag constant and  $\alpha_c = g_c^2/(4\pi)$  is the quark-gluon coupling constant. This density is not significantly affected by the finite strange quark mass [180] or by the pairing phenomenon in quark matter [181].

Examples of radius versus mass for broadly differing EOSs selected from [6] are shown in Fig. 17. While quantitative differences exist among normal stars, a rough representation of  $\alpha(M_{NS})$  for low mass stars is [175]

$$\alpha \approx -\frac{0.09}{M_{NS}/M_\odot - 0.09}. \quad (131)$$

This relation is useful in understanding detailed numerical simulations. Qualitative differences in the outcomes of mergers with a black hole emerge, however, because of the gross differences in the mass-radius diagram of normal and self-bound stars. Thus, a normal star and a self-bound star represent two quite different possibilities (see the right panel in Fig. 17):

$$\alpha \equiv \frac{d \ln R}{d \ln M} \begin{cases} \leq 0 & \text{for a normal neutron star (NS)} \\ \geq 0 & \text{for a self-bound SQM star} \end{cases}. \quad (132)$$

We will explore the astrophysical consequences of these distinctive behaviors in BH-NS mergers.

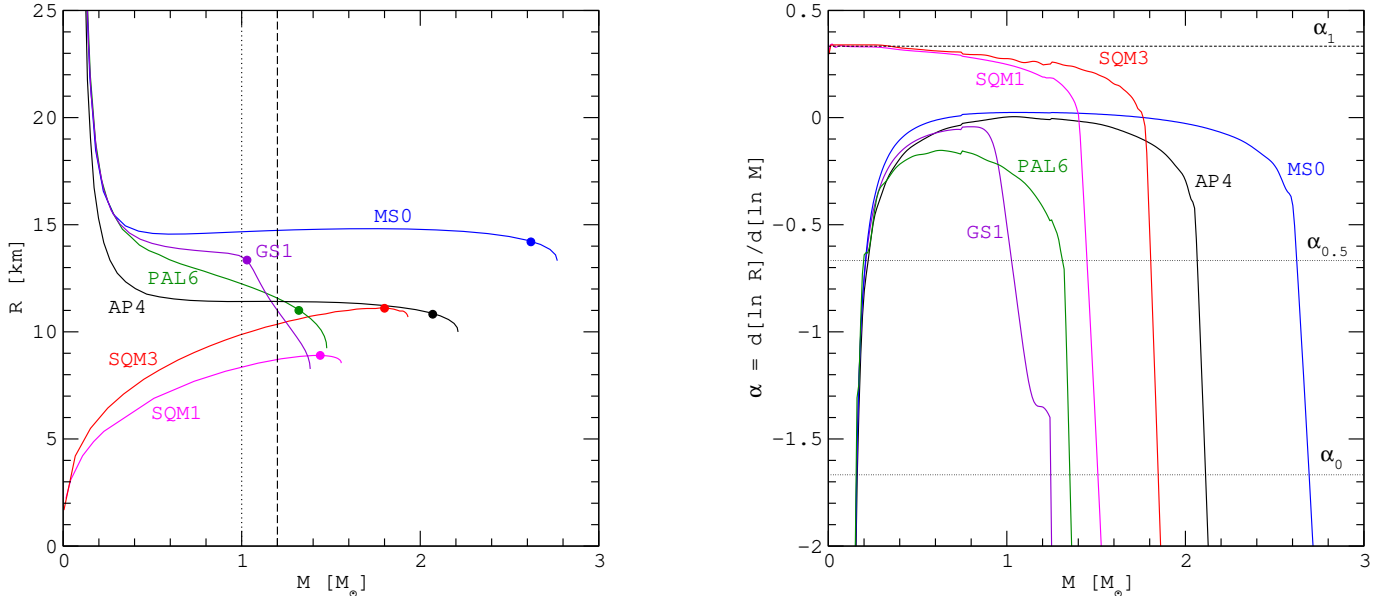


FIG. 17: Radius versus mass (left panel) and its logarithmic derivative (right panel) for prototype EOSs. The EOS symbols are as in [6]. The vertical lines in the left panel and the horizontal lines in the right panel are discussed in text. In the left panel, the maximum masses for which stable mass transfer is allowed in the case  $q = M_{NS}/M_{BH} = 0.5$  are denoted by filled circles for each EOS.

Note that  $\alpha$  is intimately connected with the dense matter EOS, since there exists a one-to-one correspondence between  $R(M)$  and  $P(n_B)$ , where  $P$  is the pressure and  $n_B$  is the baryon density. Gravitational mergers in which a compact star loses significant mass during evolution is one of the rare examples in which the  $R$  versus  $M$  (or equivalently,  $P$  versus  $n_B$ ) relationship of the same star is sampled. Although we focus here on the coalescence of a compact star with a BH, the theoretical formalism and our principal findings apply also to NS-NS mergers.

#### D. Model evolutions

Figure 18 shows the results of integrating Eqs. (125) and (126) for simulations involving a  $4.5 M_\odot$  black hole and a  $1.5 M_\odot$  normal or self-bound quark star. Although both simulations result in stable mass transfer, there is a pronounced qualitative difference between the results after mass transfer begins. Inspiral is characterized by increases in the orbital frequency  $\omega$  and scalar gravitational polarization amplitude  $h_+$ , a decrease in orbital separation  $a$ , and a fixed  $q$ . Stable mass transfer ensues at the “kinks” visible in the evolution of these quantities. Within each class of EOS, i.e., normal and self-bound stars, variations in the EOS only qualitatively alter the results. During stable mass transfer, the decrease in orbital separation and rise in frequency and waveform amplitudes are reversed.

In the neutron star case, the star spirals outwards and loses mass at an approximately constant rate. Mass loss continues for a few seconds until the star approaches but does not decrease below its minimum mass (about  $0.1 M_\odot$ ). Mass transfer becomes unstable at this point, and full tidal disruption including explosive decompression of the remnant is to be expected in this case [174]. On the other hand, the quark star loses mass exponentially and *remains at a nearly fixed orbital separation* during this period. Mass loss continues for a virtually infinite time. As a result, the temporal behavior of the gravity wave emissions,

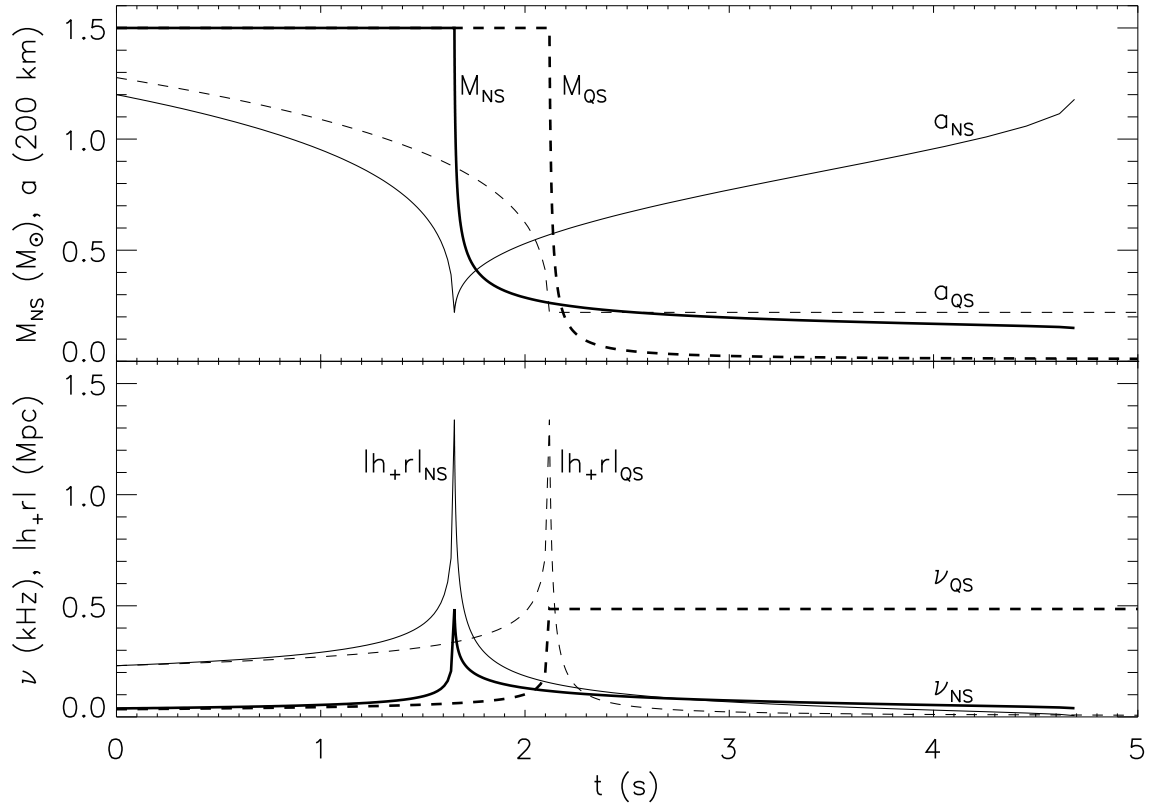


FIG. 18: Schematic behavior of physical and observational variables in mergers between low-mass black holes and neutron stars or self-bound quark stars. The total system mass is  $6 M_{\odot}$  and the initial mass ratio is  $q = 1/3$  in both cases. The initial radii of the neutron star and quark star were assumed to be equal. The time scales have arbitrary zero points. Upper panel displays semi-major axis  $a$  (thick lines) and component mass  $M_{NS}, M_{QS}$  (thin lines) evolution. Lower panel displays orbital frequency  $\nu$  (thick lines) and strain amplitude  $|h_+ r|$  evolution. In both panels, solid curves refer to the neutron star simulation and dashed curves to the quark star simulations.

both of the amplitude and the frequency, from these two types of mergers significantly differ, as seen in Fig. 18.

The major effect of incorporating general relativistic corrections to the potential is to speed up the evolution relative to the Newtonian case [175]. Stable mass transfer thus begins earlier in these cases. GR corrections also result in a somewhat larger value for the orbital separations following the onset of mass transfer.

Using the relations established in the previous sections, one can readily understand qualitatively and quantitatively the results shown in Fig. 18. For example, the binary separation when mass transfer begins is, from Eq. (124),  $a \simeq R(4/3)^{1/3}/0.46 \simeq 44$  km for the two cases shown (assuming  $R = 12$  km). The orbital frequency will be a maximum here,  $\nu = (\omega/2\pi) \simeq 500$  Hz, from Eq. (121).

In the neutron star case, mass loss continues until the condition Eq. (128) is violated. This occurs before the minimum mass is reached, since near the minimum mass  $\alpha \rightarrow -\infty$ . The binary separation increases since, using Kopal's formula, Eq. (122),  $d \ln a / d \ln q = (\alpha - 1/3)/(1 + q)$  is negative for  $\alpha < 1/3$ , which is always true for neutron stars.

However, in the quark star case, the binary separation remains nearly fixed since  $\alpha - 1/3 \simeq 0$ , especially

for  $q \rightarrow 0$ . The condition Eq. (128) is never violated for quark stars, so mass transfer is not terminated. Using Kopal's formula and setting  $\alpha = 1/3$ , one arrives at the evolution equation

$$\frac{dq}{dt} = -\frac{32}{5} \frac{G^3}{c^5} \frac{M^3 q^2}{1 - q^2} \left(\frac{0.46}{R_Q}\right)^4 \left(\frac{M_Q}{M}\right)^{4/3}, \quad (133)$$

where  $R_Q$  and  $M_Q$  are the quark star's initial radius and mass, respectively. This is trivially integrated to find the elapsed time to go from an initial mass ratio  $q_i$  to a final mass ratio  $q_f$

$$\Delta t = \frac{5}{32M^3} \frac{c^5}{G^3} \left(\frac{R_Q}{.46}\right)^4 \left(\frac{M}{M_Q}\right)^{4/3} \left[ \frac{q_f^2 + 1}{q_f} - \frac{q_i^2 + 1}{q_i} \right] \simeq 0.002 q_f^{-1} \text{ s}, \quad (134)$$

where we assumed in the final step that  $q_f \ll q_i$ . Thus, the mass of the self-bound star dwindles to extremely small values  $< 10^{-30} M_\odot$ , the minimum mass limit being that of a strange quark nugget, determined in part by surface and Coulomb effects. This takes, from Eq. (134), more than  $10^{27}$  s.

The envelope of the gravitational waveform amplitude  $|h_+(t)|$  follows the behavior of  $q$  and  $a$ . In the normal neutron star case, following the onset of stable mass transfer, the amplitude decreases steadily until stable mass transfer terminates, but decreases much more rapidly in the the quark star case.

### E. Observational parameters

As discussed in Ref. [182], careful analysis of the gravitational waveform during inspiral yields values for not only the chirp mass  $M_{chirp} = (M_{BH} M_{NS})^{3/5} / M^{1/5}$ , but for also the reduced mass  $M_{BH} M_{NS} / M$ , so that both  $M_{BH}$  and  $M_{NS}$  can be found. Thus, observation of stable mass transfer effects in the gravitational wave signal will allow several details about neutron star structure to be discerned, including several features of the underlying EOS. For example, the onset of mass transfer can be determined by the peak in  $\omega$ , and the value of  $\omega$  there gives  $a$ . The Roche limit condition Eq. (124), as modified by general relativity [175], then allows the determination of the star's radius. Thus a point on the mass-radius diagram can be estimated [183].

This information can be supplemented using the gravitational wave amplitudes  $h_+$  at its peak and at the end of stable mass transfer. The combination  $h_+ \omega^{-1/3}$  depends only on a function of  $q$ , so the ratio of that combination and knowledge of  $q_i$  should allow determination of  $q_f$ . From the Roche condition and knowledge of  $a_f$  from  $\omega_f$ , another mass-radius combination can be found.

The time elapsed between the onset of stable mass transfer and its termination depends in a complicated way on  $q$ ,  $M$  and  $\alpha(M)$ . Nevertheless, measurement of this time, assuming that  $q$  and  $M$  are already measured, implies that the function  $\alpha$  can be constrained.

Most importantly, the sharp contrast between the evolutions during stable mass transfer of a normal neutron star and a strange quark star should make these cases distinguishable even if other information concerning the values of  $q$ ,  $M$  and  $R$  is weak. This result is independent of the form of the gravitational potential or the nuclear or quark matter EOS employed.

Finally, for the case of strange quark matter stars, the differences in the height of the frequency peak and the plateau in the frequency values at later times are related to the differences in radii of the stars at these two epochs. (In Fig. 18, the peak and the plateau are coincident because  $\alpha = 1/3$  was assumed for all masses.) It could be an indirect indicator of the maximum mass of the star: the closer is the star's mass before mass transfer to the maximum mass, the greater is the difference between these frequency values, because the radius change will be larger. Together with radius information, the value of the maximum mass remains the most important unknown that could reveal the true equation of state at high densities.

## XI. CONSTRAINTS FROM LABORATORY DATA

We turn now to opportunities afforded by laboratory experiments to constrain the dense matter equation of state. Supplements to our brief account here are contained in several reviews, some of which are alluded to below.

### A. Nuclear masses

The most fundamental property of a nucleus is its binding energy, or mass defect relative to the total individual masses of its  $Z$  protons and  $N$  neutrons. The first giant leap to understand the nuclear mass systematics was taken by Bethe and von-Weizsäcker who developed the semi-empirical mass formula using the liquid-drop model. Incorporating realistic nuclear surfaces and effects stemming from neutron-proton asymmetries, Myers and Swiatecki [185] formulated the droplet model approach in which the nuclear energy can be written as

$$\begin{aligned}
 E(A, Z) = & -BA + E_s A^{2/3} + S_v A \frac{(1 - 2Z/A)^2}{1 + S_s^*/(S_v A^{1/3})} + E_C \frac{Z^2}{A^{1/3}} \\
 & + E_{dif} \frac{Z^2}{A} + E_{ex} \frac{Z^{4/3}}{A^{1/3}} + a\Delta A^{-1/2}.
 \end{aligned} \tag{135}$$

In this expression,  $B \simeq 16$  MeV is the binding energy per particle of bulk isospin symmetric matter at saturation,  $E_s, E_C, E_{dif}$  and  $E_{ex}$  are coefficients for the surface energy of symmetric matter, the Coulomb energy of a uniformly charged sphere, the diffuseness correction and the exchange correction to the Coulomb energy, respectively. The last term represents pairing corrections, where  $\Delta$  is a constant and  $a = +1$  for odd-odd nuclei, 0 for odd-even nuclei, and  $-1$  for even-even nuclei. For simplicity, the effects of curvature and higher-order terms are neglected. The quantity  $S_v$  is the usual symmetry energy coefficient and the quantity  $S_s^*$  is related to the surface tension associated with the asymmetry parameter  $\delta = (n_n - n_p)/(n_n + n_p)$  according to

$$S_s^* = 4\pi \left( \frac{3}{4\pi n_s} \right)^{2/3} \sigma_\delta. \tag{136}$$

Note that the surface energy  $E_s = 4\pi r_0^2 \sigma$  ( $\delta = 0$ ) and the surface symmetry energy  $S_s = 4\pi r_0^2 \sigma_\delta$ , where  $(4\pi r_0^3/3)(0.16 \text{ fm}^{-3}) = 1$ , so that  $S_s^*$  and  $S_s$  differ only in the values of the equilibrium densities used.

For the description of nuclei in the equation of state relevant for astrophysical simulations of supernovae and neutron stars, the droplet approach for isolated nuclei has been extended to the case in which nuclei are immersed in a dense medium comprised of electrons, positrons, protons, neutrons and alpha particles [186]. The determination of the various parameters entering Eq. (135) is afforded by the experimental nuclear masses. Fits of Eq. (135) to currently available masses have revealed interesting linear correlations, particularly for  $S_s/S_v$  with  $S_v$ . Theoretically,  $S_s/S_v$  is closely connected to the neutron skin thickness  $\delta R = \langle r_n^2 \rangle^{1/2} - \langle r_p^2 \rangle^{1/2}$ . (For recent accounts, see [187, 188] and references therein.) For example, and depending on the precise way in which the nuclear surface and Coulomb attributes are treated, correlations emerging from equivalent fits to nuclear masses are

$$S_s/S_v = -5.253 + 0.254S_v \quad \text{or} \quad S_s/S_v = -3.453 + 0.163S_v. \tag{137}$$

Tighter constraints will be provided by a larger number of experimental masses for nuclei with  $N > Z$ , highlighting the importance of new mass measurements using rare isotope accelerators (RIA). For new developments in techniques of measuring masses of short-lived nuclei off the stability line, see Refs. [189].

## B. Nuclear matter compression modulus

The task of determining the isospin symmetric nuclear matter compression modulus

$$K = 9n_s^2 \left. \frac{d^2(E/A)}{dn^2} \right|_{n_s}, \quad (138)$$

where  $E/A$  is the energy particle (determined from the empirical nuclear masses) at the nuclear equilibrium density  $n_s \simeq 0.16 \text{ MeV fm}^{-3}$  (determined from electron and hadron scattering experiments on nuclei), has been arduous on both experimental and theoretical fronts. Thanks to vastly improved experimental techniques, the identification and analysis of isoscalar giant monopole and isoscalar giant dipole resonances have been accomplished for light to heavy nuclei such as  $^{70}\text{Zr}$ ,  $^{116}\text{Sn}$  and  $^{208}\text{Pb}$ . Equally challenging theoretical analyses of the data based on fully self-consistent Hartree-Fock plus random phase approximation (RPA) calculations have now been performed utilizing both non-relativistic potential and relativistic field-theoretical models. The conclusions that emerge from these combined experimental and theoretical efforts are:

1. The isoscalar giant monopole resonance data yields  $K = 240 \pm 20 \text{ MeV}$ . The uncertainty of about 20 MeV is mainly due to the density dependence of the symmetry energy around  $n_s$ ; and
2. The isoscalar giant dipole resonance data tend to point toward lower values of  $K$ . However, there is consensus that the extraction of  $K$  in this case is largely experimental as the maximum cross section decreases very strongly at high excitation energy and likely drops below the current experimental sensitivity for excitation energies above 30 and 26 MeV for  $^{116}\text{Sn}$  and  $^{208}\text{Pb}$ , respectively. With improved experimental techniques and analysis, these difficulties may be overcome.

An excellent account of these developments can be found in the recent short review (and in other articles) by Shlomo et. al. [190].

## C. Symmetry energy and giant dipole resonances

The analyses of giant resonances, particularly dipole resonances, have long served to delineate the role of volume and surface effects in nuclei; for a review see Ref. [191]. In medium to heavy nuclei in which magnetic contributions are small, the inverse-energy-squared weighted photoabsorption cross section  $\sigma_{-2}$  can be related to the static polarizability  $p$  as

$$\sigma_{-2} = \int \frac{\sigma(\omega)}{\omega^2} d\omega = 2\pi^2(e^2/\hbar c)p. \quad (139)$$

In nuclei with mass number  $A \geq 100$ ,  $\sigma_{-2} = (2.9 \pm 0.2)A^{5/3} \mu\text{b MeV}^{-1}$  parameterizes the data [192, 193]. The dipole polarizability can be evaluated as the response of a nucleus to an external dipole field  $\eta D$ , where  $\eta$  denotes the strength and  $D = (1/2) \sum_{i=1}^A z_i \tau_i^3$  is the dipole operator. Explicitly,

$$p = 2 \sum_{n \neq 0} \frac{|\langle 0 | D | n \rangle|^2}{\omega_n - \omega_0}, \quad (140)$$

where  $|n\rangle$  and  $\omega_n$  are the eigenstates and eigenenergies of the nuclear Hamiltonian responsive to the dipole operator  $D$ .

Microscopic RPA calculations [194] of  $p$  employing Skyrme-like interactions reproduce the general trends of the data. The interplay between volume and surface effects are, however, difficult to extract from RPA calculations. Semiclassical methods, in which the energy density formalism is coupled with a hydrodynamic approach to describe collective excitations, have thus been employed to explore how the volume and surface symmetry energies,  $S_{v0}$  and  $S_s$ , determine the value of  $p$  across the periodic table [191, 195, 196]. Starting from a given Hamiltonian density, and writing the transition density as  $\delta[\rho_n(r) - \rho_p(r)] = \eta\phi(r) \cos\theta$ , the polarizability is calculated from

$$p = \frac{2\pi}{3} \int \phi(r)r^3 dr, \quad (141)$$

where  $\phi(r)$  is the solution of the corresponding Euler-Lagrange (integro-differential) equation. Investigations have found that similar results for  $p$  are obtained for correlated values of  $S_v$  and  $S_s$ . Numerical results for  $^{40}\text{Ca}$ ,  $^{120}\text{Sn}$ , and  $^{208}\text{Pb}$  show that the choice of  $S_v$  in the range 27–42 MeV requires  $|S_s/S_v| = 1.2$ –2.2; lower values of  $S_v$  demand lower values of  $S_s$  for good fits [196].

A qualitative understanding of this correlation can be gained by using a schematic symmetry energy density functional and a leptodermous expansion of the density [191], whence one obtains the result

$$p = \frac{A \langle r^2 \rangle}{24 S_v} \left( 1 + \frac{5 S_s}{3 S_v} A^{-1/3} + \dots \right), \quad (142)$$

where  $\langle r^2 \rangle$  is the mean square radius of the nucleus and higher order terms contain corrections from the diffuseness and the skin thickness. Although values of  $S_v = 32.5$  MeV and  $|S_s/S_v| = 2.2$  describe the data adequately [191], correlated variations in these numbers are allowed as pointed out in Ref. [196].

Sum rules have been particularly useful to relate experiments and theory in discussing the mean excitation energies, widths, and the spreading of the excitation strengths [191]. The moments  $m_p$  of the strength function  $S(\omega) = \sum_{n>0} |\langle n | F | 0 \rangle|^2 \delta(\omega - \omega_n)$  defined by

$$m_p = \int_0^\infty S(\omega)\omega^p d\omega = \sum_{n>0} |\langle n | F | 0 \rangle|^2 \omega_n^p, \quad (143)$$

where  $F$  is the physical operator exciting the nucleus from its ground state  $|0\rangle$  to its eigenstate  $|n\rangle$ , are especially helpful in this regard. For example, a good measure of the mean excitation energy is provided by  $E(D) = \sqrt{m_1/m_{-1}}$ , for which results from RPA and hydrodynamic calculations have been compared with data [191]. Using a droplet model coupled with a hydrodynamic approach to excite the dipole resonance, Ref. [197] obtains

$$E(D) = \sqrt{\frac{6\hbar^2(1 + K_D)}{M \langle r^2 \rangle} \frac{S_v}{[1 + 5S_s/(S_v A^{1/3})]}}, \quad (144)$$

where  $M$  is the nucleon mass. The quantity  $K_D$  is a model dependent enhancement factor characterizing the relative contribution of the nuclear interaction to the  $m_1$  sum rule and depends critically on the value of the energy up to which the energy integration is carried out in analyzing the experimental data. Using values of  $S_v = 32.5$  MeV and  $S_s/S_v \simeq 2$  from a droplet model fit to nuclear energies, and  $K_D = 0.2$  corresponding to  $E_{max} = 30$  MeV, Ref. [197] finds that a hydrodynamic approach is able to reproduce the experimental mean excitation energy of nuclei ranging from  $^{40}\text{Ca}$  to  $^{208}\text{Pb}$  reasonably well. Several Skyrme interactions with different values of  $S_v$  and  $S_s/S_v$  are also able to account for the data to the same level of accuracy. However, since the values of  $S_v$  and  $S_s$  for these forces are correlated because they are fit to experimental masses, the additional constraint on the permitted ranges of  $S_v$  and  $S_s$  resulting from fitting dipole resonances does not seem to be significant.

It must be emphasized that while a hydrodynamic approach is able to account for the gross features of nuclear mass dependence, several detailed features of the data such as strength fractionation, spreading widths, etc., are not naturally incorporated in its scope. For such details one must adopt a more microscopic approach that includes, for example, contributions from 2p–2h excitations, etc. For a detailed account, see, for example, Ref. [198].

#### D. Neutron skin thickness in nuclei

Unlike proton distributions, neutron distributions in nuclei have remained uncertain to this date. Studies of neutron densities from a global analysis of medium-energy proton scattering on  $^{208}\text{Pb}$  indicate that  $0.07 < \delta R < 0.16$  fm [199]. Related information is also available from an analysis of antiprotonic atom data that gives  $\delta R = 0.15 \pm 0.02$  fm [200]. In the latter work, nucleon density distributions are parameterized by Fermi functions and it is found that the half-density radii for neutrons and protons in heavy nuclei are the same, but the diffuseness parameter for the neutrons is larger than that for the protons. Skin thicknesses as large as 0.2 fm were obtained in earlier analyses [201]. Since these studies involve strongly interacting probes, even to this date the value of  $\delta R$  for a nucleus such as  $^{208}\text{Pb}$  is not accurately known. This situation should improve as it is expected that the neutron rms radius will be determined to about 1% accuracy by measuring the parity-violating electroweak asymmetry in the elastic scattering of polarized electrons from  $^{208}\text{Pb}$  [202]. This experiment, named PREX, is planned at the Jefferson Laboratory [203] for the summer of 2008.

The neutron skin thickness is of interest as the pressure of neutron star matter below and above the saturation density  $n_s$  depends on the density dependence of the isospin asymmetric part of the nuclear interaction. Typel and Brown [204, 205] have noted that model calculations of the difference between neutron and proton rms radii  $\delta R = \langle r_n^2 \rangle^{1/2} - \langle r_p^2 \rangle^{1/2}$  are linearly correlated with the pressure of pure neutron matter at a density below  $n_s$  characteristic of the mean density in the nuclear surface (e.g.,  $0.1 \text{ fm}^{-3}$ ). The density dependence of the symmetry energy controls  $\delta R$  (we will call this the neutron skin thickness) in a heavy, neutron-rich nucleus. Explicitly,  $\delta R$  is proportional to a specific average of  $[1 - S_v/E_{sym}(n)]$  in the nuclear surface, see Refs. [74, 75].

Horowitz and Piekarewicz [206] have pointed out that models that yield smaller neutron skins in heavy nuclei tend to yield smaller neutron star radii. These authors, along with others [202, 203], have also pointed out the need for an accurate measurement of the neutron skin.

For the connection between isospin asymmetry in nuclei and properties of neutron stars, see the recent review by Steiner et al. [187].

#### E. Heavy-Ion Collisions

##### 1. Collective Flow

Nuclear collisions in the range  $E_{lab}/A = 0.5 - 2$  GeV offer the possibility of pinning down the equation of state of matter above normal nuclear density (up to  $\sim 2$  to  $3n_s$ ) from a study of matter, momentum, and energy flow of nucleons [207]. The observables confronted with theoretical analyses include (i) the mean transverse momentum per nucleon  $\langle p_x \rangle/A$  versus rapidity  $y/y_{proj}$  [208], (ii) flow angle from a sphericity analysis [209], (iii) azimuthal distributions [210], and (iv) radial flow [211]. Flow data gathered to date are largely for protons (as detection of neutrons is more difficult) and for collisions of laboratory nuclei in which the isospin asymmetry is not large. Theoretical calculations have generally been performed using Boltzmann-type kinetic equations. One such equation for the time evolution of the phase space distribution

function  $f(\vec{r}, \vec{p}, t)$  of a nucleon that incorporates both the mean field  $U$  and a collision term with Pauli blocking of final states is (see, for example, Ref. [212])

$$\begin{aligned} \frac{\partial f}{\partial t} + \vec{\nabla}_p U \cdot \vec{\nabla}_r f - \vec{\nabla}_r U \cdot \vec{\nabla}_p f = & - \frac{1}{(2\pi)^6} \int d^3 p_2 d^3 p_{2'} d\Omega \frac{d\sigma_{NN}}{d\Omega} v_{12} (2\pi)^3 \delta^3(\vec{p} + \vec{p}_2 - \vec{p}_{1'} - \vec{p}_{2'}) \\ & \times [f f_2 (1 - f_{1'}) (1 - f_{2'}) - f_{1'} f_{2'} (1 - f) (1 - f_2)] . \end{aligned} \quad (145)$$

Above,  $d\sigma_{NN}/d\Omega$  is the differential nucleon–nucleon cross–section and  $v_{12}$  is the relative velocity. In general, the mean field  $U$  depends on both the density  $n$  and the momentum  $\vec{p}$  of the nucleon. Equation (145) contains effects due to both hard collisions and soft interactions, albeit at a semiclassical level. Theoretical studies that confronted data have thus far used isospin averaged nucleon–nucleon cross sections and mean fields of symmetric nuclear matter. It is now well established that much of the collective behavior observed in experiments stems from momentum dependent forces at play during the early stages of the collision [213]. The conclusion that has emerged from several studies is that as long as momentum dependent forces are employed in models that analyze the data, a symmetric matter compression modulus of  $\sim 220 - 240$  MeV, as suggested by the analysis of the giant monopole resonance data [190, 214], fits the heavy-ion data as well (see the recent review by Danielewicz et. al. [215]).

The prospects of rare isotope accelerators (RIA’s) that can collide highly neutron-rich nuclei has spurred further work to study a system of neutrons and protons at high neutron excess [216, 217, 218]. Generalizing Eq. (145) to a mixture, the kinetic equation for neutrons is

$$\frac{\partial f_n}{\partial t} + \vec{\nabla}_p U \cdot \vec{\nabla}_r f_n - \vec{\nabla}_r U \cdot \vec{\nabla}_p f_n = J_n = \sum_{i=n,p} J_{ni} , \quad (146)$$

where  $J_n$  describes collisions of a neutron with all other neutrons and protons. A similar equation can be written down for protons with appropriate modifications. On the left hand side of each coupled equation the mean field  $U \equiv U(n_n, n_p; \vec{p})$  depends explicitly on the neutron–proton asymmetry. The connection to the symmetry energy arises from the fact that  $U$  is obtained from a functional differentiation of the Hamiltonian density. Examples of such mean fields may be found in Refs. [133, 217, 218]. Observables that are expected to shed light on the influence of isospin asymmetry include neutron–proton differential flow and the ratio of free neutron to proton multiplicity as a function of transverse momentum at midrapidity. Experimental investigations of these signatures await the development of RIA’s at GeV energies. In this connection, it will be important to detect neutrons in addition to protons.

## 2. Multi-fragmentation

The breakup of excited nuclei into several smaller fragments during an intermediate-energy heavy-ion collision probes the phase diagram of nucleonic matter at sub-saturation density and moderate ( $\sim 10 - 20$  MeV) temperatures. In this region of the phase diagram the system is mechanically unstable if  $(dP/dn)_{T,x} < 0$ , and/or chemically unstable if  $(d\mu_p/dx)_{T,P} < 0$ . (A pedagogical account of such instabilities can be found in Ref. [219]). These instabilities, which are directly related to the symmetry energy at sub-saturation densities [220], are believed to trigger the onset of multifragmentation. Because of the instabilities, matter separates into coexisting liquid and gas phases, which each have different proton fractions, *i.e.* “isospin fractionation” [221]. This fractionation is observed in the isotopic yields which can potentially reveal information about the symmetry energy. Also, the scaling behavior of ratios of isotope yields measured in separate nuclear reactions, “isoscaling”, is sensitive to the symmetry energy [222, 223]. This scaling is expressed in the empirically observed ratio of fragment yields from two similar systems

with different neutron-to-proton ratios:

$$Y_2(N, Z)/Y_1(N, Z) \sim \exp^{\alpha N + \beta Z}, \quad (147)$$

where the constants  $\alpha$  and  $\beta$  can be related to the neutron and proton chemical potentials in a canonical ensemble description, and thus to the proton fraction of the source. To date, there are many suggestions of how the symmetry energy may affect multifragmentation [224]. Ongoing research is concerned with an extraction of reliable constraints on the symmetry energy from the presently available experimental information.

### 3. Isospin diffusion

Isospin diffusion is the process in which the symmetry energy drives the exchange of neutrons and protons between nuclei in a heavy-ion collision (see Fig. 19). This diffusion process tends to force the isospin asymmetry, i.e. the charge to baryon ratio, of the post-collision target and projectile nuclei to be equal. The isospin content of the post-collision projectile-like fragment have been recently measured in experiments [225]. Starting from a parameterization of the symmetry energy near the nuclear equilibrium density as in Eq. (44, information from multifragmentation [226] and isospin diffusion [227] observables have been combined to yield the constraint  $0.64 < i < 1.05$  and values of 31-33 MeV for  $S_{v0}$ , the symmetry energy at saturation density. This constraint is consistent with the Monte Carlo evaluation of the equation of state in Akmal et al. [228], computed from two- and three-body interactions which are matched to nucleon scattering phase shifts and the energy levels of light nuclei.

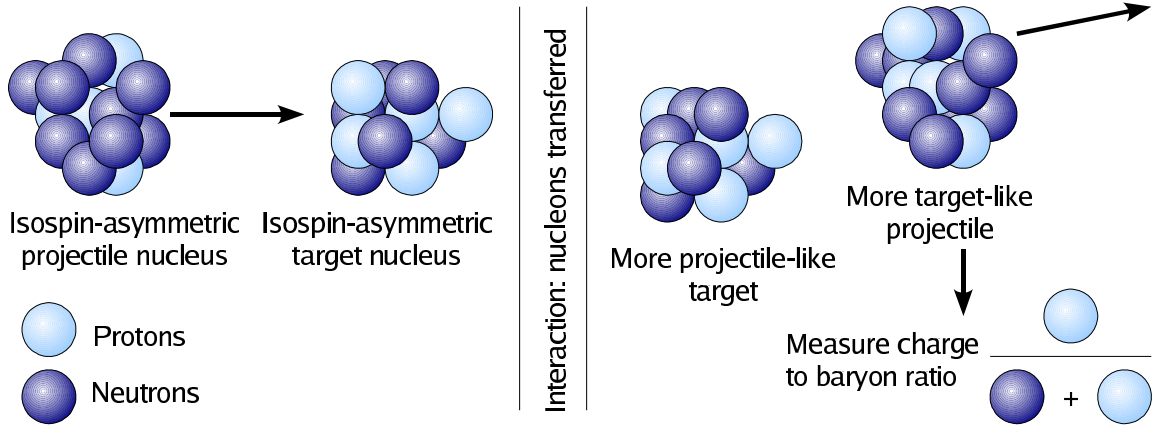


FIG. 19: Isospin diffusion process during a heavy-ion collision . (Figure courtesy of A. W. Steiner.)

In the case of isospin diffusion, the constraints obtained on the symmetry energy have also led to constraints in nuclear structure physics. This simple picture is, however, modified by fragment emission during and after the collision. This complication is alleviated [229] by considering the ratio

$$R_\delta = \frac{2\delta^{A+B} - \delta^{A+A} - \delta^{B+B}}{\delta^{A+A} - \delta^{B+B}}, \quad (148)$$

where  $A$  and  $B$  are nuclei with different isospin asymmetries and  $\delta$  is the isospin asymmetry of the projectile-like fragment. Using experimental data from the collision of  $^{112}\text{Sn}$  and  $^{124}\text{Sn}$  obtained at the

National Superconducting Cyclotron Laboratory (MSU) [225], a value  $R_\delta \sim 0.46$  was obtained. Isospin-dependent transport models [217] of the same collision suggest that only symmetry energies with  $0.64 < \gamma < 1.05$  as discussed above are compatible with the observed value of  $R_\delta$ . Because the symmetry energy is tightly correlated with the neutron skin thickness (the difference between the neutron and proton RMS radii) in lead [204], the heavy-ion collision data also offer a constraint on the neutron-skin thickness,  $R_n - R_p > 0.15$  fm [230].

Although the connection between the heavy-ion data and neutron star radii is more tenuous, owing to the fact that neutron star radii are sensitive to the symmetry energy at higher densities, isospin diffusion also offers guidance on the radii of 1.4 solar mass neutron stars. The symmetry energy from Eq. (44) suggests that the radius of a 1.4 solar mass star is likely between 11.5 and 13.6 km [231] - a range consistent with presently available astrophysical observations.

## XII. OUTLOOK

Even relative to a decade ago, the quantity of data and the variety of approaches using light waves of all wavelengths to estimate neutron star masses, radii, compactness, crustal thicknesses, etc. have mushroomed. Traditional techniques such as pulsar timing measurements have produced more than two dozen masses accurate to the 10% or better level, enough that their statistical analysis are beginning to yield information about their origin and evolution. More than a dozen thermally emitting neutron stars have had radiation radii estimated. A few stars have had redshifts determined either via direct measurements of atmospheric absorption lines or from estimates obtained from light-bending arguments. Regions in the  $M - R$  plane have been staked out from observations of accreting neutron stars including QPOs and Eddington-flux-limited sources. Other observations, including pulsar glitches, seismological studies of neutron star oscillations, and the cooling behavior following bursts or accretion, have constrained the extent of neutron star crusts. With the exception of masses, none of these other observations are yet sufficiently precise or model-independent to significantly impact dense matter theories.

In fact, some apparently contradictory conclusions have been reported over the last few years. Some neutron stars are observed to be spinning rapidly enough to exclude extremely stiff density-dependent symmetry energies. But the best-studied cooling, neutron star, the nearby source RX J1856-3754, indicates a relatively large radius. Rapidly cooling neutron star crusts following superbursts and the non-detection of neutron stars in several young supernova remnants both indicate high rates of neutrino emission in their interiors. Yet the majority of thermally-emitting neutron stars are consistent with relatively slow, or standard, core neutrino rates.

There are indications that new observations and techniques will mount even more rapidly than in the last decade, which gives hope that some of these contradictory results will be resolved. The number of known pulsars is growing rapidly, and new mass measurements implying that the neutron star maximum mass is greater than  $1.6 M_\odot$  and perhaps as large as  $2 M_\odot$  now exist. This is large enough to perhaps delimit the amounts of exotic matter (*i.e.*, hyperons, Bose condensates, or deconfined quarks) in neutron star cores. Several new pulsars have been found in highly relativistic binaries, including, in some cases, other neutron stars or pulsars. The most highly relativistic system discovered to date, PSR 0737-3039, might reveal the moment of inertia of one of its stars, yielding perhaps the most accurate measurement of a neutron star radius possible. Furthermore, its relative closeness and dimness strongly suggests that several even more relativistic binaries will soon be found.

At the opposite extreme, there are indications that neutron stars smaller than  $1.2 M_\odot$  exist. This value is uncomfortably close to the empirical minimum found in supernova models stemming from the evolved cores of the smallest stars thought to be capable of the event, approximately  $8 M_\odot$  initial mass. Theoretically, proto-neutron stars as small as  $0.9 M_\odot$  could be stable, and it will be interesting to see if

masses approaching this value are observed.

Less traditional methods, involving neutrinos and gravity waves, that could be utilized to infer information about neutron stars should soon become available. The 20 neutrinos detected from SN 1987A twenty years ago will be dwarfed by the thousands or even tens of thousands that could be observed today from a galactic supernova. Statistical uncertainties in the total binding energy, the deleptonization and cooling timescales, the average neutrino energies, etc. should be quite small, permitting important conclusion to be drawn about the proto-neutron star's mass and opacities. In addition, tens or more  $\nu_e$ 's could be detected during the collapse prior to bounce, their number and average energy crucially depending on the density dependence of the symmetry energy below nuclear density. The observation of gravity waves from compact star binary mergers is eagerly anticipated, even more so now that the pulsar binary PSR 0737-3039 has been discovered. In fact, the gravity waves observed from a binary merger might be the least unambiguous way to learn of the existence of quark matter stars.

Complementing the increase in observational data has been the development of new techniques, supporting theory and laboratory data relevant to dense matter physics. It is now known that the underlying physics behind the neutron star maximum mass and typical neutron star radii are quite different. The maximum mass is set by the dense matter equation of state well beyond  $2n_s$ , but neutron star radii are determined by  $dE_{sym}/dn$  in the range  $1 - 2n_s$ . It is similarly expected that better models of emission beams from accreting neutron stars, pulsar glitches, superfluidity and superconductivity involving nucleons and hyperons, neutron star atmospheres, and the seismology of crustal oscillations will make better use of accumulating data.

Laboratory experiments relevant to nuclear astrophysics in general, and to neutron stars in particular, have accelerated significantly in recent years. With impressive efficiency, masses of most nuclei between the path of beta stability and the neutron drip line have now been measured. With the Rare Isotope Accelerator and Jefferson Lab experiments, many more mass measurements of extremely neutron-rich nuclei and flow measurements of neutron-rich heavy ion collisions will be forthcoming. More knowledge of hyperon-nucleon interactions through studies of hypernuclei should be available. Perhaps one of the more intriguing experiments is the PREX experiment at the Jefferson Laboratory to measure the neutron radius of  $Pb^{208}$  to 1% accuracy, which should yield a neutron skin thickness estimate sufficiently precise to offer significant constraints on the neutron star radius. Such experiments should be extended to other neutron-rich nuclei. Multifragmentation and isospin diffusion studies from heavy ion collisions should yield more accurate information concerning the symmetry energy of nucleonic matter and the critical density for phase separation in dense matter, which is particularly relevant to the determination of the core-crust interface density, pressure and enthalpy. New studies of giant monopole, dipole and other nuclear vibrational modes should be undertaken to study the nuclear incompressibility and symmetry energy properties. In addition, new neutrino laboratories are planned, including UNO, that will refine measurements of neutrino oscillations which could be relevant for interpreting neutrino signals from supernovae. These new neutrino laboratories will also improve by an order of magnitude or more, the number of neutrinos observed from a supernova, and will increase the rate at which supernovae are observed as well. New experiments involving neutrino interactions with heavy nuclei could shed light on neutrino absorption and scattering rates, quantifying the effects of density, spin and isospin correlations for opacities of dense matter.

Although we've not commented on recent developments in microscopic theory, a topic to which Hans Bethe devoted much of his early career, there have been many of interest for neutron stars. Much effort has gone into determining the EOS of neutron matter at subnuclear densities which is consistent with phase shift data. The effects of Pauli blocking and density, spin and isospin correlations on neutrino opacities have been explored. New explorations of the pairing gaps of nucleons and hyperons, the hyperon-nucleon interaction and the threshold densities of hyperons have appeared. Finally, new studies are targeting the properties of pion and kaon condensates and delineating quark matter properties including color

compositions, gaps and critical densities.

### Acknowledgements

This work was supported in part by the U.S. Department of Energy under grant DOE/DE-FG02-87ER-40317 (for JML) and DOE/DE-FG02-93ER40756 (for MP).

- 
- [1] E. Witten, Phys. Rev. **D30**, 272 (1984); E. Fahri & R. L. Jaffe, Phys. Rev. **D30**, 2379 (1984)
  - [2] M. G. Alford, K. Rajagopal, S. Reddy, & A. W. Steiner, Phys. Rev. **D73**, 4016 (2006)
  - [3] A. Burrows & J. M. Lattimer, ApJ **307**, 178 (1986)
  - [4] M. Prakash et al., *Physics of Neutron Star Interiors*, eds. D. Blaaschke, N. K. Glendenning and A. Sedrakian, Springer-Verlag, New York, Lect. Notes. Phys. **578**, 364 (2001)
  - [5] C. E. Rhoades Jr. & R. Ruffini, Phys. Rev. Lett. **32**, 324 (1974)
  - [6] J. M. Lattimer & M. Prakash, ApJ, **550**, 426 (2001)
  - [7] V. Kalogera et al., ApJL **614**, L137 (2004)
  - [8] J. M. Lattimer & D. G. Ravenhall, ApJL **223**, L314 (1978)
  - [9] H. A. Bethe, G. E. Brown, J. Applegate & J. M. Lattimer, Nucl. Phys **A324**, 487 (1979)
  - [10] D. Q. Lamb, J. M. Lattimer, C. J. Pethick & D. G. Ravenhall, Phys. Rev. Lett. **41**, 1623 (1978)
  - [11] M. Prakash, T. L. Ainsworth, J. P. Blaizot and H. Wolter, in *Windsurfing the Fermi Sea*, Proceedings of the International Conference and Symposium on “Unified Concepts of Many-Body Problems”, Stony Brook, eds. T. T. S. Kuo and J. Speth, 357 (1986)
  - [12] J. B. Hartle & A. G. Sabbadini, ApJ **213**, 831 (1977)
  - [13] L. Lindblom, ApJ **278**, 364 (1984)
  - [14] N. K. Glendenning, Phys. Rev. **D46**, 4161 (1992)
  - [15] S. Koranda, N. Stergioulas & J. L. Friedman, ApJ **488**, 799 (1997); N. K. Glendenning, Phys. Rev. **D46**, 4161 (1992)
  - [16] V. R. Pandharipande & D. G. Ravenhall, in *Proc. NATO Advanced Research Workshop on Nuclear Matter and Heavy Ion Collisions*, ed. M. Soyeur et al., Plenum, New York, 103 (1989)
  - [17] J. M. Lattimer & M. Prakash, Phys. Rev. Lett. **94**, 1101 (2005)
  - [18] R. C. Tolman, Phys. Rev. **55**, 364 (1939)
  - [19] P. Haensel & J.L. Zdunik, Nature **340**, 617 (1989)
  - [20] J. L. Friedman, L. Parker & J. R. Ipser, ApJ **304**, 115 (1986); J. M. Lattimer, M. Prakash, D. Masak & A. Yahil, ApJL **355**, L241 (1990)
  - [21] J. M. Lattimer & M. Prakash, Science **304**, 536 (2004)
  - [22] J. W. T. Hessels et al., Science **311**, 1901 (2006)
  - [23] P. Kaaret et al., astro-ph/0611716 (2006)
  - [24] J. S. Clark et al., A&A **392**, 909 (2002) (a)
  - [25] O. Barziv et al., A&A **377**, 925 (2001) (b)
  - [26] H. Quaintrell et al., A&A **401**, 303 (2003) (c)
  - [27] J. A. Orosz & E. Kuulkers, MNRAS **305**, 132 (1999) (d)
  - [28] S. E. Thorsett & D. Chakrabarty, ApJ **512**, 288 (1999) (e)
  - [29] D. J. Nice, E. M. Splaver, & I. H. Stairs, IAU Symposium 218, eds. F. Camilo and B.-M. Gaensler, 49 (2004); astro-ph/0311296; also private communication (f)

- [30] D. J. Nice, E. M. Splaver & I. H. Stairs, ASP Conf. Ser. **302**, *Radio Pulsars*, eds. M. Bailes, D. J. Nice and S. E. Thorsett, Ast. Soc. Pac., San Francisco, 75 (2003); astro-ph/0210637 (g)
- [31] D. J. Nice, E. M. Splaver & I. H. Stairs, ApJ **549**, 516 (2001) (h)
- [32] A. G. Lyne et al., Science **303**, 1153 (2004) (i)
- [33] M. Bailes et al., ApJL **595**, L49 (2003) (j)
- [34] M. H. van Kerkwijk, J. van Paradijs & E. J. Zuiderwijk, A&A **303**, 497 (1995) (k)
- [35] D. M. Gelino, J. A. Tomsick & W. A. Heindl, BAAS **34**, 1199 (2003); J.A. Tomsick, private communication (l)
- [36] Ch. Lange et al., MNRAS **326**, 274 (2001) (m)
- [37] T. Muñoz-Darias, J. Casares & I. G. Martínez-Pais, ApJ **635**, 502 (2005) (n)
- [38] P. G. Jonker, D. Steeghs, G. Nelemans & M. van der Klis, MNRAS **356**, 621 (2005) (o)
- [39] W. van Straten et al., Nature **412**, 158 (2001) (p)
- [40] J. M. Weisberg & J. H. Taylor, ASP Conf. Ser. **328**, *Binary Radio Pulsars*, eds. F. A. Rasio and I. H. Stairs, Ast. Soc. Pac., San Francisco, 25 (2005); astro-ph/0407149 (q)
- [41] E. M. Splaver et al., ApJ **620**, 405 (2005) (r)
- [42] A. J. Faulkner et al., ApJL **618**, L119 (2004) (s)
- [43] S. M. Ransom et al., Science **307**, 892 (2005) (t)
- [44] B. A. Jacoby et al., ApJ **629**, 113 (2005) (u)
- [45] D. J. Nice, et al. ApJ **634**, 1242 (2005) (v)
- [46] P. C. Freire et al., MNRAS **340**, 1359 (2003) (w)
- [47] B. A. Jacoby, PhD dissertation, CalTech (x)
- [48] E. M. Splaver et al., ApJ **581**, 509 (2002) (y)
- [49] D. J. Champion et al., MNRAS **363**, 929 (2005) (z)
- [50] A. Corongiu et al., Mem. S. A. It Suppl. **5**, 188 (2004) (A)
- [51] D. R. Lorimer et al., ApJ **640**, 428 (2006) (B)
- [52] D. J. Nice, J. H. Taylor & R. W. Sayer, *Pulsar Timing, General Relativity, and the Internal Structure of Neutron Stars*, eds. E. Van den Heuvel, J. Van Paradijs and Z. Arzoumanian, Elsevier (1999); <http://pulsar.princeton.edu/ftp/pub/papers/ams-96.ps> (C)
- [53] H. A. Bethe & G. E. Brown, ApJ **506**, 780 (1998)
- [54] N. K. Glendenning, ApJ, **293**, 470 (1985);  
*Compact Stars, Nuclear Physics, Particle Physics and Cosmology*, Springer, New York (1997)
- [55] J. Ellis, J. I. Kapusta & K. A. Olive, Nucl. Phys. **B348**, 345 (1991)
- [56] R. Knorren. M. Prakash & P. J. Ellis, Phys. Rev. **C52**, 3470 (1995)
- [57] J. Schaffner & I. N. Mishustin, Phys. Rev. **C53**, 1416 (1996)
- [58] D. B. Kaplan & A. E. Nelson, Phys. Lett. **B175**, 57 (1986); **B179**, 409 (1986)
- [59] D. Page, ApJ **442**, 273 (1995)
- [60] D. Scott, D. Leahy & R. Wilson, ApJ **539**, 392 (2000)
- [61] D. Leahy, ApJ **613**, 517 (2004)
- [62] G. E. Brown, K. Kubodera, M. Rho & V. Thorsson, Phys. Lett. **B291**, 355 (1992)
- [63] H. D. Politzer & M. B. Wise, Phys. Lett. **B273**, 156 (1991)
- [64] T. Muto & T. Tatsumi, Phys. Lett. **B283**, 165 (1992); T. Muto, Prog. Theor. Phys. **89**, 415 (1993); T. Muto et al, Prog. Theor. Phys. Suppl. **112**, 221 (1993); H. Fujii et al., Nucl. Phys, **A571**, 758 (1994)
- [65] T. Maruyama, H. Fujii, T. Muto & T. Tatsumi, Phys. Lett. **B337**, 19 (1994)
- [66] G. E. Brown, C-H. Lee, M. Rho & V. Thorsson, Nucl. Phys. **A567**, 937 (1994)
- [67] G. E. Brown, C-H. Lee, H-J, Park & M. Rho, Phys. Rev. Lett., **96**, 062303 (2006)
- [68] V. Thorsson, M. Prakash & J. M. Lattimer, Nucl. Phys. **A572**, 693 (1994)

- [69] M. Alford, M. Braby, M. Paris & S. Reddy, *ApJ* **629**, 969 (2005)
- [70] D. Gonddek, P. Haensel & J. L. Zdunik, Pacific Rim Conference on Stellar Astrophysics, ed. K. L. Chan, K.S. Cheng and H.P. Singh, ASP Conf. Ser. **138**, 131 (1998)
- [71] H.-A. Buchdahl, *ApJ* **147**, 310 (1967)
- [72] J. P. Blaizot, *Phys. Rep.* **65**, 171 (1980)
- [73] J. M. Pearson, *Phys. Lett.* **B271**, 12 (1991)
- [74] H. Krivine, *J. de Phys. Supp.* **C6**, 153 (1984)
- [75] J. Lattimer, *Nuclear Equation of State*, eds. A. Ansari and L. Satpathy, World Scientific, Singapore, 83 (1996)
- [76] B. Link, R. I. Epstein & J. M. Lattimer, *Phys. Rev. Lett.* **83**, 3362(1999)
- [77] R. C. Duncan, *ApJL* **498**, L45 (1998)
- [78] R. E. Rutledge et al., *ApJ* **580**, 413 (2006)
- [79] J. B. Hartle, *ApJ* **150**, 1005 (1967)
- [80] J. M. Lattimer & B. F. Schutz, *ApJ* **629**, 979 (2005)
- [81] S. Kubis, astro-ph/0611740 (2006)
- [82] D. Q. Lamb, J. M. Lattimer, C. J. Pethick & D. G. Ravenhall, *Nucl. Phys.* **A411**, 449 (1983)
- [83] H. B. Callen, *Thermodynamics*, John Wiley & Sons, New York (1985)
- [84] P. W. Anderson & N. Itoh, *Nature* **256**, 25 (1975); M. Ruderman, *ApJ* **203**, 213 (1976); D. Pines & M. A. Alpar, *Nature* **316**, 27 (1985)
- [85] B. Link, *A&A* **458**, 881 (2006)
- [86] C. Barat et al., *A&A* **126**, 400 (1983)
- [87] G. L. Israel et al., *ApJL* **628**, L53 (2005)
- [88] T. E. Strohmayer & A. L. Watts, *ApJL* **632**, L111 (2005)
- [89] L. Samuelsson & N. Andersson, submitted to MNRAS, astro-ph-0609265 (2006)
- [90] J. M. Lattimer, K. A. van Riper, M. Prakash & Manju Prakash, *ApJ* **425**, 802 (1994)
- [91] K. A. van Riper, *ApJ* **329**, 339 (1988)
- [92] O. Y. Gnedin, D. G. Yakovlev & A. Y. Potekhin, *MNRAS* **324**, 725 (2001)
- [93] A. D. Kaminker et al., *MNRAS* **371**, 477 (2006)
- [94] P. G. Jonker, P.G. et al., *MNRAS* **368**, 1803 (2006)
- [95] E. Kuulkers et al., *A&A* **382**, 503 (2002)
- [96] R. Wijnands et al., *ApJL* **560**, L159 (2002)
- [97] F. M. Walter & J. M. Lattimer, *ApJ* **576**, 145 (2002)
- [98] F. M. Walter & J. K. Faherty, in *Isolated Neutron Stars*, ed. D. Page, R. Turolla & S. Zane, ApSS, Springer (2006)
- [99] B. Gendre, B. Barret & N. A. Webb, *A&A* **403**, L11 (2003)
- [100] B. Gendre, B. Barret & N. A. Webb, *A&A* **400**, 521 (2003)
- [101] C. O. Heinke, G. B. , Rybicki, R. Narayan & J. E. Grindlay, *ApJ* **644**, 1090 (2006)
- [102] J. M. Lattimer, C. J. Pethick, M. Prakash & P. Haensel, *Phys. Rev. Lett.* **66**, 2701 (1991)
- [103] M. Prakash, M. Prakash, J. M. Lattimer, & C. J. Pethick, *ApJL* **390**, L77 (1992)
- [104] D. Page, J. M. Lattimer, M. Prakash, & A. W. Steiner, *ApJS* **155**, 623 (2004)
- [105] P. Slane, D. J. Helfand, E. Van der Swaluw & S. S. Murray, *ApJ* **616**, 403 (2004)
- [106] D. L. Kaplan et al., *ApJS* **153**, 269 (2004)
- [107] J. Cottam, F. Paerls & M. Mendez, *Nature* **420**, 51 (2002)
- [108] A. R. Villarreal & T. E. Strohmayer, *ApJL* **614**, L121 (2004)
- [109] L. Sidoli, A. N. Parmar & T. Oosterbroek, *A&A* **429**, 291 (2005)
- [110] S. Bhattacharyya, M. C. Miller & F. K. Lamb, *ApJ* **644**, 1085 (2006)

- [111] J. Madej, P. C. Joss & A. Rozanska, *ApJ* **602**, 904 (2004)
- [112] F. Ozel, *Nature* **441**, 1115 (2006)
- [113] J. A. Van Paradijs, *A&A* **101**, 174 (1981)
- [114] N. A. Inogamov & R. A. Sunyaev, *Astron. Lett.* **25**, 269 (1999)
- [115] V. Suleimanov & J. Poutanen, *MNRAS* **369m** 2036 (2006)
- [116] M. van der Klis, in *Compact Stellar X-ray Sources*, eds. W.H.G. Lewin & M. van der Klis (Cambridge: Cambridge Univ. Press), in press (2006); astro-ph/0410551
- [117] M. C. Miller, F. K. Lamb & D. Psaltis, *ApJ* **508**, 791 (1998)
- [118] L. Stella & M. Vietri, *ApJL* **492**, L59 (1998); M. A. Abramowicz et al., *PASJ* **55**, 567 (2003)
- [119] D. Barret, J.-F. Olive & M. C. Miller, *MNRAS* **370**, 1140 (2006)
- [120] J. Casares, *MNRAS*, in press (2006); astro-ph/0610086
- [121] M. Burgay et al., *Nature* **426**, 531 (2003)
- [122] T. Damour & G. Schaefer, *Nuovo Cimento* **B101**, 127 (1988)
- [123] M. Bejger & P. Haensel, *A&A* **405**, 747 (2003)
- [124] R. A. Fesen, J. M. Shull & A. P. Hurford, *ApJ* **113**, 354 (1997)
- [125] B. M. Barker & R. F. O'Connell, *Phys. Rev.* **D12**, 329 (1975)
- [126] W. Keil & H-T Janka, *A&A* **29**, 145 (1995)
- [127] A. Burrows & R. F. Sawyer, *Phys. Rev.* **C59**, 510 (1999)
- [128] J. A. Pons, S. Reddy, M. Prakash & J. M. Lattimer, J. A. Miralles, *ApJ* **513**, 780 (1999)
- [129] J. A. Pons, J. A. Miralles, M. Prakash & J. M. Lattimer, *ApJ* **553** (2001) 382.
- [130] J. A. Pons, A. W. Steiner, M. Prakash & J. M. Lattimer, *Phys. Rev. Lett.* **86**, 5223 (2001)
- [131] C. K. Jung, *Next Generation Nucleon Decay and Neutrino Dectector*, ed. N. Diwan and C.K. Jung, AIP, New York, 29 (2000)
- [132] A. Burrows, *Ann. Rev. Nucl. Sci.* **40**, 181 (1990)
- [133] M. Prakash et al., *Phys. Rep.* **280**, 1 (1997)
- [134] P. J. Ellis, J. M. Lattimer & M. Prakash, *Comm. Nucl. Part. Phys.* **22**, 63 (1996); M. Prakash, J. R. Cooke & J. M. Lattimer, *Phys. Rev. D* **52**, 661 (1995); A. W. Steiner, M. Prakash & J. M. Lattimer, *Phys. Lett.* **B486**, 239 (2000)
- [135] A. Burrows, *ApJ* **334**, 891 (1988)
- [136] S. Reddy, PhD thesis, Stony Brook University (1998)
- [137] A. Burrows & B. Fryxell, *ApJL* **418**, L33 (1993); M. Herant et al., *ApJ* **435**, 339 (1994); W. Keil, H.-T. Janka & E. Müller, *ApJL* **473**, L111 (1995); A. Mezzacappa et al., *ApJ* **495**, 911 (1998); J. A. Miralles, J. A. Pons & V. A. Urpin, *ApJ* **543**, 1001 (2000)
- [138] A. Burrows & R. F. Sawyer, *Phys. Rev. C* **58**, 554 (1998); S. Reddy, M. Prakash, J. M. Lattimer & J. A. Pons, *Phys. Rev. C* **59**, 2888 (1999)
- [139] G. E. Brown & H. A. Bethe, *ApJ* **423**, 659 (1994)
- [140] M. Prakash, J. R. Cooke & J. M. Lattimer, *Phys. Rev.* **D52**, 661 (1995)
- [141] F. K. Thielemann, M. Hashimoto & K. Nomoto, *ApJ* **349**, 222 (1990); H. A. Bethe & G. E. Brown, *ApJL* **445**, L129 (1995)
- [142] G. W. Carter & S. Reddy, *Phys. Rev.* **D62**, 103002 (2000)
- [143] B. Paczynski, *Acta Astron.* **42**, 145 (1992)
- [144] C. Thompson & R. C. Duncan, *MNRAS* **275**, 255 (1995)
- [145] C. Thompson & R. C. Duncan, *ApJ* **473**, 322 (1996)
- [146] A. Melatos, *ApJL* **519**, L77 (1999)
- [147] C. Y. Cardall, M. Prakash & J. M. Lattimer, *ApJ* **554**, 322 (2001)
- [148] C. Kouveliotou et al., *Nature* **393**, 235 (1998)

- [149] R. C. Duncan & C. Thompson, *ApJL* **392**, L9 (1992)
- [150] R. C. Duncan & C. Thompson, *ApJ* **469**, 764 (1996)
- [151] D. Lai & S. L. Shapiro, *ApJ* **383**, 745 (1991)
- [152] V. Canuto & J. Ventura, *Fund. Cosmic Phys.* **2**, 203 (1977)
- [153] I. Fushiki, E. H. Gudmundsson & C. J. Pethick, *ApJ* **342**, 958 (1989); I. Fushiki, E. H. Gudmundsson, C. J. Pethick & J. Yngvason, *Ann. Phys.* **216**, 29 (1992); A. M. Abrahams & S. L. Shapiro, *ApJ* **374**, 652 (1991)
- [154] Ö. E. Rögnvaldsson, I. Fushiki, E. H. Gudmundsson, C. J. Pethick & J. Yngvason, *J.*, *ApJ* **416**, 276 (1993); A. Thorlofsson, Ö. E. Rögnvaldsson, J. Yngvason & E. H. Gudmundsson, *ApJ* **502**, 847 (1998)
- [155] S. Chakrabarty, *Phys. Rev.* **D54**, 1306 (1996)
- [156] S. Chakrabarty, D. Bandyopadhyay & S. Pal, *Phys. Rev. Lett.* **78**, 2898 (1997)
- [157] Y. F. Yuan & J. L. Zhang, *ApJ* **525**, 920 (1999)
- [158] M. Boucquet, S. Bonazzola, F. Gourgoulhon & J. Novak, *A&A* **301**, 757 (1995)
- [159] A. Broderick, M. Prakash & J. M. Lattimer, *ApJ* **537**, 351 (2000)
- [160] A. Broderick, M. Prakash & J. M. Lattimer, *Phys. Lett* **B531**, 167 (2002)
- [161] L. D. Landau, L.M. Lifshitz & L. P. Pitaevskii, *Electrodynamics of Continuous Media, 2nd ed.*, Pergamon, New York (1984)
- [162] R. D. Blandford & L. Hernquist, *J. Phys. C: Solid State Phys.* **15**, 6233 (1982)
- [163] J. Schwinger, *Particles, Sources and Fields*, Vol. 3, Addison-Wesley, Redwood City, 164 (1988)
- [164] M. Ruderman, *Millisecond Pulsars: A Decade of Surprise*, eds. A. S. Fruchter, M. Tavani, and D. C. Backer, ASP Conf. Ser. **72**, Ast. Soc. Pac., San Francisco, 277 (1995)
- [165] K. S. Thorne, *Three Hundred Years of Gravitation*, ed. S. W. Hawking and W. Israel, Cambridge Univ. Press, Cambridge, Ch. 9 (1973).
- [166] J. M. Lattimer & D. N. Schramm, *ApJ* **210**, 549 (1976)
- [167] D. Eichler, M. Livio, T. Piran & D. N. Schramm, *Nature* **340**, 126 (1989)
- [168] J. A. Faber, P. Grandclement & F. A. Rasio, *Phys. Rev.* **D69**, 14036 (2004)
- [169] J. P. A. Clark, *Astrophys. Lett.* **18**, 73 (1977)
- [170] P. Jaranowski & A. Krolak, *ApJ* **394**, 586 (1992)
- [171] S. F. Portegies Zwart, *ApJ* **503**, 53 (1998)
- [172] J. M. Lattimer, F. Mackie, D. G. Ravenhall & D. N. Schramm, *ApJ* **213**, 225 (1977)
- [173] B. S. Meyer, *ApJ* **343**, 254 (1989)
- [174] M. Colpi, S. L. Shapiro & S. A. Teukolsky, *ApJ* **414**, 717 (1993)
- [175] S. Ratkovic, M. Prakash & J. M. Lattimer, submitted to *ApJ*, astro-ph/0512133 (2005)
- [176] P. C. Peters, *Phys. Rev.* **B136**, 1224 (1964)
- [177] Z. Kopal, *Close Binary Systems*, Wiley, New York (1959)
- [178] P. P. Eggleton, *ApJ* **268**, 368 (1983)
- [179] C. Alcock & A. Olinto, *Ann. Rev. Nucl. Part. Sci.*, **38**, 161 (1988)
- [180] M. Prakash, E. Baron & Manju Prakash, *Phys. Lett. B.* **243**, 175 (1990)
- [181] J. Madsen, *J. Phys. G.* **28**, 1737 (2002)
- [182] C. Cutler & E. E. Flanagan, *Phys. Rev.* **D49**, 2658 (1994)
- [183] J. A. Faber, P. Grandclement, F. A. Rasio & K. Taniguchi, *Phys. Rev. Lett.* **89**, 231102 (2002)
- [184] H. A. Bethe & R. F. Bacher, *Rev. Mod. Phys.* **8**, 82 (1936); C. F. von Weizsäcker, *Z. Physik* **96**, 431 (1935)
- [185] W. D. Myers & W. J. Swiatecki, *Ann. Phys.* **55**, 395 (1969)
- [186] J. M. Lattimer, C. J. Pethick, D. G. Ravenhall & D. Q. Lamb, *Nucl. Phys.* **A 432**, 646 (1985).
- [187] A. W. Steiner, M. Prakash, J. M. Lattimer & P. J. Ellis, *Phys. Rep.* **411**, 325 (2005)
- [188] P. Danielewicz, *Nucl. Phys.* **A 727**, 233 (2003)
- [189] M. Hausmann et al., *Hyperfine Interactions*, **132**, 289 (2001); D. Lunney, J. M. Pearson & C. Thibault,

- Rev. Mod. Phys. **75**, 1021 (2003); U Hager et al., Phys. Rev. Lett. **96**, 042304 (2006)
- [190] S. Shlomo, V.M. Kolomietz & G. Colo, Eur. Phys. J. **A30**, 23 (2006); T. Sil, S. Shlomo, B. K. Agarwal & P.-G. Reinhard, Phys. Rev. C **73**, 034316 (2006); B. K. Agarwal, S. Shlomo & V. Kim Au, Phys. Rev. C **72**, 014310 (2005); B. K. Agarwal, S. Shlomo & V. Kim Au, Phys. Rev. C **68**, 031304 (2003)
- [191] E. Lipparani & S. Stringari, Phys. Rep. **103**, L175 (1989)
- [192] R. Bergere, in *Lecture Notes in Physics* **61**, eds. S. Costa and C. Scharf, Springer, Berlin, 1 (1977)
- [193] R. M. Laszewski & P. Axel, Phys. C **19**, 342 (1979)
- [194] O. Bohigas, N. Van Giai & D. Vautherin, Phys. Lett. **B 102**, 105 (1981)
- [195] E. Lipparini & S. Stringari, Phys. Lett. **B 112**, 421 (1982)
- [196] H. Krivine, C. Schmit & J. Treiner, Phys. Lett **B 112**, 281 (1982)
- [197] E. Lipparini & S. Stringari, Nucl. Phys. A **482**, 205c (1988)
- [198] S. Khamerdzhiev, J. Speth & G. Tertychny, Nucl. Phys. **A 624**, 328 (1997)
- [199] B. C. Clark, L. J. Kerr & S. Hama, Phys. Rev. C **67**, 054605 (2003)
- [200] A. Trzcinska et al., Phys. Rev. Lett. **87**, 082501 (2001)
- [201] S. Karataglidis, K. Amos & B. A. Brown, Phys. Rev. C **65**, 044306 (2002)
- [202] C. J. Horowitz, S. J. Pollock, P. A. Souder & R. Michaels, R., Phys. Rev. **C63**, 025501 (2001)
- [203] R. Michaels, P. A. Souder & G. M. Urciuoli, Jefferson Laboratory Proposal **PR-00-003** (2000).
- [204] B. A. Brown, Phys. Rev. Lett. **85**, 5296 (2000)
- [205] S. Typel & B. A. Brown, Phys. Rev. C **64**, 027302 (2001)
- [206] C. J. Horowitz & J. Piekarewicz, Phys. Rev. Lett. **86**, 5647 (2001)
- [207] H. H. Gutbrod, A. M. Poskanzer & H. G. Ritter, Rep. Prog. Phys. **52**, 267 (1989)
- [208] P. Danielewicz & G. Odyniec, Phys. Lett. **157**, 146 (1985)
- [209] H. A. Gustafsson et al., Phys. Rev. Lett. **52**, 1590 (1984)
- [210] G. M. Welke, M. Prakash, T. T. S. Kuo & S. Das Gupta, Phys. Rev. C **38**, 2101 (1988)
- [211] P. Siemens & J. O. Rasmussen, Phys. Rev. Lett. **42**, 880 (1979)
- [212] G. F. Bertsch & S. Das Gupta, Phy. Rep. **160**, 189 (1988)
- [213] C. Gale et al., Phys. Rev. C **41**, 1545 (1990)
- [214] D. H. Youngblood, H. L. Clark & Y.-W. Lui, Phys. Rev. Lett. **82**, 691 (1999)
- [215] P. Danielewicz, R. Lacey & W. G. Lynch, Science **298**, 1592 (2002)
- [216] C. B. Das, S. Das Gupta & C. Gale, Phys. Rev. C **67**, 034611 (2003)
- [217] B.-A. Li, C. B. Das Gupta & C. Gale, Phys. Rev. C **88**, 192701 (2004)
- [218] B.-A. Li, C. B. Das & S. Das Gupta, Nucl. Phys. **A 735**, 563 (2004)
- [219] P. Chomaz, M. Colonna & J. Randrup, Phys. Rep. **389**, 263 (2004)
- [220] B. A. Li & C. M. Ko, Nucl. Phys. **A 618**, 498 (1997)
- [221] H. S. Xu et al., Phys. Rev. Lett. **85**, 716. (2000)
- [222] M. B. Tsang et al., Phys. Rev. Lett. **86**, 5023 (2001)
- [223] A. Ono et al., Phys. Rev. C **68**, 051601 (2003)
- [224] C. B. Das et al., Phys. Rep. **406**, 1 (2005)
- [225] M. B. Tsang et al., Phys. Rev. Lett. **92**, 062701 (2004)
- [226] D. V. Shetty et. al., Phys. Rev. **C70**, 011601 (2004)
- [227] L. W. Chen, C. M. Ko & B.-A. Li, Phys. Rev. Lett. **94**, 032701 (2005)
- [228] A. Akmal, V. R. Pandharipane & D. G. Ravenhall, Phys. Rev. **C58**, 1804. (1998)
- [229] F. Rami et al., Phys. Rev. Lett. **84**, 1120 (2000)
- [230] A. W. Steiner & B.-A. Li, Phys. Rev. C **72**, 041601 (2005)
- [231] B.-A. Li & A. W. Steiner, Phys. Lett. **B642**, 436 (2006)